UNIVERSITÀ
DEGLI STUDI
FIRENZE

DOTTORATO DI RICERCA IN ENERGETICA E
TECNOLOGIE INDUSTRIALI E AMBIENTALI INNOVATIVE

CICLO XXXVI
COORDINATOR Prof. Giovanni Ferrara

High-fidelity CFD methods for the aero-acoustic design of modern turbofan engines

Settore scientifico disciplinare ING-IND/08

Dottorando
Dott. Simone Giaccherini
Department of Industrial Engineering, University of Florence

Supervisore
Prof. Andrea Arnone
Department of Industrial Engineering, University of Florence

Coordinatore
Prof. Giovanni Ferrara
Department of Industrial Engineering, University of Florence

Firenze, 01/11/2020 - 31/10/2023

"Non e' la destinazione, ma il viaggio che conta" -
Capitan Jack Sparrow

A mia nonna, che ha sempre creduto in me fin dall'inizio di questo percorso universitario durato 10 anni. E che oggi sarebbe stata sicuramente la più orgogliosa per il conseguimento di questo mio titolo

Acknowldegements

Desidero anzitutto ringraziare i Proff. Andrea Arnone, Michele Marconcini e Roberto Pacciani per la fiducia in me riposta e per avermi dato l'opportunità di approfondire le tematiche di questa tesi di dottorato.

Ringrazio inoltre il collega e potrei dire "mentore" Lorenzo Pinelli, con cui ho instaurato un solido legame di amicizia e da cui ho imparato moltissimo sia sotto il punto di vista professionale che umano.

Ringrazio quindi tutti i colleghi del gruppo di ricerca T-Group, con cui ho trascorso momenti indimenticabili durante questi tre anni di dottorato all'università.

Ultimi, ma non meno importanti, ringrazio i miei familiari e la mia futura moglie Carmela che mi hanno sempre spronato a dare il meglio di me stesso in ogni occasione.

Abstract

The exponential growth of civil air traffic during the last decades has forced the aeronautical community to face noise pollution of air routes striking urban areas. At the same time, the massive improvements in high parallel computing of the recent years have oriented the aeronautical industry towards the use of high-fidelity computational fluid dynamics (CFD) methods for the aero-acoustic design of the modern turbofan engines. The need for scale-resolved simulations comes from the highly unsteady flow structures from which noise emissions are generated and then propagated from inside the engine to the open field. These aspects cannot be investigated with traditional turbulence model based on Unsteady Reynolds Average Navier Stokes (URANS) approaches which are not able to capture most of the aerodynamic sources responsible for aircraft noise.

In this framework, the aim of this Ph.D. thesis is to demonstrate the capabilities of the high-fidelity techniques for the investigation of the acoustic performance of two common aeronautical devices for noise abatement: the acoustic liners and the chevron exhaust nozzles. The numerical analyses of this work have been performed using the open-source OpenFOAM suite.

Concerning acoustic liners, a single-degree-of-freedom (SDOF) open geometry experimentally studied at the NASA Langley Center has been selected for the validation of the proposed Large Eddy Simulation (LES) method for acoustic impedance eduction. Several simulations have been carried out to investigate the absorption characteristics of perforated panels under the effects of grazing flow and acoustic excitation. Then, a semi-analytical model for innovative multi-degree-of-freedom (MDOF) liners has been developed and validated through the same LES environment.

Moving to the jet noise investigation, the hybrid Delayed Detached Eddy Simulation (DDES) approach coupled with a Computational Aero-Acoustic (CAA) method based on the Ffowcs-William-Hawkings (FWH) analogy has been used to study round and chevron exhaust nozzle geometries fully described in the literature. The core of this activity has been the feasibility of performing such studies by means of an open-source CFD code, also highlighting the physical mechanisms responsible for the abatement of broadband jet noise. To this end, general guidelines on the set-up of scale-resolved simulations have been provided, with a particular focus on the meshing technique for accurate noise predictions. Moreover, aerodynamic aspects of the jet features from the round and the chevron nozzles are debated, and comparisons between the broadband noise spectra are presented. This aero-acoustic investigation has been oriented to a proper design of the tooth-saw shape of the engine exhaust aiming at efficiently tackling jet noise emissions.

Contents

List of Figures

List of Tables

1

Introduction

This introduction is intended to provide a brief overview on the topic faced in this work of thesis. Firstly, the issues of noise pollution from civil aviation are discussed, underlining the need for a low-noise design of new aircrafts. Then, some aspects of the high-fidelity Computational Fluid Dynamics (CFD) are presented, clarifying why this numerical method should be preferred for aeronautical applications.

1.1 Aircraft noise

Nowadays, the recover of civil air traffic to pre-pandemic standards has brought with it a sharp growth of noise pollution from aviation. According to the EUROCONTROL agency [1], before the onset of the COVID-19 crisis 11.1 millions flight were operated in Europe in 2019. Then, after a plummet down to just around 5 millions flights due to the 2020 lock-downs, by the end of 2022 the 83 % of the total number of flight has been already recovered. For the next 7-years (2022-2028), long-term forecasts predict a further increase in the total number of flight up to 13 millions, with a growth of around the 18 % with respect to the 2019 standards. The recovery trends for Europe are shown in Figure 1.1 where it can be seen that forecasts are affected by several factors like prices inflation, fuel cost, passenger confidence and impact of the travelling restrictions due to the COVID-19 pandemic on airports and airlines.

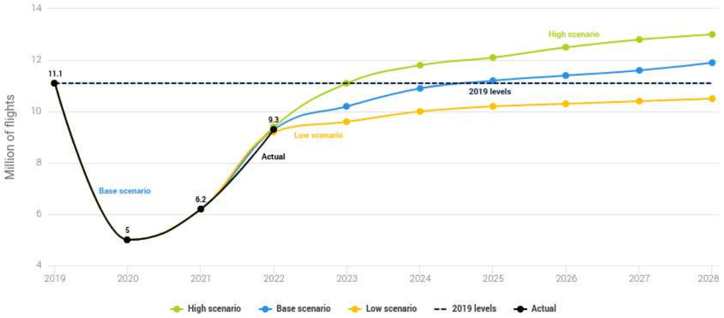

Figure 1.1: Low, medium and high scenarios of air traffic recovery in Europe.

Noise pollution is extremely annoying when aircrafts are close to the ground (e.g., takeoff, cutback and approach conditions) and noise radiated from the engines and the airframe directly strikes people living near large airports. Thus, a noise certification procedure is mandatory for any aircraft before entering into service. For this reason, all the modern propulsion systems based on ultra-high bypass ratio turbofan engines must be designed following low-noise design criteria and using more and more accurate acoustic prediction methods [2, 3]. This means that noise radiated from a turbofan engine, must be properly abated to comply with international restrictions on the maximum allow-able noise emission levels promulgated by the International Civil Aviation Organization (ICAO) [4]. More specifically, as indicated in the Flightpath 2050 document [5], aircraft noise must be abated by the 65 % with respect to the noise emission levels of the early 2000s. Under this perspective, the concept of turbofan architecture adopted by almost all the modern airplanes has already drastically reduced the engine nuisance, acting mainly on jet noise. Very iconic is the story of the Concorde supersonic airplane which was dismissed in 2003 also for noise pollution reasons because of its turbojet engines. Nonetheless, to target the 2050 objectives, further efforts in the low-noise design of aircrafts are required to meet the targets of the 2050 agenda promoting a quieter civil aviation. To this end, many strategies can be pursued acting directly on the design of engine and airframe components. It should be bear in mind that the ICAO directives are addressed to all the Landing Take-Off (LTO) cycle manoeuvres which involve the taxing out to the runway, the takeoff, the approach, the landing and the taxing in to the apron. Depending on the phase of the LTO cycle, the relative impact of each noise source to the overall noise signature of the aircraft varies, as visible in Figure 1.2.

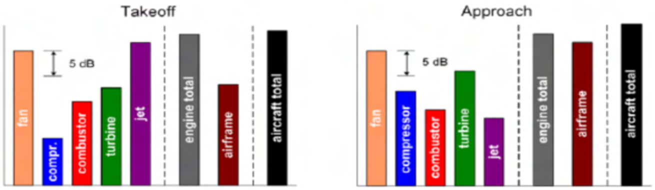

Figure 1.2: Engine and airframe noise at takeoff and approach.

As it can be seen from Figure 1.2, airframe and engine noise are almost of the same order of magnitude at approach while engine noise is the loudest at takeoff. The high impact of airframe noise at approach comes from the extraction of the wing slats and the landing gear when the aircraft is going to land. Airframe noise is broadband and at low frequency since it is the result of large whirling phenomenon set in the slat cove or vortex detachment from the landing gear struts. Many studies can be found in the literature addressing the airframe noise topic. Slat noise can be abated through a slat cove filler attached to the slat that removes flow separation creating a more aerodynamic shape of the wing trim. Effects of the cove filler on slat noise reduction can be found in [6, 7, 8, 9]. With regard to landing gear noise, this is due to the bluff shape of the structure and it can be demonstrated that scales with the 6^{th} power of the flow velocity [10]. Hence, to shield the landing gear and reduce the local airflow speed, fairings can be applied to any component of the landing gear [11, 12, 13].

Focusing just on the engines, the two major noise sources are the fan and the exhaust jet which contributes the most to the engine noise footprint when the aircraft is ready to depart. Moreover, an almost constant contribution of the fan is observed at both the takeoff and approach phases. This is directly linked to the turbofan architecture in which the fan plays the major role in generating the engine thrust. In addition, looking at Figure 1.3 it can be noted that fan noise is radiated frontward while jet noise rearward. Furthermore, fan noise is mainly tonal and it is generated by unsteady interactions between the fan blade rotating wakes and the Outlet Guide Vane (OGV) leading edges. On the other hand, jet noise is broadband coming from turbulence decay of detached shear layers originated when

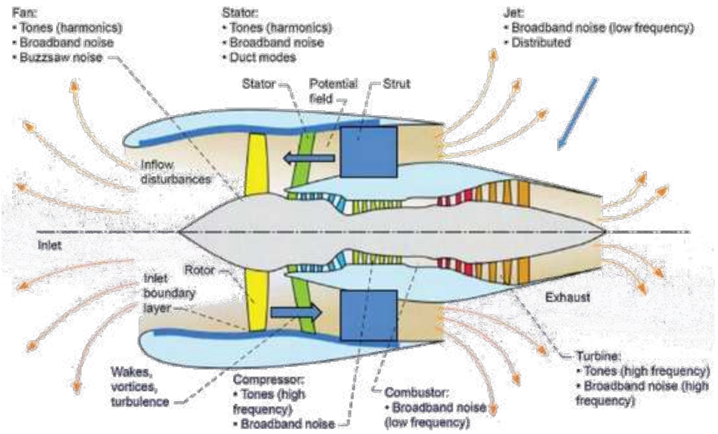

Figure 1.3: Noise sources of turbofan engines.

the jet flows into the atmosphere. As a consequence of the different nature (i.e., tonal or broadband) of fan and jet noise, two different devices are commonly employed to properly take them: acoustic liners and chevron nozzles. The design and the acoustic absorption assessment of such devices through high-fidelity Computational Fluid Dynamics (CFD) and Computational Aero-Acoustics (CAA) methods will be the core of the present work of thesis, as discussed in the dedicated chapters. In the following section, a focus on high-fidelity CFD and its role in the aero-acoustic design of aeronautical engine components is provided.

1.2 High-fidelity CFD

High fidelity methods for CFD are a class of numerical techniques aimed at overcoming the limitations of traditional Reynolds-Averaged (RANS) approaches when dealing with turbulent flows.

The core of these methods is to numerically solve the turbulent content of any kind of flow instead of using turbulence modelling. Doing so, a higher accuracy of the CFD simulation is reached enabling the in-depth investigations of engineering problems that could not be tackled otherwise. On the other hand, the augmented resolution of the high-fidelity approach brings with it a huge computational cost of the calculations, requiring a higher level of parallelism of such CFD simulations. For this reason, in the last years the scientific community has oriented its efforts on massive developments of high parallel computing (HPC) platforms to drastically reduce the time needed to run high-fidelity CFD. As a result, modern supercomputers equipped with graphical processing units (GPU) of latest generation have accomplished the task, showing an impressive speed-up with respect to the older ones based on central processing unit (CPU) architectures. According to [14], the newest GPU-based systems outperform the CPUs-based ones by around one order of magnitude in terms of billion of floating point operations per second (GFLOPS). This means that results from large CFD simulations that originally might have last for weeks, can be now obtained in a few days. The evolution of CPU and GPU architectures during the years is reported in Figure 1.4 for single precision operations. In the field of the CFD, GPU implementations can be found in many scientific areas, ranging from medicine to engineering to meteorology. For this reason, GPU-based solvers have been developed for a large variety of flows, from incompressible [15, 16] to multi-phase [17] and reactive [18].

From the point of view of the aeronautical industry, high-fidelity CFD has become very promising to increase the accuracy of unsteady analyses and to improve the numerical-to-experimental correlation of data. Generally speaking, high-fidelity

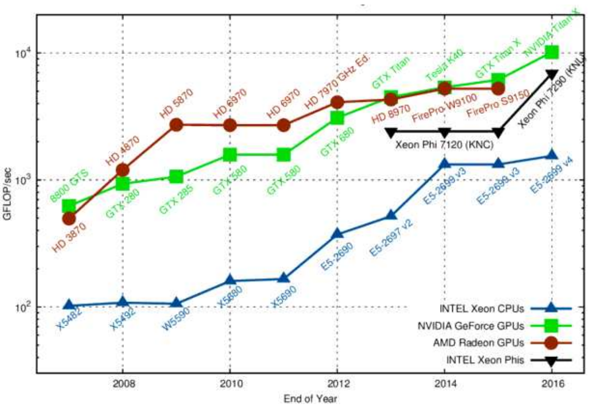

Figure 1.4: Temporal evolution of CPU and GPU performance.

CFD is a powerful tool to design aero-engines that must comply with both performance and environmental requirements. For instance, with regard to the aero-acoustic field, scale-resolved simulations help having a deeper insight on the physical mechanisms behind phenomena like noise generation from aerodynamic sources and its propagation through the engine. These techniques are also useful to support the designer of noise reduction devices as acoustic liners and chevron nozzles. Looking instead at the engine aerodynamics, an accurate analysis of the boundary layer transition in low pressure turbine stages leads to a better characterization of the turbine losses and hence to improvements in the aerodynamic efficiency of the entire engine, with beneficial effects also on fuel consumption. Other applications of the high-fidelity CFD within the aviation framework are related to the design of modern combustion chambers. Here, high-fidelity multi-phase simulations of fuel atomization can provide a better understanding of how the liquid phase breaks up and the fuel droplets are spread inside the combustor volume helping in the design of the injection and the sparkling devices. Moreover, a detailed simulation of the swirling flow entering the combustion chamber can provide more accurate heat transfer coefficient maps on the liner walls thus optimizing the design of the cooling systems. Finally, high-fidelity CFD can be useful also for in-depth aero-elastic analyses that may be required for slender blades of turbine modules. More specifically, high-fidelity methods can highlight the spectral content of the aerodynamic forces due to rotor-to-stator interactions, enabling more accurate flutter and forced responses investigations. Besides the aviation and turbomachinery fields, high-fidelity CFD methods are widely used in many other engineering contexts. An increasing demand of high-fidelity calculations comes from wind industry especially for the characterization of stalled-flow working conditions of wind turbine blades. Stalled airflow around wind turbine blades can frequently occur due to both power regulation strategies and sudden changes of wind direction and intensity. After the stall onset, the prediction of the airfoil performance through analytical and traditional CFD methods is usually inaccurate due to the unreliability of mathematical correlations and turbulence models in case of massively separated flows. Another engineering field for which high-fidelity CFD is becoming appealing is the automotive sector. Here, major applications are concerned with the aerodynamic design of motor-sport vehicles and noise emissions coming from side-view mirrors of cars.

With the aim of clarifying the objectives of the present work of thesis, the two main activities on acoustic liners and chevron nozzles conducted during the three years of Ph.D. are briefly described below:

1. **Investigation on acoustic liners**: the research has been focused on the acoustic absorption achieved through the in-

stallation of acoustic liners on the inner surface of a turbofan intake. More specifically, the high-fidelity Large Eddy Simulation (LES) approach has been exploited to understand the fluid mechanisms that lead to noise suppression and to design the acoustic liner resonators. Multiple liner configurations have been analysed from single to multi cavity systems.

2. **Investigation on exhaust nozzles**: The high-fidelity Delayed Detached Eddy Simulation (DDES) approach has been coupled with a CAA method based on the Ffwocs-Williams-Hawkings analogy (FWH) to derive and analyse the noise spectra coming from the exhaust jet of round and chevron nozzles for aeronautical propulsion systems. This activity has been oriented to understand how to design the chevron pattern to target a certain broadband noise attenuation.

From this point on, this thesis is structured as follows:

Chapter 2: this chapter addresses the theory of turbulent flows and some aspects of CFD and CAA methods. A theoretical background on turbulence is thought to introduce the topic, then a detailed explanation on all the possible CFD approaches is given. Finally, some basis on the FWH analogy are presented to make the reader familiar with the CAA used in this work.

Chapter 3: here, the numerical tools used in this work are presented. The first and the second sections of the chapter deal with the description of the CFD code chosen to run the high-fidelity simulations. Then, in a third section the numerical implementation of the FWH analogy into the CFD code is shown.

Chapter 4: this chapter is headed by a dedicated introduction to explain how acoustic liners work and which is the state of the art of acoustic liners investigation. In the rest of the chapter, results of the high-fidelity simulations on different liner configurations are presented and deeply discussed.

Chapter 5: the structure of this chapter is the same of the previous one but focused on chevron nozzle analyses. The outcomes of the present activity are mainly intended to provide general guidelines on how to correctly set up high-fidelity simulations for jet noise investigations.

Conclusions: in this last part of the thesis final considerations are made to support the usage of the high-fidelity CFD for the aero-acoustic design of turbofan engines.

2

Fundamentals of Turbulent Flows

This chapter is organized to firstly provide a theoretical background on turbulent flows, then CFD and CAA methods are introduced in dedicated sections.

2.1 Theory of turbulence

By definition, turbulence is a stochastic three-dimensional and unsteady phenomenon that represents the equilibrium state of any flow [19]. From a microscopic perspective, turbulence can be defined as the chaotic motion of fluid particles whose velocity varies both in space and time. This leads to a subsequent enhancement of the mass, momentum and energy transport mechanisms with respect to laminar flows. The turbulent state of a flow is expected at high Reynolds numbers when instabilities grow and perturb the parallel motion of fluid particles. Turbulence is a spectral quantity that is inserted into the flow under the form of turbulent eddies, each one characterized by a length scale and carrying a certain amount of turbulent kinetic energy.

The majority of the turbulent kinetic energy is inserted into the mean flow at the largest scales, which are usually referred as the integral scales, through a production mechanism. Hence, these scales break down into smaller scales and the process continues until the viscous length scale is reached. During this process known as energy cascade, turbulent kinetic energy is transferred the from larger to smaller eddies. In a first phase, turbulent kinetic energy is just redistributed over smaller scales by an inviscid process that preserves the turbulent content of the flow. Then, when approaching the so-called Kolmogorov scales, viscous effects become prominent, turbulent kinetic energy is dissipated into heat by the flow shear stresses and the energy cascade stops. The sum of the kinetic energy contributions coming from all the eddies of the cascade determines the turbulent spectrum at a specific location somewhere in a three-dimensional fluid domain. According to Richardson [20], an eddy is a region of the flow where a turbulent motion occurs and eddies of different size may coexist in the same region. Each eddy of length scale l has a characteristic velocity $u(l)$ and a characteristic time $\tau(l)$, hence an eddy Reynolds number can be defined as $Re = ul/\nu$. The largest eddies are of the same dimension of the flow scale and their velocity is approximately the root mean square turbulence intensity. Being k the turbulent kinetic energy and using the *0* subscript to label integral scales, from Richardson's assumption it holds:

$$u_0 = u' = \sqrt{\frac{2k}{3}}; \quad Re_0 = \frac{u_0 l_0}{\nu} \tag{2.1}$$

Another important finding was that the rate of dissipation ϵ of turbulent kinetic energy at the small scales is equal to the transfer of energy due to the largest eddies. As ϵ is the derivative of turbulent kinetic energy with respect to time, in terms of eddy scales it follows:

$$\epsilon \approx \frac{u_0^3}{l_0} \tag{2.2}$$

The length scale at which the dissipation mechanism start is defined by the Kolmogorov theory [21] according to three hypotheses:

1. **Local isotropy**: *Turbulent motions at small scales are statistically isotropic.*

   This means that small scales show an universal behaviour regardless of the flow and the geometry of the largest eddies from which they have been generated. The threshold length scale below which the local isotropy assumption is retained has been set by Kolmogorov to $l_{EI} \approx l_0/6$.

2. **First similarity hypothesis**: *In every flow at high Reynolds number the small scales have a universal form that is uniquely determined by ν and ϵ.*

   This hypothesis comes from the idea that for $l \ll l_{EI}$ turbulent kinetic energy transfer and dissipation are balanced (i.e., $\epsilon \approx \tau_{EI}$). In other words, small scales dissipate almost the same amount of energy they have received from the larger ones, thus keeping a dynamic equilibrium state. Hence, once ϵ and ν have been specified, the Kolmogorov scales are defined as:

   $$l_\eta = \left(\frac{\nu^3}{\epsilon}\right)^{0.25}; \quad u_\eta = (\nu\epsilon)^{0.25}; \quad \tau_\eta = \left(\frac{\nu}{\epsilon}\right)^{0.5} \tag{2.3}$$

   At this point, by substituting Equation 2.1 into 2.2, and considering that the flow Reynolds number is approximately the one of the largest eddies (i.e., $Re \approx Re_0$), the ratios between integral and Kolmogorov scales can be expressed as:

$$\frac{l_\eta}{l_0} \approx Re^{-0.75}; \quad \frac{u_\eta}{u_0} \approx Re^{-0.25}; \quad \frac{\tau_\eta}{\tau_0} \approx Re^{-0.5} \tag{2.4}$$

From Equation 2.4 it can be noted that if the Reynolds number increases, the ratio between the integral and the Kolmogorov scales diminishes. As the size of the integral scale is set by the flow, this implies that a smaller Kolmogorov scale is expected. As a result, the range of scales from the integral l_0 down to the Kolmogorov l_η will be broaden as well. Therefore, the third hypothesis of the Kolmogorov theory is introduced.

3. **Second similarity hypothesis**: *in every flow at high Reynolds number the statistics of the motion of scale l in the range $l_\eta \ll l \ll l_0$ have a universal form that is uniquely determined by ϵ independent of ν.*

   From this hypothesis a second threshold length scale $l_{DI} \approx 60 l_\eta$ is introduced to express the size of the eddies below which turbulent kinetic energy is dissipated by viscous effects.

Considering all the three hypotheses, the turbulence spectrum can be split into three sub-ranges each one related to a different phase of the energy cascade. A sketch of the energy cascade splitting is shown in Figure 2.1 while the partitioning of the turbulence spectrum in Figure 2.2.

- *Energy containing range* ($l_0/6 < l < 6l_0$): this range comprises those length scales responsible for the production of turbulent kinetic energy inside a flow

- *Inertial sub-range* ($l_{DI} < l < l_{EI}$): this is the part of the spectrum at which the inviscid transfer of turbulent kinetic

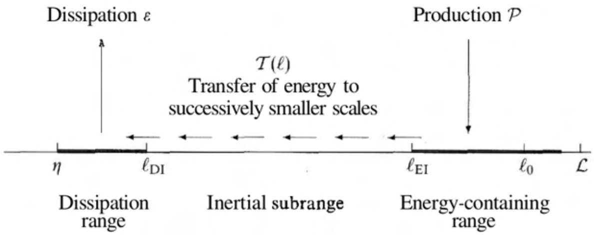

Figure 2.1: Energy cascade ranges

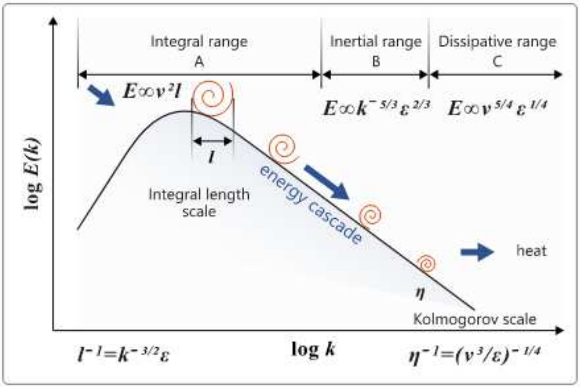

Figure 2.2: Turbulence spectrum

energy between scales takes place. In this range viscosity effects are negligible and the turbulent kinetic energy is conserved between scales.

- *Dissipation range* ($l_\eta < l < l_{DI}$): this is the last portion of the spectrum where the dimension of eddies approaches the molecular scale. Here, the viscous scales are responsible for the dissipation of the turbulent kinetic energy.

2.2 CFD methods

At this point, a brief recap on CFD is made focusing on the differences between all the possible numerical approaches that can be used to face engineering problems. From a theoretical point of view, CFD methods have been developed during the years as a computational tool to solve fluid flows for which the system of Navier-Stokes equations does not admit any analytical solution. To do so, a large number of CFD codes implements the finite volume method (FVM) [22, 23] so that the Navier-Stokes equations are rewritten in their discrete form and then integrated over finite control volumes starting from specific initial and boundary conditions. As shown in Figure 2.3, the continuous physical space occupied by the flow under investigation must be fit with a computational mesh made of polyhedral cells (i.e., the control volumes) over which the discrete Navier-Stokes equations are integrated. As a consequence, the original system of Navier-Stokes equations made of partial differential equation (PDE) is rearranged into an algebraic system that can be solved using linear algebra iterative strategies. Then, the solution of this system is stored into each cell of the mesh (in the nodes or in the cell

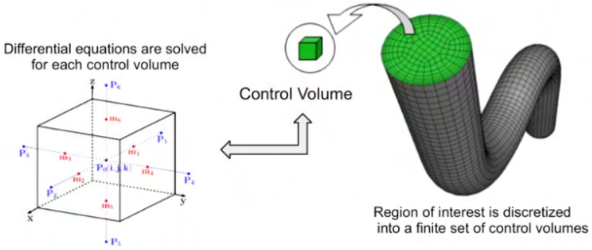

Figure 2.3: Finite volume method (FVM) illustration.

centroid) and the process is repeated until convergence. However, a direct numerical solution of the NS equations for whatever fluid flow is hardly ever attempted due to the presence of turbulence in the most relevant engineering applications. Remembering that turbulence is an intrinsically three-dimensional and unsteady feature of flows, very fine meshes and time-steps should be adopted to correctly catch all the turbulent eddies that constitute the turbulent spectrum, thus leading to too long lasting simulations. To further stress this point it can be assumed that the mesh sizing to resolve the smallest scale for a 3D simulation must be at least $\Delta x = \Delta y = \Delta z = l_\eta$, and the time-step $\Delta t = \tau_\eta$. With this assumptions, the ratios between integral and viscous scales can be interpreted as the total number of mesh cells and the total number of time-steps needed to run a direct numerical simulation (DNS). From the Kolmogorov theory explained in the previous section it has been demonstrated that the ratio between the integral and the viscous length scales is proportional to $Re^{0.75}$ while in terms of time scales to $Re^{0.5}$. In conclusion, it can be stated that the computational effort of a DNS scales approximately with the product $Re^{0.75} Re^{0.5} \approx Re^3$. This means that DNS approach is even more computationally expensive as the Reynolds number of the flow is high, making unfeasible to use this method for most of the practical applications. Moreover, these kind of simulations require local information about turbulence at the domain boundaries that is often unavailable from experimental campaigns. For these reasons, turbulence models have been developed with the aim of mimicking the effects of turbulence on the mean flow variables without solving the turbulent length scales. This has brought to the birth of the so-called Reynolds-Averaged Navier Stokes (RANS) approaches that have drastically reduced the computational effort of simulations making feasible to extend CFD methods also to the industrial field. On the other hand as stated in the Introduction, some engineering applications cannot rely on turbulence modelling as they need an accurate resolution of turbulent flows to be meaningful. For instance, broadband noise is generated by turbulence, thus at least the largest eddies of the turbulent spectrum must be solved to determine the noise level somewhere in the space. Hence, to combine the accuracy of a DNS with the low computational effort of a RANS, a wide range of hybrid CFD methods have been proposed through the years, ranging from the Scale Adaptive Simulation (SAS), to the Detached Eddy Simulation (DES) to the Large Eddy Simulation (LES). Thereby, a breakdown of all the possible CFD approaches can be based on the percentage of the turbulent spectrum that the CFD method solves. A summary of all the existing CFD methods is reported in Figure 2.4. In the rest of the section, dedicated paragraphs are intended to separately deepen some aspects of each CFD technique family mentioned so far.

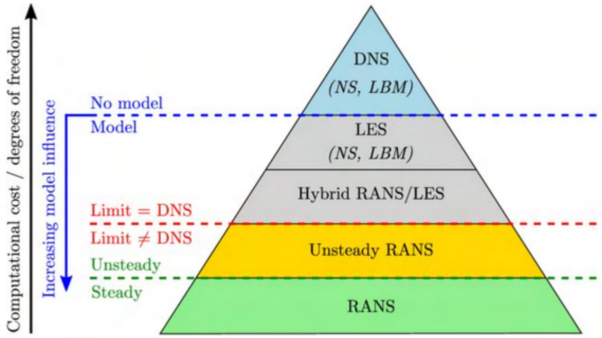

Figure 2.4: CFD methods hierarchy in ascending order of accuracy.

2.2.1 Reynolds Averaged Simulation - RANS

The RANS approach [24] is the state of the art of numerical simulation for many industrial applications due to its ease of setup, running and post-processing. This comes from the usage of turbulence models which strongly reduce the impact of initial and boundary conditions. The basis of the method is to consider each flow variable as the sum of a mean and a fluctuating component, describing the flow field with a time-averaged formalism. Equation 2.5 shows that the Reynolds averaging consists in taking a time-average of $f(x,t)$ over an infinite size window width.

$$\overline{f(x)} = f - f' = \lim_{\tau \to \infty} \frac{1}{\tau} \int_0^{\tau} f(x,t)\,dt \tag{2.5}$$

To account for compressibility effects of the flow, a density-weighted or Favre-averaging [25] formulation is introduced. The Favre average is linked to the Reynolds average through Equation 2.6.

$$\tilde{f(x)} = f - f'' = \lim_{\tau \to \infty} \frac{1}{\overline{\rho}\tau} \int_0^{\tau} \rho f(x,t)\,dt \; = \frac{\overline{\rho f(x)}}{\overline{\rho}} \tag{2.6}$$

At this point, by taking the Reynolds averaging of the Navier-Stokes system, the continuity, momentum and scalar transport equations (i.e., energy or chemical specie) are rewritten in their RANS form according to Equations 2.7, 2.8, 2.9.

$$\frac{\partial \overline{\rho}}{\partial t} + \nabla \cdot (\overline{\rho}\tilde{\mathbf{U}}) = 0 \tag{2.7}$$

$$\frac{\partial (\overline{\rho}\tilde{\mathbf{U}})}{\partial t} + \nabla \cdot (\overline{\rho}\tilde{\mathbf{U}}\tilde{\mathbf{U}}) = -\nabla \tilde{p} + \mu \nabla^{\mathbf{2}} \tilde{\mathbf{U}} + \mathbf{S_M} + \tau_{ij} \tag{2.8}$$

$$\frac{\partial (\overline{\rho}\tilde{\phi})}{\partial t} + \nabla \cdot (\overline{\rho}\tilde{\phi}\tilde{\mathbf{U}}) = \Gamma_{\phi} \nabla^{\mathbf{2}} \tilde{\phi} + S_{\phi} + \lambda_i \tag{2.9}$$

From the averaging process, the symmetric Reynolds stress tensor $\tau_{ij} = -\rho\overline{u'_i u'_j}$ and the vector $\lambda_i = -\rho\overline{u'_i \phi'}$ appear in the momentum and the scalar transport equations respectively. These terms account for the effect of turbulence on the mean variables but now a closure to the RANS system must be provided as τ_{ij} and λ_i are unknown. To do so, specific relations between the unknowns and the averaged quantities are needed. Depending on the way these unknowns are treated, two families of RANS turbulence models are obtained.

2.2.1.1 Eddy Viscosity Models

Through the Boussinesq hypothesis [26] a turbulent eddy viscosity coefficient μ_t is introduced to provide an algebraic closure for the unknown Reynolds stress tensor which is supposed to be proportional to the mean velocity gradient according to Equation 2.10.

$$\tau_{ij} = -\rho\overline{u'_i u'_j} = \mu_t \left(\frac{\partial U_i}{\partial x_j} \frac{\partial U_j}{\partial x_i} \right) - \frac{2}{3}\rho k \delta_{ij} \tag{2.10}$$

In Equation 2.10, the term in brackets is twice the mean strain rate tensor S_{ij}, k is the turbulent kinetic energy and δ_{ij} is the Kronecker delta. A similar closure yields also for the λ_i vector as given by Equation 2.11.

$$\lambda_i = -\rho\overline{u'_i \phi'} = \Gamma_t \frac{\partial \phi}{\partial x_i} \tag{2.11}$$

Here, the Γ_t constant can be expressed as a function of μ_t once the turbulent Prandtl or Schmidt number are known. In other words,the idea behind eddy viscosity models is to build a parallelism between motion of fluid molecules and turbulent eddies. The presence of turbulence enhances the transport mechanisms and the momentum exchange between fluid particles so that under the RANS perspective, a turbulent flow can be viewed as a laminar one with a modified viscosity $\mu_{eff} = \mu + \mu_t$. Therefore, the closure problem is reduced to the evaluation of the turbulent viscosity everywhere in the fluid domain. It is worth noting that eddy viscosity models assume isotropic turbulence, although this approximation does not hold for the largest energy-carrying eddies. At this point, from the gas kinetic theory it can be assumed $(\mu_t/\rho) \propto u^* l^*$, where u^* and l^* are the eddy mixing velocity and length. Equation 2.10 can be recast in Equation 2.12 for a 2D flow, highlighting the contribution of u^* and l^* to turbulent eddy viscosity.

$$\tau_{xy} = \frac{1}{2}\rho l^* u^* \frac{\partial U}{\partial y} \tag{2.12}$$

Algebraic or differential formulations can be used to express the velocity and the mixing length, determining a vast set of RANS turbulence models that can be grouped into three major categories.

1. **Algebraic models**

   These models can be referred also as zero-equation models as the velocity and the mixing length are not calculated through transport equations. Depending on the way these mixing lengths are derived, different algebraic models are built. Among these models, the very first one was developed by Prandtl [27] who considered the mixing velocity u^* as a function of the mixing length l^* which in turn was supposed to be proportional to the wall distance.

   $$u^* \approx l^* \left| \frac{\partial U}{\partial y} \right|; \quad l^* \approx y_w \tag{2.13}$$

   However, Equation 2.13 suggests that according to the Prandtl model, the turbulent time scale (i.e., l^*/u^*) is of

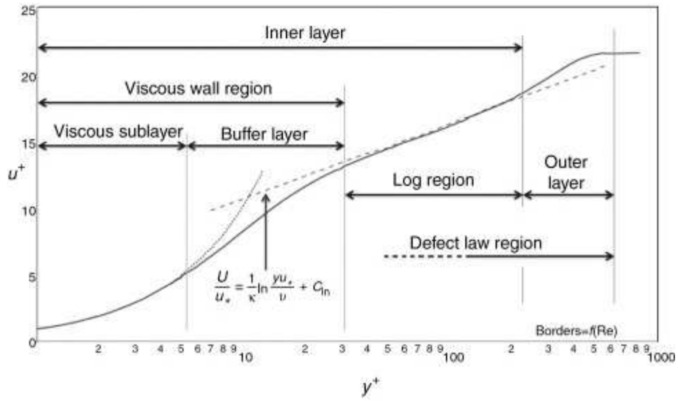

Figure 2.5: Law of the wall for turbulent boundary layers

the same order of magnitude of the integral time scale (i.e., dy/dU) violating the hypothesis of isotropic turbulence. For this reason, some modifications were needed to properly model the turbulent boundary layer. Starting from the law of the wall over a flat plate shown in Figure 2.5, Prandtl and Von Karman introduced a proper mixing length to model turbulence in each layer of a turbulent boundary layer (i.e., viscous sub-layer, log layer, defect layer) so that:

$$\begin{cases} l^* = y_w^2 \text{ sub-layer} \\ l^* = k y_w \text{ log layer} \\ l^* = \delta(x) \text{ defect layer} \end{cases} \tag{2.14}$$

In Equation 2.14, $k = 0.41$ is the Von Karman constant while $\delta(x)$ is the boundary layer displacement thickness. Subsequently, van Driest [28] proposed the damping function in Equation 2.15 to reproduce the near-wall behaviour of turbulent eddy viscosity, taking the coefficient $A^+ = 26$.

$$l^* = ky_w(1 - e^{-y^+/A^+}) \tag{2.15}$$

Furthermore, Clauser [29] corrected the eddy viscosity in the defect layer while Kays and Moffat [30] adapted the original model to pressure gradient flows, making the A^+ parameter a function of the local pressure gradient. Later on, Cebeci and Smith [31] developed a two-layer model which exploits an inner and outer eddy viscosity coefficients to reconstruct the law of the wall.

$$\begin{cases} \mu_t = \mu_{ti} \text{ for } y \leq y_m \\ \mu_t = \mu_{to} \text{ for } y > y_m \end{cases} \tag{2.16}$$

The general formulation of such models is expressed in Equation 2.16 where y_m is the wall distance at which $\mu_{ti} = \mu_{to}$. At this point, the closure is provided specifying an algebraic law for the inner and outer contribution of the eddy viscosity. Due to the difficulty in computing the displacement thickness for separated flows, Baldwin and Lomax [32] revised the formulation of the outer eddy viscosity of the Cebeci-Smith model, developing a more versatile two-layer model. Nevertheless, both these models were designed to include pressure gradient terms, streamline curvature, surface roughness and the laminar-to-turbulent boundary layer transition. Although algebraic models do not provide any information of the transport of turbulence inside the flow, they have been widely used for industrial applications due to their robustness and easiness of implementation into a CFD code.

2. **One-equation models**

One differential equation is added to the original Navier-Stokes system to determine how turbulence is transported into the fluid domain. Hence, the eddy viscosity is supposed to be a function of a scalar selected to express the turbulence content of the flow. Doing so, non local effects and the temporal evolution of turbulent eddies are included in the modeling, overcoming the main deficiency of algebraic models. The first one-equation differential model was developed by Prandtl [33] who chose the turbulent kinetic energy ($k = \frac{1}{2}\overline{u_i'u_i'}$) to describe the transport of turbulence inside a flow. Therefore, he linked the eddy viscosity to turbulent kinetic energy through Equation 2.17, although a mixing length must be provided to close the model.

$$\mu_t \propto \rho l^* \sqrt{k} \tag{2.17}$$

The transport equation for the turbulent kinetic energy was derived by Prandtl from a manipulation of the momentum equations leading to:

$$\rho\frac{\partial k}{\partial t} + \rho U_j \frac{\partial k}{\partial x_j} = \tau_{ij}\frac{\partial U_i}{\partial x_j} - \rho\epsilon + \frac{\partial}{\partial x_j}\left[\mu\frac{\partial k}{\partial x_j} - \frac{1}{2}\rho\overline{u_i'u_i'u_j'} - \overline{p'u_j'}\right] \tag{2.18}$$

Equation 2.18 implies that the transport of the kinetic energy (LHS) must be balanced by production, dissipation and diffusion terms (RHS) everywhere inside the flow. The dissipation and the diffusion terms of Equation 2.18 can be expressed through Equations 2.19 and 2.20

$$\frac{1}{2}\rho\overline{u_i'u_i'u_j'} - \overline{p'u_j'} = -\frac{\mu_t \partial k}{\sigma_k \partial x_j} \tag{2.19}$$

$$\epsilon = \nu \overline{\frac{\partial u_i' \partial u_i'}{\partial x_k \partial x_k}} = C \frac{k^{3/2}}{l} \tag{2.20}$$

The C parameter in Equation 2.20 is a closure coefficient derived by experimental evidence.

From the Prandtl model, another one-equation differential model was derived by Spalart and Allmaras in 1992 [34]. In this model the turbulent variable is a modified kinematic viscosity $\tilde{\nu}$ which is directly correlated to the eddy viscosity through Equation 2.21. Here, f_{v1} is a function of the ratio $\chi = \frac{\tilde{\nu}}{\nu}$, being ν the kinematic viscosity of the fluid.

$$\mu_t = \rho \tilde{\nu} f_{v1} \tag{2.21}$$

The transport of the $\tilde{\nu}$ variable is given by Equation 2.22.

$$\frac{\partial \tilde{\nu}}{\partial t} + U_j \frac{\partial \tilde{\nu}}{\partial x_j} = c_{b1} \tilde{S} \tilde{\nu} + \frac{1}{\Gamma} \left[\frac{\partial}{\partial x_k} \left((\nu + \tilde{\nu}) \frac{\partial \tilde{\nu}}{\partial x_k} \right) + \right. \\ \left. + c_{b2} \frac{\partial \tilde{\nu} \partial \tilde{\nu}}{\partial x_k \partial x_k} \right] - c_{w1} f_w \left(\frac{\tilde{\nu}}{d} \right)^2 \tag{2.22}$$

The reader may refer to [34] for further details on model constants and damping functions.

3. **Two-equation models**

Exploiting a second differential equation allows for a more precise characterization of the turbulence transport since no length scale must be issued a priori. In addition to the kinetic energy equation (Eq. 2.18), a dissipation equation describes how turbulence is dissipated into thermal energy. To this end, the turbulent dissipation per mass unit ϵ or the turbulent dissipation per turbulent kinetic energy unit

$\omega = \frac{\epsilon}{k}$ are commonly selected as the transported scalar of the second equation. In the first case, the model is called $k - \epsilon$ while in the second one $k - \omega$. Due to the presence of many unknown terms, the standard versions of the $k - \epsilon$ model is attributed to Launder and Spalding [35] who used the following dissipation equation:

$$\rho\frac{\partial \epsilon}{\partial t} + \rho U_j \frac{\partial \epsilon}{\partial x_j} = C_{e1}\frac{\epsilon}{k}\tau_{ij}\frac{\partial U_i}{\partial x_j} - C_{e2}\rho\frac{\epsilon^2}{k} + \frac{\partial}{\partial x_j}\left[\left(\mu + \frac{\mu_t}{\sigma_e}\right)\frac{\partial \epsilon}{\partial x_j}\right] \tag{2.23}$$

On the other hand, the most widely used formulation of the $k - \omega$ model is the one proposed by Wilcox [36] whose dissipation equation is:

$$\rho\frac{\partial \omega}{\partial t} + \rho U_j \frac{\partial \omega}{\partial x_j} = \alpha\frac{\omega}{k}\tau_{ij}\frac{\partial U_i}{\partial x_j} - \beta\rho\omega^2 + \frac{\partial}{\partial x_j}\left[(\mu + \mu_t\sigma)\frac{\partial \omega}{\partial x_j}\right] \tag{2.24}$$

At this point, depending of which model is used, the eddy viscosity can be written as:

$$\mu_t \propto \rho\frac{k^2}{\epsilon}; \quad \mu_t \propto \rho\frac{k}{\omega} \tag{2.25}$$

Basically, the rearrangement of the $k - \epsilon$ model into the $k - \omega$ comes from some limitations of the $k - \epsilon$ for wall-bounded flows. More precisely, the $k - \epsilon$ model cannot be integrated down to the wall and it requires wall functions to model the boundary layer. Furthermore, it is not very accurate in case of adverse pressure gradients, leading to wrong predictions of the separation onset for separated flows. On the contrary, the $k - \omega$ model is well suited to predict the flow close to solid walls and it can be also adapted for low Reynolds applications. This can be done by modifying some of the model constants introducing a dependency upon the the turbulent Reynolds number $Re_T = \frac{k}{\omega\nu}$ to correctly capture the boundary layer transition. Another option is to blend into a single model both the $k-\epsilon$ and the $k-\omega$ so to exploit the flexibility of the first one in the free-stream region and the robustness of the second one close to the wall. This was the idea of Menter [37] who wrote the $k-\omega$ Shear Stress Transport (SST) model defining a switching function to force the model to run in the $k-\omega$ mode inside the boundary layer and in the $k-\epsilon$ mode elsewhere. The basis provided by the $k-\omega$ SST model was then used by Langtry and Menter [38] to develop the four-equation $k-\omega-\gamma-Re_\theta$ transitional model. Here the authors introduced two additional transported scalar (i.e., the intermittency γ and the momentum thickness Reynolds number Re_θ) to properly detect the transition onset and length for a wide range of flows.

2.2.1.2 Reynolds Stress Transport Models

Differently from what has been said so far, these models do not require the Boussinesq hypothesis to close the RANS equations. For all the six unknown components of the Reynolds stress tensor, a transport equation is added to the system of the Navier-Stokes equations. Doing so, each component of the Reynolds stress tensor is numerically solved and there is no need for modelling the production term of the turbulent transport. In addition, these models enable to catch the local anisotropy of the flow due to buoyancy, swirling and curvature effects that are absent in the eddy viscosity models. However, although the higher flow characterization these models provide, they are not so widely used as the eddy viscosity models. This is mainly due to the numerical instability and the higher computational effort they add to the simulation. Among the others, the most famous Reynolds Stress Transport models are the one of Launder, Reece and Rodi [39] and the one of Speziale, Sarkar and Gatski [40].

2.2.2 Large Eddy Simulation - LES

The LES method was firstly developed by Smagorinsky [41] for weather forecast, then Deardorff [42] used it for channel flow applications to overcome the limitations of the RANS methods. In the LES approach, turbulence is taken as a spectral quantity made of eddies with different length and time scales, as described in Section 1.1. The LES aims at numerically solving the turbulent content of the flow, thus velocity fluctuations of the energy carrying eddies must be captured. This means that the fluid mesh should be fine enough to properly discretize all the eddies from the energy containing range down to the upper threshold of the inertial sub-range. Further refinements of the mesh would shift the LES towards a Direct Numerical Simulation (DNS) where also eddies in the dissipation range are resolved. Due to the massive increase computational effort that a DNS would determine, eddies in the dissipation range are modelled through eddy viscosity models that are called sub-grid scale (SGS) models. In other words, the LES is a blending of the RANS and the DNS methods: it works as a DNS for the larger energy-carrying scales while it behaves as a RANS in the dissipation range, where viscous motions cannot be neglected. Therefore, a spatial filtering of the Navier-Stokes system is required taking care that the filter width size is of the same dimension of the eddies in the inertial sub-range. The need for resolving turbulence up to the dissipation range threshold lies in the isotropy of the smallest scale that can be safely modelled by an eddy viscosity model. From a computational perspective, the filtering operation consists in creating a fluid mesh whose smallest cells have a sizing at least equal to the length scale of eddies in the inertial sub-range. Thus, all the length scales smaller than the mesh sizing are modelled as sub-grid scales, while the larger ones are resolved. The separation between resolved and modelled scales is performed applying to the Navier-Stokes equation a filter function $G(\mathbf{x}, \mathbf{x}', \Delta)$ so that the filtered velocity comes from a convolution operation:

$$\tilde{u_i}(\mathbf{x}) = \int G(\mathbf{x}, \mathbf{x}', \Delta) u_i(\mathbf{x}') d\mathbf{x}' \tag{2.26}$$

In equation 2.26, x is the position vector while x' stands for the region of space surrounding the x location. The Δ parameter represents the filter width that dictates the threshold between the modelled and the resolved scales and it is usually taken as the cube root of the cell volume. Hence, the i-th component of velocity at location x can be expressed as the sum of the filtered (tilde) and the fluctuating sub-grid (prime) contributions.

$$u_i(\mathbf{x}) = \tilde{u_i}(\mathbf{x}) + u_i'(\mathbf{x}) \tag{2.27}$$

By applying the filtering operation to the incompressible Navier-Stokes equation and exploiting the commutativity properties of the convolution operation, the following system is obtained:

$$\frac{\partial \tilde{u_i}}{\partial x_i} = 0 \tag{2.28}$$

$$\frac{\partial \tilde{u_i}}{\partial t} + \frac{\partial \langle u_i u_j \rangle}{\partial x_j} = -\frac{1}{\rho} \frac{\partial \tilde{p}}{\partial x_j} + \nu \frac{\partial^2 \tilde{u_i}}{\partial x_i^2} \tag{2.29}$$

Where the angular parentheses in Equation 2.29 mean the convolution operation applied to the product $u_i u_j$. By substituting Equation 2.27 into Equation 2.29, the convective term of the filtered momentum equation can be rewritten as:

$$\langle u_i u_j \rangle = \langle \tilde{u_i} \tilde{u_j} \rangle + (\langle \tilde{u_i} u'_j \rangle + \langle u'_i \tilde{u_j} \rangle + \langle u'_i u'_j \rangle) \tag{2.30}$$

The first addendum in the RHS of Equation 2.30 is equal to the product of the filtered velocity components while the quantity in round brackets is the sub-grid stress tensor τ_{sgs}. More specifically, it can be noted that the overall sub-grid effect on the resolved variable comes from the interaction between sub-grid scales R_{ij} and the cross interaction between resolved and sub-grid scales C_{ij}.

$$R_{ij} = \langle u'_i u'_j \rangle; \quad C_{ij} = \langle \tilde{u_i} u'_j \rangle + \langle u'_i \tilde{u_j} \rangle \tag{2.31}$$

Thus, by inserting Equation 2.31 into Equation 2.29 it yields:

$$\frac{\partial \tilde{u_i}}{\partial t} + \frac{\partial \tilde{u_i} \tilde{u_j}}{\partial x_j} = -\frac{1}{\rho} \frac{\partial \tilde{p}}{\partial x_j} - \frac{\partial \tau_{sgs}}{\partial x_j} + \nu \frac{\partial^2 \tilde{u_i}}{\partial x_i^2} \tag{2.32}$$

According to the way the unknown τ_{sgs} tensor is modelled, different LES turbulence model are derived. The most intuitive way is to provide an algebraic closure for τ_{sgs} making it a function of a sub-grid eddy viscosity ν_{sgs}. Among the variety of sub-grid models available from literature, the most wide-spread ones are:

1. Smagorinsky model [41]
2. Dynamic Smagorinsky-Germano-Lilly model [43, 44]
3. Wall Adaptive Local Eddy Viscosity (WALE) model [45]

All these models have been developed starting from the original Smagorinsky model [41] which suggests that the sub-grid viscosity ν_{sgs} is a function of the resolved strain rate tensor:

$$\nu_{sgs} = (C_s\Delta)^2|\tilde{S_{ij}}| = \frac{1}{2}(C_s\Delta)^2\left|\left(\frac{\partial\tilde{u_i}}{\partial x_j}+\frac{\partial\tilde{u_j}}{\partial x_i}\right)\right| \tag{2.33}$$

where Δ is the filter width and C_s is the Smagorinsky constant equal to 0.1. However, it has been found that the C_s constant should be tuned according to the type of flow under examination. For this reason, dynamic versions of the model have been introduced by Germano [43] and Lilly [44] to adapt the model constant to different kind of flows, making it a function of time and space. More in detail, dynamic models exploit a second filter, whose width is larger than the one of the LES, to average the already filtered LES equation. Doing so, a link between the two residual sub-grid tensor can be found and the Smagorinsky coefficient C_s can be derived from this relation. Nevertheless, another limitation of the original Smagorinsky model is the wrong prediction of eddy viscosity close to solid boundaries. Here the model predicts a maximum for the eddy viscosity while according to the law of the wall, the eddy viscosity should vanish in the laminar sub-layer. To face this issue, a van-Driest wall function is embedded into the model leading to the relation of Equation 2.34 for the sub-grid eddy viscosity.

$$\nu_{sgs} = \frac{1}{2}(C_s\Delta)^2(1-e^{-y+/25})^2\left|\left(\frac{\partial\tilde{u_i}}{\partial x_j}+\frac{\partial\tilde{u_j}}{\partial x_i}\right)\right| \tag{2.34}$$

A more detailed characterization of the sub-grid eddy viscosity is provided by the WALE model of Nicoud and Ducros [45].

$$\nu_{sgs} = (C_w\Delta)^2\frac{(\tilde{S^d_{ij}}\tilde{S^d_{ij}})^{3/2}}{(\tilde{S_{ij}}\tilde{S_{ij}})^{5/2}+(\tilde{S^d_{ij}}\tilde{S^d_{ij}})^{5/4}} \tag{2.35}$$

In Equation 2.35, $\tilde{S^d_{ij}}$ is the deviatoric component of the resolved strain rate tensor and C_w is a model constant. This model can be intended as an upgraded version of the Smagorinsky model that is well suited also for wall-bounded flows. The WALE model does not need a damping function as the sub-grid closure has been rewritten to consider the real behaviour of eddy viscosity at wall. Moreover the model also includes the back-scattering of turbulent kinetic energy from smaller to larger scales that was not originally considered in the Smagorinsky model. Finally, as in the WALE model the sub-grid eddy viscosity is a function of both the strain and the rotation rates, the model correctly detects the stream regions where the turbulent kinetic energy is concentrated. In light of these considerations, it can be concluded that the Smagorinsky model is reliable for LES of free flows (e.g., jets in cross-flow, shear layers, vortex detachment) while the WALE model is preferable for the simulation of wall-bounded flows (e.g., flow over flat plates, airfoils, channel flow).

2.2.3 Detached Eddy Simulation - DES

This approach was developed by Spalart [46] in 1997 and consists in a blending of both the RANS and the LES formulations into a single simulation. The need for such a hybrid method comes from the too high computational cost of running a wall-resolved LES (WRLES) for wall bounded flows, especially at the high Reynolds number. It should be reminded that approaching the wall, the size of the eddies scales with the wall distance. At the same time, the size of the largest eddies is approximately the boundary layer thickness which is expected to thin for high Reynolds flows. Therefore, from a computational point of view it would be unfeasible to run WRLES as too fine meshes should be designed to detect the near wall eddies. On the other hand, in case of massively separated flows, RANS techniques usually fail in accurately solve the flow features, leading to poor quality results. For this reason, the idea behind a DES simulation is to run into RANS mode inside the attached boundary layer while the LES mode is restored in the detached flow regions (e.g., wakes, shear layers, separation bubbles, etc). The DES is a non-zonal approach, meaning that the switching between the RANS and the LES modes is based on a crossover distance that is run-time calculated and not set a priori. More specifically, a RANS and a LES-based length scales are defined and a local comparison between them is taken at each mesh point. As long as the RANS length scale is smaller than the LES one ($L_{RANS} < L_{LES}$) a near-wall region is detected and the RANS mode is enabled. If instead ($L_{RANS} > L_{LES}$), the simulation runs into LES mode as very little viscous effects are expected far from the walls. The definition of the RANS length scale depends on the selection of the turbulence model that is enabled in the near-wall region: common choices are the one-equation Spalart-Allmaras [34] or the two-equation $k - \omega$ of Wilcox [36]. The LES length scale is always taken proportional to the local grid sizing, so that $L_{LES} = C_{DES}\Delta$. The C_{DES} constant is set to 0.65 and it is calibrated on the decay of homogeneous turbulence according to Shur [47].

With regard to the Spalart-Allmaras version of a DES (SA-DES), the distance d in the destruction term of Equation 2.22 is replaced by the modified distance:

$$\tilde{d} = min(d, C_{DES}\Delta) \tag{2.36}$$

From Equation 2.36 it can be observed that the original Spalart-Allmaras model is recovered for $d \ll \Delta$ while a one-equation sub-grid model is obtained for $d \gg \Delta$. Similar considerations hold also in case of a $k-\omega$ DES, just taking the RANS length scale as $L_{RANS} = \sqrt{k}/\beta^{*}\omega$. To ensure that the RANS mode is activated in the attached boundary layer, the Δ is taken as:

$$\Delta = max(\Delta_x, \Delta_y, \Delta_z) \tag{2.37}$$

As fluid meshes are always stretched in the stream-wise direction along solid surfaces, it is very likely that Δ_x will be the maximum of Equation 2.37. This is important to prevent the activation of the LES mode too close to the wall that could happen if the Δ was equal to the cube root of the cell volume. This is an issue as the stream-wise resolution of a DES mesh is set to target RANS quality criteria and an early activation of the LES mode would result in an incorrect prediction of the wall shear stress.

However, basing the switching between the RANS and the LES models just on the mesh might lead to early activation of the LES in those region where the mesh is refined in multiple directions. For instance, in high-curvature regions (e.g., airfoil leading edge) the mesh is usually refined both in the wall-normal and in the stream-wise directions: here it can happen that $L_{LES} < L_{RANS}$ although at wall the mesh is not intended for scale-resolved simulations. The major drawback of running into LES mode on a low-fidelity mesh is the anticipation of the separation onset due to the underestimation of the local wall shear stress. This numerical issue, referred as Grid Induced Separation (GIS), has made the original DES method not so appealing for complex flow applications in which local refinements of the mesh are unavoidable. To tackle the problem a first modification of the original formulation was proposed by Spalart [48] leading to the Delayed Detached Eddy Simulation (DDES). To prevent the GIS, the idea of Spalart was to alter the switching mechanism embedding a shielding function in addition to the mesh design parameters. Thus a DDES reads:

$$L_{DDES} = L_{RANS} - f_d max(0, L_{RANS} - L_{LES}) \tag{2.38}$$

where f_d is the shielding function defined by Equation 2.39.

$$f_d = 1 - \tanh{(8r_d)^3}; \quad r_d = \frac{\mu + \mu_t}{\rho(kd)^2 max[\frac{\partial u_i}{\partial x_j}\frac{\partial u_i}{\partial x_j}, 10^{-10}]} \tag{2.39}$$

From Equation 2.38 it can be noted that the RANS length scale is returned if the shielding function f_d tends to 0. This is consistent with the argument r_d tending to unity which is true up to the edge of the log layer of a turbulent boundary layer. Then, in the defect layer r_d diminishes reaching 0 at the edge of the boundary layer so that f_d tends to unity and the LES length scale is returned from Equation 2.38. In other words, in a DDES the switching criterion is based on both the grid sizing and the local turbulent viscosity of the flow. The shielding function ensures that the LES mode is enabled in regions where the magnitude of the velocity gradient is much higher than viscous effects (i.e., in the defect layer and in the free-stream), enforcing the RANS approach where convective and diffusive terms of the Navier-Stokes equations have the same weight (i.e., inside the viscous layers of a turbulent boundary layer).

Despite the extended range of validity of the DDES approach, in 2008 Shur et al. [49] introduced the Improved Delayed Detached Eddy Simulation (IDDES) with the aim of upgrading the previous DDES method of Spalart [48]. Two main points are addressed by the IDDES variant:

1. **Log-Layer Mismatch (LLM):** the DDES of Spalart [48] suffers from a depletion of the RANS Reynolds stresses across the RANS-LES interface.

2. **Wall-modelled LES (WMLES) functionality:** in case of turbulent inflow prescribed in the form of energy spectrum, the IDDES of Shur [49] can act as a WMLES if the mesh sizing in boundary layer regions is fine enough to solve the energy-carrying eddies.

To include these two improvements into the DDES formulation, a length scale for the WMLES mode is defined as follows:

$$L_{WMLES} = f_B(1 + f_e)L_{RANS} + (1 - f_B)L_{LES} \tag{2.40}$$

The f_B empirical function is dependent upon the ratio between the wall distance and the grid sizing and it is designed to provide a rapid switching between RANS and LES mode in the range $0.5 < d/\Delta < 1$. According to Equation 2.41, for $f_B = 1$ the RANS mode is on, while the LES is activated for $f_B = 0$

$$f_B = min[2e^{-9\alpha^2}, 1]; \quad \alpha = \frac{1}{4} - \frac{d}{\Delta} \tag{2.41}$$

The function f_e in Equation 2.40 is intended to prevent the LLM and the depletion of the RANS stresses in the crossing zone. To do so, the f_e function is constructed to elevate the RANS stresses in the region $0 < d/\Delta < 0.5$. The in the range $0.5 < d/\Delta < 1$ the elevating function f_e coincides with f_B, tending to zero as the d/Δ ratio grows. This behaviour is needed as the LES mode should be recovered (i.e., $f_e = 0$) when the grid close to the wall is fine enough to run a WRLES. The elevating function is defined as:

$$f_e = max[(f_{e1} - 1), 0]\Psi f_{e2} \tag{2.42}$$

where in Equation 2.42, Ψ is a low Reynolds correction factor and the f_{e1} and the f_{e2} functions control the region of augmentation of the RANS stresses and the intensity of the elevation respectively. At this point the blending between the DDES and the WMLES branches is built using a modified version of the original DDES length scale of Equation 2.38, leading to:

$$\tilde{L}_{DDES} = \tilde{f}_d L_{RANS} + (1 - \tilde{f}_d)L_{LES} \tag{2.43}$$

where the blending function is defined as:

$$\tilde{f}_d = max[(1 - f_{dt}), f_B] \tag{2.44}$$

In Equation 2.44 the f_{dt} function is basically the same of Equation 2.39, taking the r_d ratio in its turbulent form r_{dt} (i.e., considering the turbulent viscosity only on the numerator). With this strategy of defining the DDES length scale, the automatic switching between the DDES and the WMLES versions of the IDDES is based on the hybrid length scale:

$$L_{IDDES} = \tilde{f}_d(1 + f_e)L_{RANS} + (1 - \tilde{f}_d)L_{LES} \tag{2.45}$$

The IDDES length scale in Equation 2.45 returns the WMLES length scale of Equation 2.40 when $\tilde{f}_d$ is equal to f_B. This happens in case of turbulent content provided at the inflow so that $r_dt \ll 1$ and f_{dt} tends to unity. On the other hand, the elevating function f_e tends to zero, restoring the modified DDES length scale of Equation 2.43.

2.3 Acoustic analogies in CAA

Acoustic analogies consist in different mathematical formulations used in aeroacoustics to model aerodynamic noise sources as sound emitters. Starting from the compressible Navier-Stokes equations, the in-homogeneous form of the acoustic wave equation can be derived. Hence, depending on the way the source term of the wave equation is modelled, three possible acoustic analogies are retrieved:

- **Lighthill analogy**: this analogy [50, 51] models the fluctuations of free flows surrounded by a still medium as a distribution of quadrupole sources in the same volume.

- **Curle analogy**: the Curle analogy [52] is a revised version of the Lighthill one accounting also for the presence of fixed solid boundaries on noise generation from aerodynamic sources.

- **Ffowcs-Williams-Hawkings analogy**: the FWH analogy [53] allows for noise predictions from sources in relative motion with respect to a hard surface. The source terms are modelled as a distribution of monopoles, dipoles and quadrupoles.

In the rest of the section some aspects about the FWH analogy are presented, as it has been used for far field noise calculations from aeronautical exhaust jets (see Chapter 5). Thus, in-depth explanation on the Lighthill and the Curle analogies are omitted, redirecting the reader to [50, 51, 52] for further details on these models.

2.3.1 The Ffowcs-Williams-Hawkings analogy

The FWH analogy is thought to extend the Lighthill theory [50] to high speed convective problems where the noise source is in relative motion with the surrounding fluid medium. Based on the conservation of compressible mass and momentum, it can be demonstrated that, given a generic surface S encompassing the noise sources, the generation and propagation of noise in the outer volume region is expressed by the inhomogeneous wave equation:

$$\frac{\partial^2 \phi}{\partial t^2} - c_0^2 \frac{\partial^2 \phi}{\partial x_i^2} = \frac{\partial^n Q_{ij}}{\partial x_i \partial x_j ...} \tag{2.46}$$

Where ϕ is a generalized variable and Q_{ij} represents a distribution of a n-th order multipole. Thus, once a formulation for the Q_{ij} source term is provided, a solution for Equation 2.46 can be derived, mapping the acoustic field everywhere outside the solid surface S. According to the FWH formulation, Equation 2.46 can be expressed in terms of pressure fluctuation p' and recast in the following form:

$$\begin{aligned} \frac{1}{c_0^2}\frac{\partial^2 p'}{\partial t^2} - \frac{\partial^2 p'}{\partial x_i \partial x_j} = \frac{\partial^2}{\partial x_i \partial x_j}[T_{ij}H(f)] - \frac{\partial}{\partial x_i}\{[P_{ij}n_j + \\ + \rho u_i(u_n - v_n)]\delta(f)\} + \frac{\partial}{\partial t}\{[\rho_0 v_n + \rho(u_n - v_n)]\delta(f)\} \end{aligned} \tag{2.47}$$

Where:

- u_i is the flow velocity projected onto the x_i direction
- u_n is the flow velocity normal to the surface described by the function $f = 0$
- v_i is the surface velocity projected onto the x_i direction

- v_n is the surface velocity normal to the surface described by the function $f = 0$
- T_{ij} is the Lighthill stress tensor
- $\delta(f)$ is the Dirac delta
- c_0 is the speed of sound
- P_{ij} is the compressive stress tensor
- $H(f)$ is the Heaviside step function

From the list above, the Lighthill and the compressive tensors can be expressed respectively through Equations 2.48 and 2.49.

$$T_{ij} = \rho u_i u_j + P_{ij} - c_0^2(\rho - \rho_0)\delta_{ij} \tag{2.48}$$

$$P_{ij} = p\delta_{ij} - \mu\left[\frac{\partial u_i}{\partial x_j} + \frac{\partial u_j}{\partial x_i} - \frac{2}{3}\frac{\partial u_k}{\partial x_k}\right] \tag{2.49}$$

It can be shown that a solution to Equation 2.47 holds in the form of a free-space Green function. Thus, the acoustic pressure field $p'(\mathbf{x}, t)$ can be expressed as a summation of surface and volume integrals where the firsts represent the contribution to the overall noise from monopoles and dipoles and the seconds the one coming from quadrupoles (i.e., turbulence noise). As the mathematical passages to find the solution to Equation 2.47 are quite complicated and given that this is not the aim of the section, no further details are provided hereafter. The full discussion about this topic is available in [53].

On the other hand, important considerations can be made upon the choice of the FWH surface. Firstly, the FWH analogy is applicable to both stationary and moving surfaces. Moreover, the integration surface can be permeable, meaning that it can wrap around whatever fluid region so that there is no need for taking it coincident with the solid moving wall. In this case, the solution to Equation 2.47 will return also the contribution of quadrupole sources enclosed by the permeable surface. From a CFD perspective, this implies that the volume mesh within the FWH surface should be kept fine enough to properly catch all the noise sources. At the same time, the permeable surface should be carefully drawn ensuring that it includes all the sources resolved by the chosen numerical method. In conclusion, these two requirements turn into a well defined positioning of the FWH surface inside the fluid domain if noise from quadrupole sources is the main topic of the CFD investigation. An example is noise radiated from turbulent jets for which all the acoustic footprint comes from the turbulent structures generated at the nozzle exhaust. This topic is faced and widely discussed in Chapter 5.

3

Numerical Methods

In this chapter the numerical tools chosen to set up, run and post-process the LES computations are presented. Firstly, an overview on the open-source OpenFOAM [54] suite used in this work is given, focusing on how to properly build up the simulation workspace. Special care is taken to describe all the steps required to run aero-acoustic LES within the OpenFOAM framework. Then, in the second section of the chapter the meshing library CFMesh [55] for mesh generation is presented. The latter is an open-source tool implemented into the OpenFOAM suite, that has been used in this work to create meshes on aeronautical nozzles (see Chapter 4). With regard to the acoustic liner investigation (see Chapter 3), pre-processing operations involving the domain and the mesh creation have been handled by the open-source SALOME [56] software which will not be further described in this thesis. The reader may refer to the online user-guide [57] of the SALOME platform for further details about the software functionalities.

3.1 The OpenFOAM suite

OpenFOAM (Open Field Operation And Manipulation) is a collection of C++ compiled libraries and executables for CFD applications. The suite comprises a vast choice of flow solvers that allow for the simulation of different thermo-fluidynamic problems (e.g., turbulent flows, multi-phase flows, conjugate heat transfer, combustion applications, aero-acoustics, etc). In addition, a large number of utilities is available to perform pre-processing and post-processing operations, ranging from mesh generation and manipulation to sophisticated analysis of the simulation results. Moreover, the open-source nature of the software enables the embedding into the suite of customized and user-programmed applications aimed at handling very specific tasks. A sketch of the OpenFOAM structure is shown in Figure 3.1.

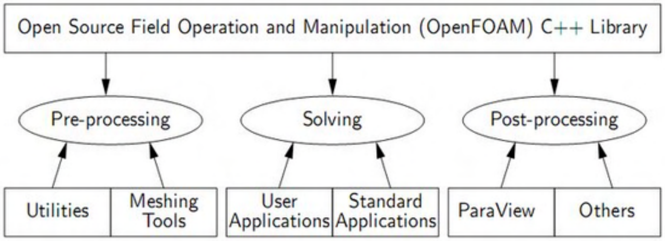

Figure 3.1: Schematic representation of the OpenFOAM suite structure.

To run a CFD simulation within the OpenFOAM framework, a hierarchical organization of directories must be followed and a minimum number of input files must be provided in the correct directory path. Each file in each directory contains specific inputs for the simulation like mesh topology information, boundary conditions, thermophysical models, simulation control settings, etc. More specifically, an OpenFOAM simulation runs into a *case* directory where the word "case" labels a user-defined name of the directory. In this mother directory, three sub-directories must be always present and labelled as: *0*, *constant* and *system*. A focus on the three directories and on their content is reported in the following paragraphs.

3.1.1 The *0* directory

The *0* directory gathers the boundary and initial condition files for each flow variable involved into the problem under investigation. Each file must be labelled accordingly to the flow variable name as listed in Table 3.1.

Variable	**File name**
Pressure	p
Velocity	U
Temperature	T
Turbulent kinetic energy	k
Turbulent dissipation rate	omega
Turbulent eddy viscosity	nut
Turbulent eddy diffusivity	alphat

Table 3.1: Flow variable file names in the 0 directory

The set of variables in Table 3.1 is the minimum required to run a compressible turbulent flow simulation using the $k - \omega$ turbulence model and a pressure-based solver. Other variables and files may be added or suppressed according to the type of the simulation (e.g., laminar, incompressible, thermal, reactive etc.) to be run. Generally speaking, the 0 directory must contain a file for each variable transported by a transport equation. The *nut* and the *alphat* files are needed to tell the simulation if wall treatments should be activated or not. In each flow variable file, specific initial and boundary conditions are set for all the domain boundaries: it is necessary that the name of the boundary region in each file is the same of the one coming out from the mesh generation.

3.1.2 The *constant* directory

In the *constant* directory the following two text files are mandatory:

- ***turbulenceProperties***: this file begins with the declaration of the simulation type (e.g., RANS, LES, DES). Then, a proper turbulence model is specified accordingly to the simulation type. In the OpenFOAM suite, a large number of RANS models is available for different kind of simulations, ranging from fully-turbulent one-equation models (i.e., Spalart-Allmaras [34]) to transitional four-equation models (Langtry-Menter k - ω SST [38]). With regard to the DES approach, the three DES97 [46], DDES [48], IDDES [49] versions are available with both the SA and the k-ω implementations as background RANS models. For LES computations, the most commonly used sub-grid models are the Smagorinsky [41] and the WALE [45] ones.

- ***thermophysicalProperties***: in this file, the working fluid properties like fluid type, equation of state, transport laws, etc. are set. Depending on the the thermophysical type that has been declared at the top of the file, other properties of the material (i.e., thermal conductivity, viscosity, density, specific heat, etc.) must be entered through specific dictionaries. In case of incompressible simulations, the *thermophysicalProperties* file is replaced by the *transportProperties* file in which just the value of the kinematic viscosity must be entered.

Next to these files, the *polyMesh* sub-directory contains all the information about the mesh topology. This sub-directory is automatically created and filled with all the necessary files when the mesh is generated. This can be done with the aid of built-in tools (e.g., *CFMesh*, *snappyHexMesh*, *BlockMesh*) or through mesh conversion utilities if the mesh is imported from external softwares. In the OpenFOAM workspace, a large choice of mesh conversion utilities is available. Among the others, in this work the *ideasUnvToFoam* utility has been invoked to translate the .unv mesh coming from the SALOME environment into a suitable FOAM format. There are five minimum mesh files produced during the mesh generation procedure, each one pointing to a specific information about the mesh structure:

- ***boundary***: this file provides information on the domain boundaries. These are outlined as a set of faces which are not shared by a couple of adjacent cells. Each boundary region is labelled with a user-defined name that must be preserved when setting the boundary conditions in the *0* directory.

- ***faces***: this file contains a ordered list of cell faces uniquely defined by the identification number (ID) of the nodes constituting them. Cell faces are then stored in an array of size equal to the total number of faces of the volume mesh.

- ***points***: in this file, the 3-D coordinates of each mesh node are listed and stored in an array of size equal to the total number of nodes of the volume mesh.

- ***owner and neighbour***: these files explicate the mesh connectivity, determining for each mesh face which is the owner cell and the neighbouring one. To do so, arrays of size N are allocated and faces are numbered from ID = 0 to ID = N accordingly to the position in the array. Thus in the *owner* file, an array is filled with the ID of the cell that owns the face at a particular position in the array. Similarly in the *neighbour* file, at each position in the array is assigned the ID of the cell that is neighbouring for that face.

3.1.3 The *system* directory

The *system* directory contains all the files for the simulation management and monitoring. Depending on the amount of pre- and post-processing activities to be performed, the number of files in this directory may vary conspicuously. However, a minimum of three files is always required to run whatever calculation:

- ***controlDict***: this is a management file in which entries like the solver selection, the maximum number of iteration, the simulation time-step, the output to disk writing interval and many others must be set according to the type of simulation it is going to run. Depending on the user needs, this file may also include the declaration of the so called *functionObjects* that address run-time operations on the mesh and the flow fields. For instance, function objects can be invoked to calculate and output derived quantities from the flow variables, to plot residuals on the fly, to perform sampling and averaging operations and so on.

- ***fvSchemes***: in this file, numerical schemes for temporal and spatial discretization of all the terms of the Navier-

Stokes and transport equations are specified. Different numerical schemes can be selected for the discretization of different terms of the same transport equation. As the list of available numerical schemes in OpenFOAM is very long, in this paragraph just the most commonly used scheme are cited. For spatial discretization, schemes are based mainly on the Gauss integration. Then, depending on the interpolation method, the order of accuracy of the numerical approximation can be adjusted. The first order upwind *Gauss upwind* [58] scheme is usually too dissipative to be recommended, unless for initialization purposes. A good trade-off between accuracy and simulation stability is provided by the second order upwind *Gauss linearUpwind* scheme [59] which is commonly set on the convective term of the momentum equation in case of RANS calculations. Another option for the discretization of the convective terms is given by the TVD family schemes [60] among which the *Gauss Van Leer* [61] and the *Gauss minmod* [62] schemes are the most used. On the other hand, when using high-fidelity DES/LES methods, at least a second order cell-centered *Gauss linear* [63] scheme should be set on all the transport equation terms to ensure high quality results. Blended and limited schemes can be also exploited to make the LES setup more robust. Finally, with regard to temporal discretization in case of unsteady simulations, the first order implicit *Euler* scheme is usually selected for RANS cases, while the more accurate second order *Crank-Nicolson* [64] or the second order implicit *backward* scheme are common choices for high-fidelity approaches.

- ***fvSolution***: in this file the numerical algorithms to solve the Navier-Stokes system of equations are declared. Since all the OpenFOAM solvers run into a segregated mode, different numerical algorithms can be selected to solve each equation separately. Furthermore, in case of pressure based solvers, the parameters of the SIMPLE [65] and PISO [66] loops are set in a dedicated section of this file. Other dictionaries can be filled in to specify relaxation factors or limiters on flow variables to improve the simulation convergence at the very first iterations.

3.2 The CFMesh library

In this section some aspects of the CFMesh [55] meshing tool are described. The CFMesh has been used in this work of thesis to create the fluid meshes around aeronautical nozzles. Details of the final meshes for rounded and chevron configurations are shown in Chapter 4.

The reason behind the choice of using the CFMesh instead of the SALOME software lies in the octree-based meshing strategy that makes CFMesh more suitable to handle complex geometries. Moreover, the tool can automatically generate cartesian, tetrahedral and polyhedral meshes directly within the OpenFOAM workspace so that no mesh conversion is needed to run simulations. In this work, the *cartesianMesh* application has been used to generate hexa-dominant meshes around the nozzle geometries under investigation in Chapter 4. To do so, the *cartesianMesh* application reads the geometry and the meshing parameters of the *meshDict* file that must be put into the *system* directory. Details on the *cartesianMesh* workflow are presented in the following paragraphs. It is worth noting that the same domain and mesh generation phases hold also for the *tetMesh* (tetra-dominant) and the *pMesh* (poly-dominant) applications.

3.2.1 Domain creation

Since CFMesh does not provide a CAD modeler, the domain geometry must be created by exploiting an external software. All the meshing algorithms implemented in the CFMesh require that the geometry to be meshed is provided as a surface triangulation. This means that to mesh 3-D volumes, the meshing applications require just a manifold shell enclosing the volume and not the volume component itself. At this point the domain geometry can be saved and exported from the external CAD software as a .stl (stereo-lithography) file. However, although the CFMesh supports the .stl format extension, it is more convenient to convert the geometry from the .stl to the .fms file format. The latter is the one preferred by CFMesh to generate meshes starting from the information collected into the input geometry file. The file format conversion can be handled by the *surfaceFeatureEdges* utility which finds edges and corners of an input triangulated surface. Once the geometry has been converted, the following geometric entities will be listed in the .fms geometry file:

- **Patches**: domain boundaries are labelled preserving the name it has been assigned to within the CAD environment. If no separate named selections have been set before the exporting phase, the whole shell will be detected as a single boundary patch. Although this is not a major issue, it implies that further mesh manipulation will be needed to correctly split and rebuild multiple boundary patches.

- **List of points**: 3-D coordinates of all the surface points are stored in an array.

- **List of triangles**: triangles are outlined as the triplet of node IDs building them.

- **List of feature edges**: edges are outlined as the couple of node IDs building them.
- **Face subsets**: these subsets are not transferred onto the volume mesh but they can be used to locate those regions where particular mesh settings are needed. Each subset contains the IDs of the faces that constitute the subset itself.

From what has been said so far it can be stated that the input geometry must be accurately shaped already within the CAD modeler, as the CFMesh utilities do nothing except from file format conversion. This means that great attention should be paid on the resolution of the final .stl file when exporting the geometry, as some features may be missing due to poor quality of the surface triangulation.

3.2.2 Mesh generation

The meshing process is based on the inputs of the *meshDict* file located in the *system* directory. Generally speaking, every mesh is generated fitting the volume enclosed by the surface shell with elements that are usually refined approaching solid boundaries or high curvature regions. Refinements are based on an octree strategy which implies that the size of the mesh elements is progressively divided by two along each coordinate direction to cluster the elements close to walls or user-defined regions of the domain. The splitting process starts from a coarse level mesh sizing and it stops once a target element size is reached in the regions of interest. This meshing procedure is very powerful as it enables complex mesh generation with low effort, efficiently redistributing the mesh elements inside the domain. As default, all the CFMesh applications (i.e., *cartesianMesh*, *tetMesh* and *pMesh*) run in parallel on all the available cores, exploiting a shared memory communication architecture. To select a reduced number of cores, the user can set the *OMP-NUM-THREADS* environment variable to the desired number of cores.

Focusing now on the *meshDict* file layout, various entries can be set to handle the mesh process and achieve high quality meshes. Details on the most relevant entries are provided in the list below:

- **surfaceFile**: this specifies the relative path to the geometry file inside the case directory.
- **maxCellSize**: this mandatory entry represents the maximum cell size generated in the domain. This is the value from which the octree algorithm starts splitting the mesh two by two.
- **minCellSize**: in regions where domain features are larger than the cell sizing, an automatic refinement is enabled until the *minCellSize* value is reached. Although this is optional, this setting quickly generates a mesh showing which regions need further manual refinement.
- **boundaryCellSize**: this optional setting enforces the refinement of the mesh at all the domain boundaries. It is possible to keep the refinement sizing for a certain distance from the boundaries setting the refinement thickness through the *boundaryCellSizeRefinementThickness* parameter.
- **localRefinement**: this entry is usually set to target higher quality meshes specifying different refinement levels on different boundaries. The entry requires the name of the boundary on which the refinement must be applied. The

cell sizing can be either specified in dimensional values (meters) or as the number of relative levels starting from the *maxCellSize*. In this case, the number of desired subdivisions must be entered through the *additionalRefinementLevel* keyword. As for the *boundaryCellSize* option, a dimensional refinement thickness can be specified to preserve the mesh sizing along an offset distance from the boundary.

- **objectRefinement**: regions inside the volume mesh can be refined by defining the topology of some primitive geometries where some refinement level is desired. The *objectRefinement* entry contains a dictionary to declare the volume region to be refined: supported objects are lines, spheres, cylinders, cones, truncated cones, cylindrical annulus, conical annulus. For an in-depth description on how to set these primitives the reader may refer to the CFMesh user guide [55]. Refinement thickness is supported.

- **surfaceMeshRefinement**: this option allows for using of a surface geometry file (e.g., .stl or .fms format) to define customized refinement regions in the volume mesh. It can be interpreted as an upgrade of the previous *objectRefinement* entry which limits the refinement influence to primitive shapes. On the other hand, the *surfaceMeshRefinement* option extends the refinement influence to whatever topological region, as zones to be refined are wrapped by the geometry provided by the file through an ad-hoc *surfaceFile* keyword. Refinement thickness is supported as already seen for the *objectRefinement* entry.

- **edgeMeshRefinement**: similarly to the previous entry, this option enables the mesh refinement along edges of the domain. The feature edges can be extracted from the original geometry and saved in a Visualization Toolkit (.vtk) file running the *FMSToSurface -exportFeatureEdges* command of the CFMesh library. Thus, this file can be entered into the *edgeMesh* keyword of the *edgeMeshRefinement* entry, specifying a proper mesh sizing and refinement thickness. Once more, it is important that feature edges are well outlined in the original geometry file to produce a high quality linear refinement.

- **anisotropicSources**: this entry is useful for those cases when anisotropic meshes are required to produce accurate results, still reducing the total number of elements in the mesh. As for the *objectRefinement* entry, regions where anisotropic elements must be fit are detected through the specification of primitive objects. However, in this case only planes and boxes are supported for 2-D and 3-D refinements respectively.

- **boundaryLayers**: this entry manages the inflation of prismatic layers on wall boundaries. The names of these boundaries are entered as sub-dictionaries of the *patchBoundaryLayers* sub-dictionary. On each patch, the number of prismatic layers, the growth rate and the maximum thickness of the first cell are set through the keywords *nLayers*, *thicknessRatio*, *maxFirstLayerThickness*. A further *allowDiscontinuity* keyword can be turned on to prevent the spreading of the number of layers of a patch to an adjacent one. Optimisation parameters can be also enabled to activate smoothing algorithms for a higher quality layer extrusion. A thorough discussion about this aspect is addressed in [55].

3.3 The libAcoustics library

The *libAcoustics* [67] is an OpenFOAM compatible library for far field noise computation implementing three possible prediction models: the Curle analogy [52], the FWH analogy [68, 69] and the CFD-BEM (Blade Element Momentum) coupling. The validation of the library for acoustic post-processing can be found in [70].

Once compiled the correct distribution of the library, this can be enabled by including into the *controlDict* file two additional files named *commonSettings* and *fwhControl* that must be placed into the *system* directory. The output of the library calculation are the far field noise spectra, obtained from one of the prediction models combined with the Fast Fourier Transform (FFT) [71] of noise signal at some observer locations specified by the user. In this work, the *libAcoustics* has been used for the nozzle activity of Chapter 5. The FWH analogy based on the Farassat formulation [68] has been chosen to produce the desired results. A summary of the content of the *commonSettings* and the *fwhControl* files is reported below.

- **commonSettings**: in this file the call to the acoustic library is made through the *libs* keyword at the top. Then, the ambient properties are set specifying the undisturbed pressure, density and speed of sound of the fluid medium. The total time of acoustic probing is adjusted through the *timeStart* and *timeEnd* keywords while the sampling rate relative to the simulation time-step is expressed by the *probeFrequency* keyword. Finally, the virtual location of far field microphones is entered through the *observers* dictionary where the information on the FFT window width is provided by the *fftFreq* keyword. The latter multiplied by the *probeFrequency* and the dimensional time-step returns the window width in seconds.

- **fwhControl**: in this file, the selected prediction model and its formulation (in case of the FWH analogy) are declared. Hence, the control surface for far noise extrapolation is provided through the *surfaces* dictionary. Both boundary patches and external triangulated surface enclosing the noise sources are accepted here. In case of customized triangulated surface, this must be provided as a .stl file to be included into the *constant* directory. A wide documentation on how to choose the FWH control surface can be found in the work of Mendez et al. [72]. Further keywords can be set to specify a relative motion between the noise sources and the integration surface. Lastly, the transient due to the distance the acoustic waves have to travel to reach the microphones can be cut off by turning true the *fixedResponseDelay* keyword. The latter reads the time value set by the following *responseDelay* keyword to perform a translation of the time signal. Setting to zero the *responseDelay* means the generation of acoustic data from the prediction method and the simulation progress are simultaneous.

The output of the *libAcoustics* are far field noise spectra files at each microphone position, collected into the automatically created *acousticData* directory. All the spectra are initially produced from the signal time history after the time interval expressed by the *fftFreq* keyword of the *commonSettings* file. Then, the files content is updated and overwritten with new spectra after another *fftFreq* time interval has been elapsed. This means that the far field computation is continuously updated until the *timeEnd* limit is reached. In other words, the FFT is taken on the time varying signal with a window width that is enlarged as the simulation progresses. The time history of the noise signal is saved in a separate file which is progressively updated appending samples according to the *probeFrequency* value. The product between the *probeFrequency* and time-step values set the higher frequency that can be detected in the noise spectrum. More in detail this product is related to the sampling rate of the signal acquisition and thus to the temporal filtering of data. On the other hand, the lower frequency of the spectrum is calculated as the inverse of the window width at the end of the simulation. Taking into account aliasing effects, this means that long-lasting simulations have to be run if one is interested in accurately describing the low-frequency range of the noise spectrum. General guidance is to take almost 8-12 time samples to consider a certain spectral frequency unaffected by aliasing. This indirectly implies a slower convergence of the noise spectrum at the lower frequencies and a faster one at the highest.

4

Fan noise

In this chapter the acoustic liner investigation conducted in this work of thesis is presented. The first two sections inform the reader about the acoustic liners working principle and the state of the art of acoustic liners investigation approaches. Then, in the rest of the chapter, a detailed discussion on the simulations outcomes is provided.

4.1 Acoustic liners

Acoustic liners are perforated panels installed on intake ducts and sometimes on exhaust nozzles to absorb tone noise radiated from the aft and the rear part of the engine. Traditional liners are assembled putting a honeycomb panel in between a rigid support back-plate and a perforated face-sheet as depicted in Figure 4.1. The absorption mechanism of these passive devices is based on the Helmholtz resonance phenomenon. From a qualitative point of view, acoustic liners attenuate acoustic emissions in a narrow-band frequency range by dissipating acoustic energy into shear

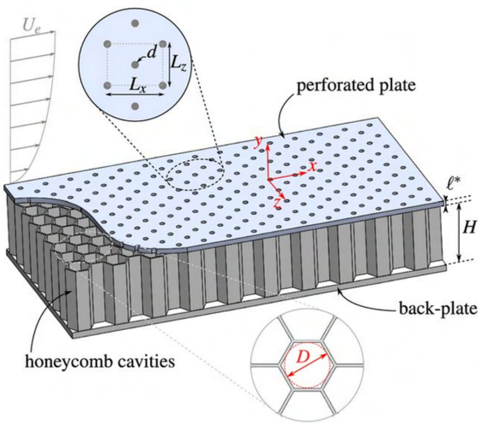

Figure 4.1: Acoustic liner geometrical parameters.

stresses and turbulent eddies at the orifices of perforated face-sheets. The attenuation effect is due to oscillations of cross-flow jets that set across the perforation pattern under the external acoustic forcing. To maximize the acoustic damping, the depth of the cavity backing the perforated plate is designed so that the resonant frequency of the Helmholtz resonator is tuned with the frequency of the acoustic excitation to be suppressed. In this way, augmented oscillations of the cross-flow jets are promoted converting a greater amount of acoustic energy into kinetic energy which is then dissipated by viscous friction. One of the major drawback of traditional liners is that acoustic attenuation is effective just around the resonant frequency of the system, thus leading to a very narrow operative range.

Moving now to technical considerations, in Figure 4.2 a 3D view and a sketch of an annular liner section is shown. The entire liner can be viewed as a series of adjacent Helmholtz resonators

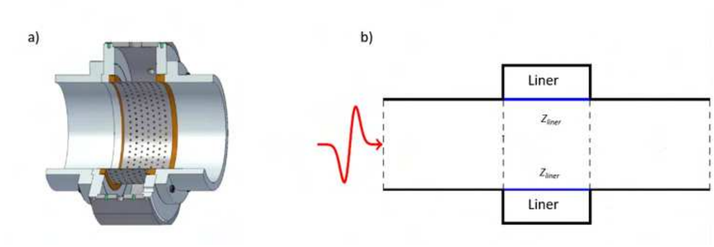

Figure 4.2: Annular liner section: 3D view (a) and schematic view (b).

all characterized by an its own acoustic impedance defined as:

$$Z = R + iX \tag{4.1}$$

From Equation 4.1 acoustic impedance is a complex quantity that measures the permeability of the resonator branch under the passage of a travelling acoustic wave (red arrow in Figure 4.2). Hence, acoustic impedance can be indirectly related to the acoustic absorption capability of the liner. More precisely, the acoustic impedance is made of a real part called resistance (R) and an imaginary part called reactance (X). The first one is concerned with the magnitude of the amplitude attenuation an acoustic wave undergoes when it hits the liner surface, while the second one sets the compliance of the perforated panel, and thus the acoustic response of the liner. Both the terms are functions of the resonator geometry and the excitation frequency so that different liners behaviours and absorption levels are possible depending on the external forcing and the liner dimensions. In case of Helmholtz resonance, the acoustic impedance is minimized and a maximum for the acoustic energy feeding the resonator cavity is found. The value of this maximum is a function on the resonator geometric parameters like the cavity depth, the orifice diameter and the face-sheet porosity and thickness. Since acoustic resistance cannot be negative as linked to damping effects, it follows that acoustic impedance is minimized (i.e., resonance occurrence) only when reactance vanishes. At the same time, resistance peaks as a consequence of the magnification of the viscous damping. On the other hand, far from resonance the sharp growth of reactance determines a hard-wall behaviour of the liner and the travelling wave just bypasses the resonator without being attenuated. Therefore, following a mechanical analogy [73], each single Helmholtz resonator of the liner assembly can be sketched as a lumped Single-Degree of Freedom (SDOF) mass-spring-damper, characterized by a single resonant frequency. This approximation holds as long as a locally reacting behaviour of the liner can be assumed, meaning that the acoustic wavelength of the excitation is much larger than the resonator dimensions. However, SDOF configurations of the liner can at most determine one single resonant frequency, thus motivating the narrow-band noise absorption typical of traditional panels. A possible strategy to broaden the absorption capability of acoustic liners is to build Multi-Degree of Freedom (MDOF) panels using multiple honeycomb layers interconnected by porous metallic septa. This stratified assembly is then enclosed by a rigid backplate and a perforated face-sheet as for traditional SDOF liners. The number of honeycombs that constitute the panel sets the number of degrees of freedom of the MDOF liner. Doing so, the designer makes the liner resonate at more than a single frequency (i.e., number of resonances equal to the number of degrees of freedom) and a multi-frequency attenuation can be obtained. However, the multi-cavity structure intrinsically determines anti-resonant frequencies in between of two adjacent resonances. Thus, when the acoustic forcing is tuned with one of the N-1 anti-resonant frequency of the MDOF liner, a hard-wall-like behavior of the panel is expected and no acoustic attenuation occurs. Therefore, the designer should carefully dimension the liner resonators ensuring that those frequencies to be suppressed will never match one of the anti-resonant frequencies of the system.

4.2 Acoustic impedance evaluation

As mentioned above, from an engineering point of view, the noise attenuation achieved with acoustic liners can be derived from the acoustic impedance of the perforated panel. The most common and practical way to measure acoustic impedance of SDOF liners is based on the use of one experimental two-microphones technique as described by Dean [74]. This is an extension of the impedance tube of Kundt [75] to account also for grazing flow and grazing incidence of the incoming excitation. At the same time, a large variety of semi-empirical and analytical theories have been developed to model the damping effect of SDOF acoustic liners. The first analytical models have been focused on the characterization of the acoustic impedance of Helmholtz resonators under the hypotheses of low pressure amplitudes and normal wave-front incidence. In this case, a single cell of an acoustic liner may be replaced by an equivalent SDOF mass-spring-damper system as proposed by Sivian [76]. To include the non-linearity of the flow oscillations and the radiation effect at the orifice neck, a more accurate impedance model has been suggested by Ingard [77]. Later on, semi-empirical models have been extended to consider the effects of a grazing flow on the acoustic performances of the acoustic liner cells. Basically, the grazing flow can be modeled as an obstacle for acoustic energy feeding the resonator neck. Under this hypothesis, the first semi-empirical model have been suggested by Garrison et al. [78] and Rice [79]. Further analyses have been conducted by Bauer [80] to model the mutual interaction of orifices in multi-perforated cell layouts. Then, Kooi and Sarin [81] have demonstrated that acoustic impedance is also a function of the boundary layer velocity profile. This point has been further deepened by Goldman and Chung [82] who have found a correlation between acoustic impedance of perforated plates and friction velocity at wall. Finally, Kirby and Cummings [83] have proposed some corrections to the existing models to consider the presence of porous materials on the resonator back-wall. With regard to MDOF layouts, an extension of the method of Dean [74] has been developed by Zandbergen [84] and Rademaker [85] for Double-Degree of Freedom (DDOF) and Triple-Degree of Freedom (TDOF) configurations respectively. But due to the challenging instrumentation of MDOF resonators, experimental campaigns usually rely on non-intrusive acquisitions of the acoustic field through Particle Image Velocimetry (PIV) or Laser Doppler Velocimetry (LDV) [86]. On the other hand, very few semi-analytical models are available from literature for MDOF liners. One of the most accurate is the model of Hersh et al., that has been introduced for SDOF systems [87] and then extended to DDOF geometries [88]. Another analytical model for DDOF liners is provided from the work of Mekid and Farooqui [89] where the authors show the link between the geometry of the DDOF resonator and the transmission loss parameter. More recent investigations on DDOF layout can be found in the work from Rego et al. [90]. However, despite the more and more accurate theoretical models and experimental measurements techniques, none of these approaches can provide a deeper insight on the physical phenomena that lead to the noise abatement of a liner element. To fill this gap, high-fidelity CFD simulations are becoming a viable alternative although only few works on this topic are already available from literature. A detailed literature review on the acoustic liner modeling strategies (analytical, mid-fidelity and high-fidelity) can be found in the work of Winkler et al. [91] where past practices and future needs are clearly described highlighting the pros. and cons. of the available methodologies. Some of the recent works are based on computational aeroacoustics (CAA) methods [92, 93], Lattice Boltzmann Method (LBM) [94, 95, 96] and Large Eddy Simulations (LES) [97]. Among them, high-fidelity numerical investigations for impedance eduction of a single-element SDOF liner have been carried out by Bodony and Zhang [98]. Through a Direct Numerical Simulation (DNS) approach, they investigated the acoustic response of both a single- and multi-orifice perforated plates backed by a hexagonal cavity under no grazing flow and normal incidence of an incoming tonal excitation. The authors further extended their investigation to the single-orifice SDOF liner in presence of a grazing flow [99] generating a wide DNS database used in this work for validation purposes. A LES approach has been also used by Bauerheim and Joly [100] to investigate the liner aeroacoustic coupling under grazing flow conditions, and by Esnault et al. [101] to study synthetic jets in combustor liners. With the aim of extending the knowledge about the physics involved in the noise reduction mechanisms of SDOF acoustic liners, in the first part of the present chapter a LES approach has been exploited to evaluate the acoustic impedance of a single- and multi-orifice liner elements for acoustic grazing waves both in absence and presence of a grazing flow. The geometry of the multi-orifice liner elements is the one experimentally studied by Jones in [102]. This part of the work is focused on the evaluation of the acoustic abatement of these liner elements in a wide range of acoustic wave amplitudes and frequencies, combined with the effect of a realistic grazing flow Mach number at the fan inlet (e.g, M = 0.3, M = 0.5). Then, single-orifice results have been presented as an additional SDOF test-case to explore a porosity scaling of the impedance results. Hence, the validation of the LES setup has been achieved by comparing the acoustic performance of multi-orifice cells with a porosity close to the Jones' test case against experimental and analytical predictions. To this purpose, the semi-analytical model of Hersh et al. [87] has been used. Furthermore, special attention has been paid to discuss the complex aerodynamic flow structures at the orifice neck strictly linked to noise attenuation. In the second part of the work, the presented LES approach has been used to validate an in-house recursive extension of MDOF liner derived by the guidelines provided in [88] and already presented in [103]. This analytical model results a quick tool for the design MDOF liners. Finally, as a side objective of this activity on acoustic liners it has been demonstrated that high-fidelity approaches are becoming a viable alternative also for liner design, contrasting the historical inertia of using empirical-based tools. This is particularly true for innovative liner concepts (e.g. triply periodic minimal surfaces, TPMS [91]) that might be needed to achieve a lower and broader noise attenuation with more compact configurations. The present study is part of a broad research activity on aircraft engine noise which includes previous studies on both tonal [104, 105] and core noise [106, 107, 108, 109, 110] of aeronautical turbine modules. To demonstrate the capability of the LES approach in predicting the acoustic performance of different liner typologies, three liner arrangements are analysed.

4.3 Test-cases

In the following pages, the three liner arrangements investigated in this work are presented. A multi-orifice SDOF case has been used to validate the CFD method, a single-orifice SDOF case to assess the scalability of impedance results and a single-orifice MDOF case to test the attenuation performance of an innovative liner layout.

4.3.1 Multi-orifice SDOF configuration

The liner geometry selected for the LES validation phase, was the one experimentally studied by Jones et al. at the NASA Langley Research [102] in the test rig named Grazing Flow Incidence Tube (GFIT) shown in Figure 4.3.

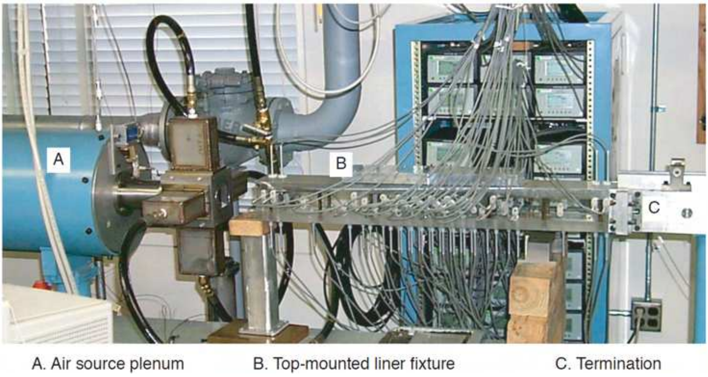

Figure 4.3: Photograph of GFIT from [102].

Experimental campaigns for impedance eduction of aeronautical liners with and without grazing flow have been carried out by the NASA Langley Research Center Liner Physics Group for a long time [111]. This experimental research activity made available to the aeroacoustic community a large database of high quality impedance data for different panel configurations extremely useful to validate analytical impedance models and, more recently, high-fidelity (LES, DNS, LBM) computation setups. The original GFIT test rig, was continuously improved by implementing different acquisition systems based on traversing bar (GFIT-TB) and 95 fixed-located microphones (GFIT-95M). For sake of clarity, a schematic drawing of the test section with these two different acquisition systems is reported in Figure 4.4. All the details about the test rig, the impedance test section and the acquisition system can be found in [102]. From pressure signals acquired with microphones, the liner impedance is educed with both an analytical approach and a 2D finite element method. Different types of acoustic liners, ceramic tubular and two conventional perforated configurations with different porosity, were experimentally studied in [102].

The presented numerical investigation was focused on conventional perforated configuration #1 (low porosity) reported in [102] that is representative of those currently installed inside on commercial aircraft engines for noise suppression. The conventional perforated liner configuration #1 consists of an aluminum face-sheet bonded onto 9.5 mm-diameter hex-cell honeycomb cavities that are 38.1 mm deep. The face-sheet thickness is 0.64 mm, the hole diameter equal to 0.99 mm, and the hole density was selected to achieve a porosity $\sigma = 6.4\%$ as shown in Figure 4.5(a). To numerically investigate this configuration with a repetitive pattern, a seven-orifice pattern for each honeycomb cavity configuration was built (see Figure 4.5(b)). The diameter of the orifices and hexagon dimensions were kept the same leading to a porosity $\sigma = 6.93\%$, very close to the experimental value. The geometry and the fluid mesh were built in the open-source SALOME framework [56], then they were converted into

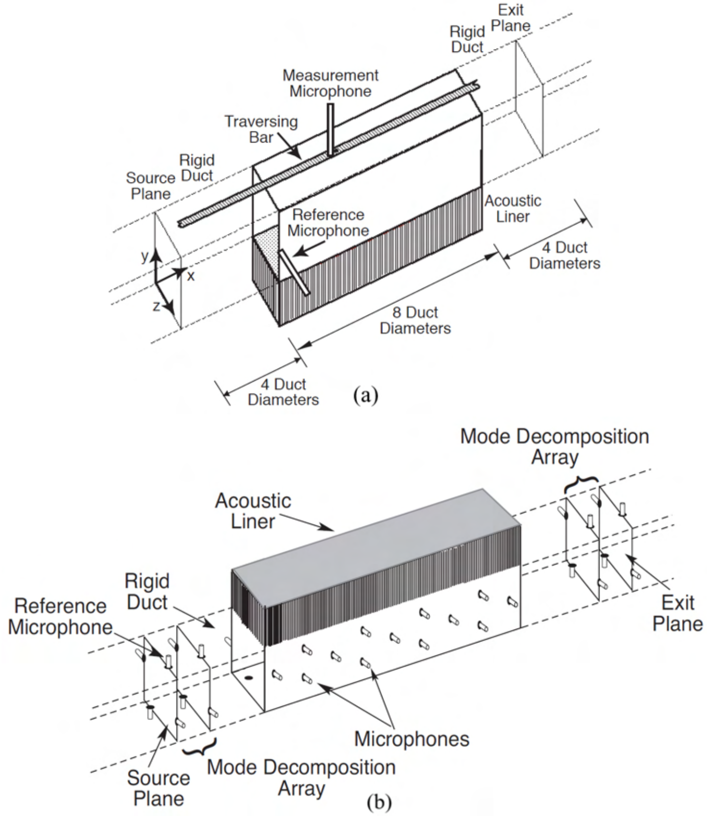

Figure 4.4: GFIT test section with different acquisition systems from [102]: (a) traversing bar GFIT-TB, (b) microphone array GFIT-95M.

an OpenFOAM [54] readable format to run the LES. A structured grid strategy was followed to discretize the entire domain. This latter was made of the hexagonal resonator and an upper box where planar acoustic waves were enforced to travel streamwise. To prevent any interaction between the cross-flow jets and the far-field, the upper box was sized to span a length of 240 ori-

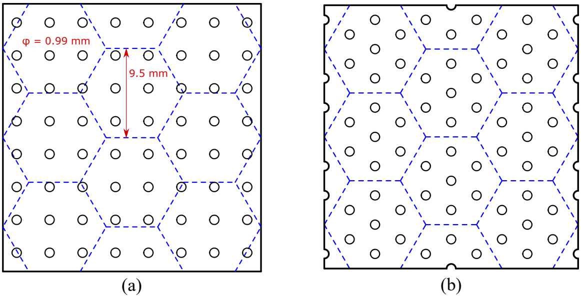

(a) (b)

Figure 4.5: Schematic of perforated patterns: (a) conventional liner #1 tested in [102] and (b) the seven-orifices configuration.

fice diameters in the stream-wise direction (L_x), a height of 100 orifice diameters in the wall-normal direction (L_y) and a width of 80 diameters in the span-wise direction (L_z). An illustration of the numerical domain geometry and its boundaries is reported in Figure 4.6. With regard to the meshing procedure, local grid refinements were needed close to the orifices where complex flow structures are generated by the pulsating jets, especially at the non-linear regimes (e.g. high SPLs or close to resonance). Moving to the orifices region both from the upper domain box and the cavity, the mesh elements were kept as uniform as possible to increase the numerical stability of the simulations. Namely, it is well known that a steep variation in the elements size or a bad mesh quality in the region of interest might result in a less robust setup. Moreover, the mesh was intentionally coarsened in the far field regions to reduce the computational cost of the simulations. In this way, a proper mesh density around the orifices was achieved, still reducing the total number of elements of the final mesh. To accurately predict the flow oscillations across the orifices and the wall shear stresses, each orifice was discretized by

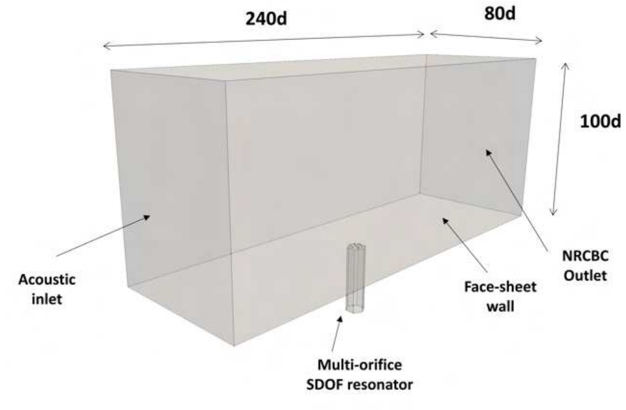

Figure 4.6: SDOF numerical domain: boundaries and dimensions.

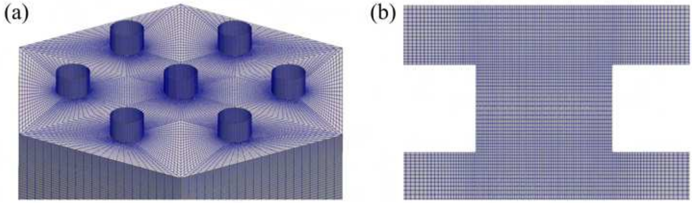

Figure 4.7: Mesh details: (a) orifice-region mesh and (b) single-orifice mesh.

45 grid points along the diameter. An outward radial refinement was used to stretch the cells down to the orifice lateral surface, resulting in a first off-the-wall cell height of about 0.013 mm. In addition, wall-normal and span-wise mesh refinements were enforced on the upper box to correctly match the coarse mesh in the far-field with the fine one near the orifices. Details of the mesh close to the orifices are visible in Figure 4.7.

4.3.2 Single-orifice SDOF configuration

A single-orifice configuration ($\sigma = 0.99\%$) depicted in Figure 4.8 was also studied to discuss the applicability of a porosity scaling of the impedance results. Namely, the cavity shape of the multi-orifice resonator was preserved but just the central orifice of the pattern was retained. The analyses on this simplified resonator help understanding whether liners with different porosity could be correlated from an acoustical point of view.

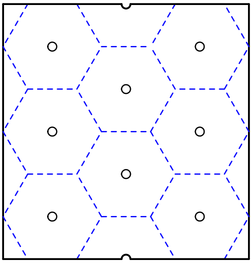

Figure 4.8: Single-orifice configuration.

4.3.3 Single-orifice MDOF configuration

This single-orifice MDOF configuration was studied to further validate the MDOF semi-analytical model proposed in [103] under realistic grazing conditions. This can be achieved by leveraging the experimental multi-microphone technique of Rademaker [85] for the impedance eduction. To do so, virtual microphones were implemented in the numerical environment of the LES. To ease the generation of the fluid domain and mesh, three identical squared-cross-section cavities and two identical septum thicknesses were considered to build a triple degree of freedom (TDOF) liner unit. For the same reason, a single-orifice

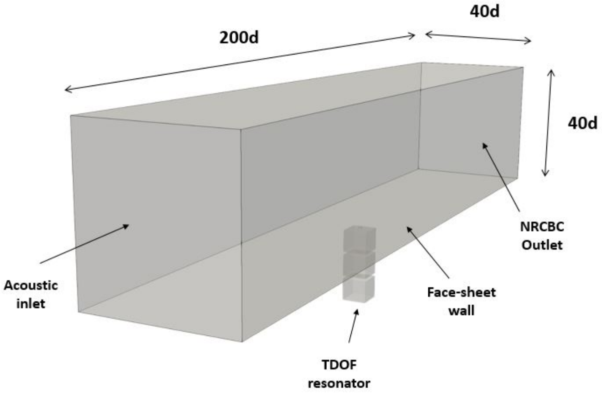

Figure 4.9: TDOF numerical domain: boundaries and dimensions.

coaxial pattern was considered. The choice of a TDOF arrangement comes from the restricted applicability of the Rademaker impedance measurement technique [85] to TDOF liners only. However, it can be reasonably assumed that for innovative MDOF liners, three degrees of freedom are a proper trade-off between absorption range widening and manufacturing complexity. Moreover, larger MDOF systems are necessarily heavier and more cumbersome, leading to installation issues inside the engine nacelle.

As for the previous test-cases, an upper box was generated to enforce a grazing planar excitation. Details of the numerical domain are shown in Figure 4.9 and Table 4.1. Focusing on the meshing strategy, the structured mesh was refined across the orifice regions where the pulsating jets are expected. The mesh density in these regions was calibrated to target an accurate discretization of the wall shear stresses at the orifice surface under the resonant condition. As for the SDOF cases, similar consid-

Orifice diameter (d)	1.20 mm
Facesheet/septum thickness (w)	1.00 mm
Cavity depth (L)	7.83 mm
Cavity side (l)	8.62 mm
Porosity (σ)	1.52%
Bounding box length (Lx)	200 d
Bounding box height (Ly)	40 d
Bounding box width (Lz)	40 d

Table 4.1: Dimensions of numerical domain.

erations can be made on the meshing strategy of the different zones of the domain. It is worth noting that the wall-normal refinement is needed to correctly solve the boundary layer in case of grazing flow simulations. The main meshing parameters are listed in Table 4.2 while details of the mesh refinements on a meridional slice are visible in Figure 4.10. The reader may note that the clustering strategy used at the upper orifice was repeated also on the middle and the lower cavity. More precisely, along the vertical edges of each cavity of the resonator, a tooth-saw distribution of mesh points was used. This latter enabled the mesh coarsening at the middle of the cavity still refining it when approaching to the orifices.

4.4 Semi-analytical impedance model

The first part of this section gives an overview of the original Hersh model formulation for SDOF multi-orifice liners [87]. Then, an in-house recursive extension of the model to MDOF liners is described. Such extension was already validated for a

Total number of elements	8.5M
Mesh points per diameter	45
Min. mesh points per wavelength	40
Bounding box first cell height [mm]	0.023
Max. average y^+	0.93
Max. aspect ratio	66
Max. non-orthogonality	42°

Table 4.2: Meshing parameters of the TDOF test-case.

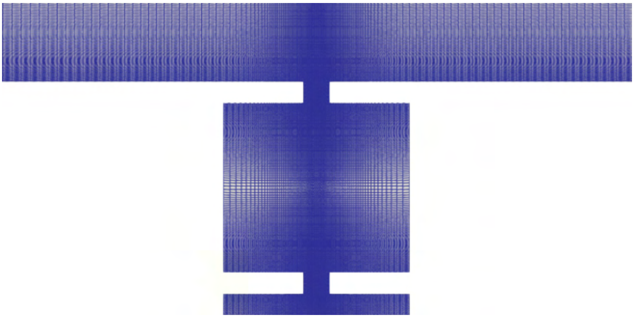

Figure 4.10: Mesh refinement on the TDOF meridional view.

single-orifice, multi-cavity resonator in [103], so it is used hereafter to demonstrate its validity also for a multi-orifice single-cavity configurations.

With reference to Figure 4.11, each degree of freedom of whatever cell arrangement can be characterized by an its own acoustic impedance. This latter is derived by taking the ratio between acoustic pressure P_0 and velocity u_0 at the orifices aperture. To do so, the conservation of unsteady mass and vertical momentum must be solved on control volumes as the ones highlighted with the dashed line in Figure 4.11. Considering just the upper control volume, this spans a height equal to an

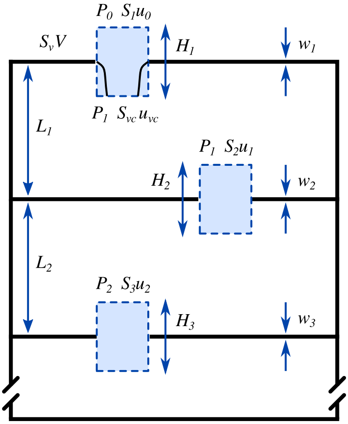

Figure 4.11: Sketch of control volumes used in the Hersh model. Multi-orifice configurations can be dealt by using an equivalent single-orifice diameter.

unknown inertial length H_1 of the jet oscillations. The upper control surface has an opening area equal to the orifices aperture S_1, while the lower one is reduced due to the acoustic blockage on the orifices wall leading to an effective area S_{vc}. The perforation pattern is supposed to be made of orifices with the same diameter, each one with a wall surface area $S_w = \pi dw$. Similar considerations hold also for the remaining degrees of freedom of the generic MDOF liner cell. In the following, the workflow to derive the impedance model for a SDOF multi-orifice cell pattern is fully discussed.

4.4.1 SDOF impedance model

When an acoustic wave hits the perforated plate, some acoustic volume flow enters the resonator through the orifices aperture. In case of N orifices and focusing on the inward half-cycle, from the unsteady mass and vertical momentum conservation laws it yields:

$$u_{vc}NS_{vc} = u_0NS_1 + VNS_V \tag{4.2}$$

$$\rho_0HNS_1\frac{du_{vc}}{dt} + \rho_0N(u_{vc}^2S_{vc} - u_0^2S_1) = (P_0 - P_1)NS_1 - \tau_wNS_w \tag{4.3}$$

where:

- $u_{vc}NS_{vc}$ is the overall acoustic volume flow exiting the lower control surface
- u_0NS_1 is the overall acoustic volume flow entering the upper control surface
- VNS_V is the overall grazing volume flow deflected into the N orifices
- $\rho_0HNS_1\frac{du_{vc}}{dt}$ is the rate of increase in vertical momentum
- $\rho_0N(u_{vc}^2S_{vc} - u_0^2S_1)$ is the momentum flux across the control surfaces
- $(P_0 - P_1)NS_1$ is the net driving pressure force at the N orifices
- τ_wNS_w is the viscous loss due to shear on the wall of the N orifices

At this point five hypotheses, reported in the following sections, are made to derive analytical models for acoustic resistance and reactance.

1. **Discharge coefficients**

   To evaluate the acoustic blockage on each orifice wall and the amount of grazing flow deflected into the resonator, an acoustic and a grazing flow discharge coefficients are introduced

$$C_D = \frac{S_{vc}}{S_1}, \quad C_V = \frac{S_V}{S_1} \tag{4.4}$$

By substituting Equations 4.2 and 4.4 into Equation 4.3, the momentum equation is recast as:

$$\rho_0 HNS_1 \frac{du_{vc}}{dt} + \rho_0 NS_1 [C_D(1 - C_D)u_{vc}^2 + 2VC_D C_V u_{vc}] = \\ = (P_0 - P_1)NS_1 - \tau_w NS_w \tag{4.5}$$

From Equation 4.5 it can be observed that a linearized version of the momentum equation is obtained when the acoustic discharge coefficient tends to unity. This approximation holds far from resonance or at the very low SPLs, when almost no jet oscillations set across the orifices.

2. **Cavity pressure**

   The restoring cavity pressure P_1 can be expressed as:

   $$P_1 = -i\rho_0 c_0 \sigma_1 \cot\left(\frac{\omega}{c_0} L_1\right) u_{vc}, \quad \sigma_1 = \frac{NS_1}{S_{cav}} \tag{4.6}$$

   Equation 4.6 is derived by solving the 1-D wave equation along the cavity depth (L_1) direction. In Equation 4.6, the liner porosity σ_1 is given by the ratio between the perforated area and the area of the cavity cross section S_{cav}.

3. **Non-linearity**

   When the acoustic system undergoes a non-linear regime (e.g., resonance or very high SPLs), the non-linear term in Equation 4.5 is supposed to oscillate harmonically. Moreover, it can be assumed that the link between the acoustic forcing P_0 and velocity u_{vc} is given by an unknown phase shift θ_p which vanishes at resonance. These approximations are respectively expressed by Equations 4.7 and 4.8.

$$(u_{vc}e^{i\omega t})^2 = (u_{vc}^2)e^{i\omega t} \tag{4.7}$$

$$u_{vc}(t) = u_{vc}e^{(i\omega t+\theta_p)} \tag{4.8}$$

4. **Viscous losses**

The momentum loss due to viscous shear stresses on the wall of each orifice is modelled by Equation 4.9

$$\tau_w = \left(k_s + k_a\sqrt{\frac{\omega {d_1}^2}{\nu_0}}\right)\frac{\mu_0}{d_1}C_D u_{vc} \tag{4.9}$$

where d_1 is the orifice diameter, ν_0 and μ_0 are the kinematic and dynamic viscosity of air and k_s and k_a are empirical constants which depend on the diameter-to-thickness ratio of the liner cell. Equation 4.9 highlights that the overall viscous shear is given by the sum of steady-state and pulsating contributions. The first one is due to the boundary layer thickness on the orifice wall whereas the second one is related to the excitation pulsation. In case of a multi-orifice layout, Equation 4.9 still holds if an equivalent single-orifice perforation is assumed. More precisely, the orifice equivalent diameter to be considered when calculating the viscous losses is:

$$d_{eq} = \sqrt{N}d_1 \tag{4.10}$$

Equation 4.10 is obtained by imposing that the equivalent single orifice has the same opening area of the original multi-orifice perforation.

5. **Resistance-reactance decoupling**

   By substituting Equations 4.6 to 4.10 into Equation 4.5, the following expression is derived:

$$C_D(1-C_D)u_{vc}^2 + \left[2VC_V + \frac{4\nu_0 w_1}{d_1^2}\left(k_s + k_a\sqrt{\frac{\omega {d_1}^2}{\nu_0}}\right)\right] C_D u_{vc} + i\left[\omega H - c_0\sigma_1 \cot\left(\frac{\omega L_1}{c_0}\right)\right] u_{vc} = \frac{P_0}{\rho_0} \tag{4.11}$$

   The resistance-reactance decoupling hypothesis is required to separately equate the real and the imaginary parts on the LHS of Equation 4.11 to the RHS. Without this simplification, Equation 4.11 would admit no analytical solution due to its complex formulation. Taking separate ratios between the acoustic forcing P_0 and the acoustic velocity u_{vc} leads to the following models for acoustic resistance and reactance:

$$\frac{R}{\rho_0 c_0} = \sqrt{\left(\frac{1-C_D}{C_D}\right)\left(\frac{P_0}{\rho_0 c_0^2 \sigma_1^2}\right) + \left(\frac{VC_V}{2\sigma_1 c_0} + \frac{R_L}{2\rho_0 c_0}\right)^2} + \left(\frac{VC_V}{2\sigma_1 c_0} + \frac{R_L}{2\rho_0 c_0}\right) \tag{4.12}$$

$$\frac{X}{\rho_0 c_0} = \frac{\omega H}{\sigma_1 c_0} - \cot\left(\frac{\omega L_1}{c_0}\right) \tag{4.13}$$

Equation 4.12 can be interpreted as a solution to Equation 4.11 in case of a system resonance. Under this condition, the imaginary part of Equation 4.11 vanishes and a solution to u_{vc} may be found by solving a second order algebraic equation. The extension of the resistance model to frequencies far from the resonant one is achieved by making the discharge coefficient a function of the excitation frequency. For each orifice of the perforation pattern, a unique discharge coefficient is calculated at resonance as a function of the thickness-to-diameter ratio only. Then, the frequency dependency is imposed through polynomial expressions to account for the linear or non-linear regime the system undergoes at different excitation frequencies and SPLs. It should be also noted that overall resistance includes the linear resistance term given by:

$$\frac{R_L}{\rho_0 c_0} = \frac{\nu_0 w_1}{\sigma_1 c_0 d_{eq}^2}\left(N k_s + k_a \sqrt{\frac{N \omega {d_{eq}}^2}{\nu_0}}\right) \tag{4.14}$$

Equation 4.14 is derived from Equation 4.12 under the linearization hypothesis and in absence of grazing flow (e.g., C_D = 1, V = 0). The linear resistance is the major contribute to the overall acoustic resistance in case of very low SPLs or when the excitation frequency is not tuned with the system resonant frequency. With regard to the reactance model, Equation 4.13 shows that a reactance trend can be obtained if some closure for the unknown inertial parameter H is provided. In case of linear behavior of the acoustic system and in absence of grazing flow, the inertial parameter is found to be a function of the resonator geometry only. Otherwise, some corrections should be applied to consider the effects of the SPL and the grazing speed on the effective length of the jet oscillations. The reader may refer to [87] for further details about this topic.

4.4.2 MDOF impedance model

The theory of the Hersh model [87] can be extended to whatever MDOF arrangement of the liner cells. This can be made by linking the impedances of each degree of freedom of the MDOF cell through a recursive formulation. In this section, the aim is to present an in-house implementation of the theory extension applied to TDOF single-orifice liner cell. This assumption does not restrict the validity of the recursive version to single-orifice configurations, as the equivalent orifice approximation still holds. However, some questions may arise on how non-linear effects are redistributed over each degree of freedom of the MDOF assembly. With reference to the sketch in Figure 4.11, the discharge coefficients are introduced for the upper control volume only. This simplification is straightforward for the grazing flow coefficient as just the upper degree of freedom is directly exposed to a grazing flow. On the other hand, the hypothesis of having the acoustic discharge coefficient on the upper degree of freedom only was made to reduce the complexity of the recursive formulation. Moreover, it is not well understood if the way the discharge coefficient is calculated for SDOF layouts holds even for the MDOF ones. For these reasons, it has been assumed that the effects of non-linear regimes would have been exerted on the upper resonator only, considering linear resistance and reactance models for the remaining ones. Although these simplifications might slightly alter the acoustic response of the MDOF cell, the extension procedure is supposed robust enough to provide at least a preliminary estimation of the noise attenuation achieved with MDOF liners. To derive acoustic impedance of the TDOF cell, the continuity and the vertical momentum equations apply to the three control volumes displayed in Figure 4.11. Following the same steps as for the SDOF case and considering the previous hypotheses, the three momentum equations can be rearranged in the form:

$$
\begin{aligned}
\rho_0 H_1 S_1 \frac{du_1}{dt} + \rho_0 S_1 \left[\left(\frac{1 - C_D}{C_D} \right) u_1^2 + 2 V C_V u_1 \right] = \\
= (P_0 - P_1) S_1 - \tau_{w1} S_{w1} \\
\rho_0 H_2 S_2 \frac{du_2}{dt} = (P_1 - P_2) S_2 - \tau_{w2} S_{w2} \\
\rho_0 H_3 S_3 \frac{du_3}{dt} = (P_2 - P_3) S_3 - \tau_{w3} S_{w3}
\end{aligned}
\tag{4.15}
$$

where the subscript $i = 1, 2, 3$ labels the acoustic velocities at the orifice of each degree of freedom. The restoring cavity pressure is again retrieved by solving the 1-D wave equation along the cavity depth direction. In this case, due to the presence of the septa of the TDOF assembly, the acoustic velocities u_2 and u_3 contribute to the overall restoring pressure at the upper and the middle orifices.

$$
\begin{aligned}
P_1 &= -i \rho_0 c_0 \sigma_1 \cot\left(\frac{\omega L_1}{c_0} \right) u_1 + i \frac{\rho_0 c_0 \sigma_2}{\sin\left(\frac{\omega L_1}{c_0} \right)} u_2 \\
P_2 &= -i \rho_0 c_0 \sigma_2 \cot\left(\frac{\omega L_2}{c_0} \right) u_2 + i \frac{\rho_0 c_0 \sigma_3}{\sin\left(\frac{\omega L_2}{c_0} \right)} u_3 \\
P_3 &= -i \rho_0 c_0 \sigma_3 \cot\left(\frac{\omega L_3}{c_0} \right) u_3
\end{aligned}
\tag{4.16}
$$

Finally, viscous losses at each degree of freedom are modeled by a generic gamma function:

$$\Gamma_i = \left(N_i K_{ssi} + K_{aci} \sqrt{\frac{\omega N_i {d_{eqi}}^2}{\nu_0}} \right) \frac{\nu_0 w_i}{d_{eqi}^2} \tag{4.17}$$

Inserting Equations 4.16 and 4.17 into System 4.15, the following expressions are derived:

$$\begin{aligned}
&\left(\frac{1-C_D}{C_D}\right) u_1^2 + [2VC_V + \Gamma_1 + i(\omega H_1 - c_0\sigma_1 \cot{(kL_1)})]u_1 + \\
&+ i\frac{c_0\sigma_2}{\sin{(kL_1)}}u_2 = \frac{P_0}{\rho_0} \\
&\left[\Gamma_2 + i\left(\omega H_2 - c_0\sigma_2 \cot{(kL_2)} - \frac{c_0\sigma_2}{\sin{(kL_1)}}\right)\right]u_2 + \\
&+ i\frac{c_0\sigma_3}{\sin{kL_2}}u_3 + ic_0\sigma_1 \cot{(kL_1)}u_1 = 0 \\
&\left[\Gamma_3 + i\left(\omega H_3 - c_0\sigma_3 \cot{(kL_3)} - \frac{c_0\sigma_3}{\sin{(kL_3)}}\right)\right]u_3 + \\
&+ ic_0\sigma_2 \cot{(kL_2)}u_2 = 0
\end{aligned} \tag{4.18}$$

For sake of clarity, in System 4.18 the wave number $k = \frac{\omega}{c_0}$ has been introduced. From the third equation of System 4.18, the acoustic velocity u_3 can be written as a function of u_2 and inserted into the second equation. Hence, in a recursive way u_2 is expressed as a function of u_1 and substituted into the first equation. At this point, after some mathematical passages, the first equation of System 4.18 simplifies to:

$$\left(\frac{1-C_D}{C_D}\right) u_1^2 + [2VC_V + z_1]u_1 = \frac{P_0}{\rho_0} \tag{4.19}$$

where z_1 is the acoustic impedance of the upper resonator. The recursive link between the impedance of each degree of freedom is provided by System 4.20:

$$\begin{aligned}
z_1 &= \Gamma_1 + \frac{c_0^2\sigma_1\sigma_2\cot(kL_1)}{z_2\sin(kL_1) - ic_0\sigma_2} + i(\omega H_1 - c_0\sigma_1\cot(kL_1)) \\
z_2 &= \Gamma_2 + \frac{c_0^2\sigma_2\sigma_3\cot(kL_2)}{z_3\sin(kL_2) - ic_0\sigma_3} + i(\omega H_2 - c_0\sigma_2\cot(kL_2)) \\
z_3 &= \Gamma_3 + i(\omega H_3 - c_0\sigma_3\cot(kL_3))
\end{aligned} \tag{4.20}$$

From System 4.20 it can be noted that the impedance of the lower resonator z_3 is exactly the same as if the liner cell had been composed just of it. On the contrary, the impedance of the middle and the upper resonators are affected by the presence of the other degrees of freedom of the assembly. This is well highlighted by the first and the second equations of the System 4.20. Generally speaking, it can be concluded that for MDOF cells, the impedance z_{i-1} is a function of the impedance z_i, stressing the recursive coupling between the degrees of freedom of the MDOF resonator. Finally, by solving Equation 4.19 for u_1 , the global impedance Z of the TDOF cell is derived taking the ratio between the acoustic forcing P_0 and the acoustic velocity u_1.

4.5 High-fidelity method

High-fidelity LES were performed for the three test cases using the open-source OpenFOAM (Open Field Operation And Manipulation) suite [54]. The simulations matrices are reported in Tables 4.3, 4.4, 4.5. Letters A, B and C stand for the simulations carried on the multi-orifice SDOF, single-orifice SDOF and single-orifice MDOF test-cases respectively. As listed in Table 4.3, the acoustic response of the multi-orifice SDOF resonator was investigated varying the excitation frequency (cases A1-A6), the SPL (cases A6-A9) and the grazing flow Mach number (cases

SDOF multi-orifice			
Case	Freq. [Hz]	SPL [dB]	Mach [-]
A1	500	130	0.000
A2	1000	130	0.000
A3	1500	130	0.000
A4	2000	130	0.000
A5	2500	130	0.000
A6	3000	130	0.000
A7	3000	140	0.000
A8	3000	150	0.000
A9	3000	160	0.000
A10	1500	130	0.300
A11	3000	130	0.500

Table 4.3: Simulation matrix for the SDOF multi-orifice tcase.

A10-A11). For the latter cases, a uniform laminar inflow was set on the upper box domain. This is an important aspect of the grazing flow simulations as the boundary layer characteristic (laminar or turbulent) has a strong influence on the resistance prediction, as it will be shown later on in the chapter. Look-

SDOF single-orifice			
Case	Freq. [Hz]	SPL [dB]	Mach [-]
B1	500	130	0.000
B2	1000	130	0.000
B3	1500	130	0.000
B4	2000	130	0.000
B5	2500	130	0.000
B6	3000	130	0.000

Table 4.4: Simulation matrix for the SDOF single-orifice case.

ing at Table 4.4, it can be seen that LES of the single-orifice SDOF test-case (cases B1-B6) were run varying the excitation frequency only and in absence of a grazing flow. This was established as it is presumed that the frequency response is the the most sensitive to a variation of the liner porosity. Moving to the MDOF arrangement, the eleven LES cases listed in Table 4.5 (cases C1-C11) were needed to accurately describe the MDOF frequency response. Then, four additional calculations (cases C12-C15) have been set up to understand how the grazing flow alters the resonator behavior at a frequency close to the first resonance (i.e., 750 Hz). Also for the MDOF, the hypothesis of a laminar inflow was used to reduce the complexity of the

MDOF single-orifice			
Case	Freq. [Hz]	SPL [dB]	Mach [-]
C1	500	130	0.000
C2	750	130	0.000
C3	1000	130	0.000
C4	1800	130	0.000
C5	2000	130	0.000
C6	2250	130	0.000
C7	2500	130	0.000
C8	3000	130	0.000
C9	3500	130	0.000
C10	5000	130	0.000
C11	6000	130	0.000
C12	750	130	0.075
C13	750	130	0.150
C14	750	130	0.225
C15	750	130	0.300

Table 4.5: Simulation matrix for the MDOF single-orifice case.

numerical setup and to easily allow the imposition of a grazing acoustic perturbation.

4.5.1 Boundary conditions

In all the simulations, a single-frequency planar acoustic wave was forced to travel along the grazing flow direction from the inlet to the outlet of the upper box domain. This is the main difference with respect to the analyses presented in [98] where the acoustic wave enters the domain from the domain top. No discrepancies in the acoustic results are expected, and in addition, a grazing acoustic wave is considered more representative of the liner working condition in turbofan engines. A sinusoidal variation of the inlet pressure, that generates the planar wave, was specified at the inlet plane through the *uniformFixedValue* boundary condition available in the OpenFOAM. This latter sets the amplitude and the frequency of the incoming acoustic wave together with the mean pressure on which the acoustic signal superimposes. A non-reflective characteristic boundary condition (NRCBC) is applied to the outlet boundary to prevent any spurious reflections. This ensured that the acoustic field close to the resonator neck was not altered by spurious boundary effects. To this purpose, the non-reflective *waveTransmissive* boundary condition was selected for all the flow variables transported by the wave equation (e.g. velocity, pressure and temperature). As explained by Poinsot and Lelef [112], such a Robin-type boundary condition solves the inviscid Navier-Stokes equations recast in the characteristics form on the outlet plane. The reflectivity of the outlet was adjusted by tuning a stiffness constant which acts as a source term in the in-homogeneous inviscid Navier-Stokes equations. The value of this constant is a measure of how far downstream of the outlet the mean pressure field is. According to the OpenFOAM nomenclature, the L_{inf} parameter was set to 20 to avoid backwards reflection of the excitation at the outlet. The standard *noSlip* condition was applied to the velocity field at the perforated plate, while the *cyclicAMI* constraint was used to enforce a span-wise periodicity of the flow variables on the upper box. Finally, a uniform temperature of 300 K was specified at the inlet through the Dirichlet-type $fixedValue$ boundary condition, while walls were treated as adiabatic through the Neumann-type *zeroGradient* boundary condition. A summary of the selected boundary conditions is shown in Table 4.6.

Patch	Pressure	Velocity	Temperature
Inlet	*Dirichlet*	*Neumann*	*Dirichlet*
Outlet	*NRCBC*	*NRCBC*	*NRCBC*
Top	*Neumann*	*Neumann*	*Neumann*
Lateral	*periodic*	*periodic*	*periodic*
Walls	*Neumann*	*no-slip*	*Neumann*

Table 4.6: Boundary conditions matrix used for all the cases.

4.5.2 Numerical solver and schemes

In the following, the numerical setup of the LES is described in detail focusing on those aspects that can play an important role when performing aeroacoustic simulations. The unsteady compressible pressure-based $rhoPimpleFoam$ solver was selected to run the LES. The solver implements the PIMPLE algorithm, which blends the Semi-Implicit Method for Pressure Linked Equations (SIMPLE) [65, 113] and the Pressure Implicit with Splitting Operator (PISO) [66] algorithms to enhance the stability of the unsteady calculations. After a sensitivity analysis, it was found that two loops on pressure equation (PISO algorithm) and three pressure-velocity coupling loops (SIMPLE algorithm) were a reasonable trade-off between stability and convergence acceleration requirements. For temporal discretization of the Navier-Stokes equations, an implicit second order *backward* scheme was selected. The gradient, the convective, and the diffusive terms were discretized with a blended *Gauss localBlended* scheme. This latter was set to switch between a fourth order cell-centered *Gauss cubic* scheme close to the orifices and the face-sheet and a first order upwind *Gauss upwind* scheme. This choice was motivated by the need for having high accuracy where pulsating jets and the grazing boundary layer are expected, while improving the setup stability otherwise. Finally, the WALE subgrid model [45] was selected to close the system of Navier-Stokes equations. All the simulations were run until reaching the convergence of acoustic pressure inside the resonator on 160 CPU cores of a Linux cluster equipped with Intel CPU E5-2680 at 2.8 GHz, taking from 24 to 96 hours to complete the parallel run. The statistical convergence of the solution was monitored by recording the pressure signal at the cavity back-wall for the SDOF layouts and at the back-wall of the lower cavity for the MDOF one. More precisely, the duration of the acoustic transient was defined as the time the acoustic oscillations inside the resonator need to grow to constant amplitude. Depending on the characteristic of the excitation, this time ranged from 20 to 50 periods of the incoming acoustic forcing. The time-step adopted for each simulation was kept tight enough to accurately reproduce the incoming wave, preventing undesirable aliasing. At the same time, the Courant-Friedrich-Lewy [114] constraint $CFL_{max} < 1$ was satisfied everywhere in the domain even for the grazing flow calculations. This led to a reduction of the dimensional time-step from 1 μs (used for the no grazing flow cases) to

20 ns for the grazing flow analyses at the highest Mach number.

4.6 Acoustic-induced flow at the orifice

As previously stated in this chapter, non-linear oscillations of the cross-flow jets are expected when liners operate at high SPLs or close to a resonant frequency. Although the highest noise suppression is observed only in case of resonance, the non-linear response of the system can be qualitatively evaluated from the shape of the pulsating jets driven by the acoustic excitation. For this reason, the present section discusses the characterization of the turbulent structures solved by the LES approach when non-linear jet oscillations occur. Such considerations are discussed for the SDOF cases only, although they can be easily extended to the multi-cavity results as well. In the rest of the section, the effect of increasing SPLs on the jets oscillation is discussed.

As it can be seen from Figure 4.12, a contraction of the oscillating jet flow area appears due to the viscous losses that reduce the effective mass flow rate across the orifice. The four visualizations collected in Figure 4.12 show the pulsating jet when varying the acoustic amplitude from 130 dB to 160 dB at a constant frequency of 3 kHz. Velocity vectors are superimposed on the velocity contours to outline both the viscous boundary layers on the orifice lateral wall and the potential jet core. The visualizations confirm that the increase in the wave amplitude leads to a more evident vortex generation above and below the liner neck. The asymmetry of the jet respect to the hole axis is due to the acoustic grazing wave that travels from left to right. To further stress this aspect, Q-criterion contours colored with the cross-flow jet velocity are displayed in Figures 4.13 and 4.15 for the single and the multi-orifice layouts respectively.

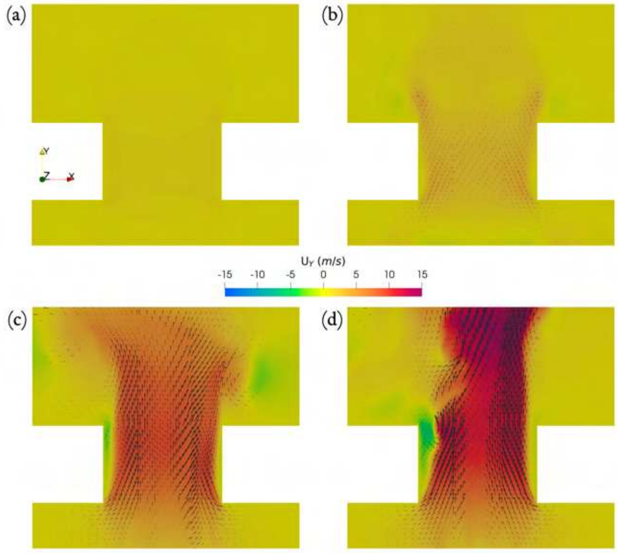

Figure 4.12: Jet velocity, f = 3 kHz: (a) 130 dB; (b) 140 dB; (c) 150 dB; (d) 160 dB.

To help detecting the main flow features at the orifice region, span-wise vorticity contours are plotted on the resonator mid-plane as well (see Figures 4.14 and 4.16). For both the cases, it is well clear that the transition to a fully non-linear regime occurs when the acoustic excitation amplitude is above 140 dB. Below this threshold, the 3 kHz acoustic forcing on the orifice section generates a very low jet oscillation. No major turbulent structures arise under this amplitude and the linearity of the jet oscillations can be assumed far from resonance. On the other hand, when the amplitude increases over 140 dB, the jet starts to penetrate more into the cavity and the upper domain box, progressively losing its original cylindrical shape. More in detail, when the oscillation regime becomes highly non-linear (e.g.

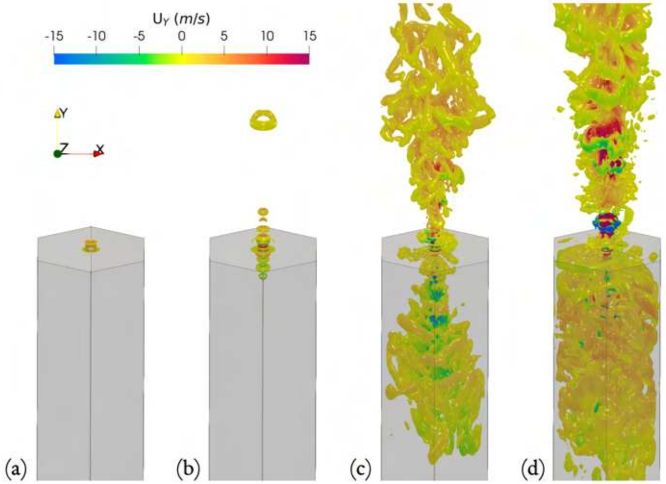

Figure 4.13: Q-criterion at different SPLs - single orifice: (a) 130 dB; (b) 140 dB; (c) 150 dB and (d) 160 dB.

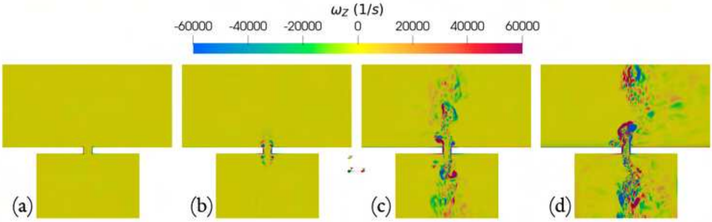

Figure 4.14: Spanwise vorticity contours - single orifice: : (a) 130 dB; (b) 140 dB; (c) 150 dB and (d) 160 dB.

150 dB), some coherent and toroidal structures are generated at the orifice rim. At the same time, the potential jet core starts to shrink and two viscous low-speed boundary regions become clearly visible on the orifice walls. These effects are magnified at the amplitude of 160 dB, when the jet oscillations are so intense to determine the breakdown of the coherent turbulence.

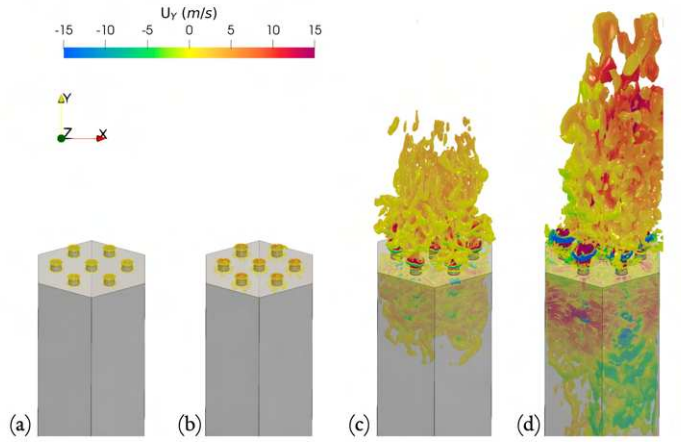

Figure 4.15: Q-criterion at different SPLs - multi orifice: : (a) 130 dB; (b) 140 dB; (c) 150 dB and (d) 160 dB.

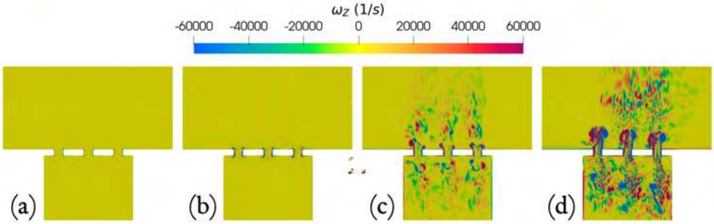

Figure 4.16: Spanwise vorticity contours - multi orifice: : (a) 130 dB; (b) 140 dB; (c) 150 dB and (d) 160 dB.

In other words, the higher the incoming acoustic energy is, the smaller and more energy-carrying eddies detach from the orifice. This also leads to a more evident wrinkling of the external jet surface which becomes highly irregular. Again the asymmetry of the jet structures at highly non-linear regimes are due to the presence of the grazing acoustic wave that propagates from left to right in all the visualizations. A similar behaviour of the cross-flow jet oscillation is expected also at resonance regardless of the SPL. However, non-linear oscillations due to high SPL do not mean great acoustic attenuation as this is obtained close to resonance only.

4.7 Impedance results

In this section, impedance evaluations of the three test-cases under investigation are reported. Firstly, the results from the LES of the multi-orifice single-cavity cell are compared with the experiments of Jones [102] and the semi-empirical model of Hersh [88] to validate the LES setup on a realistic liner pattern. For the grazing flow cases, comparisons have been made also with the numerical analysis conducted by Zhang and Bodony [99]. Then, the effects of the porosity on the resonator response are investigated: the acoustic impedance of the two different layouts are scaled by multiplying the resonator porosity to assess when different perforated panels can be somehow correlated. The numerical outcomes are compared again with the experiments of Jones [102] and the DNS of Zhang and Bodony [98]. Finally, the extended version of the Hersh model for MDOF liners is validated against the LES of the TDOF liner arrangement. Before showing the numerical results, the experimental two-microphone and three-microphone methods proposed by Dean [74] and Rademaker [85] for impedance evaluation must be illustrated. These techniques have been implemented into the OpenFOAM environment by including virtual microphones to derive the acoustic impedance from the LES results. The sketches of both the two- and the three-microphone in-situ methods are shown in Figure 4.17.

Mimicking an experimental rig, in case of SDOF systems,

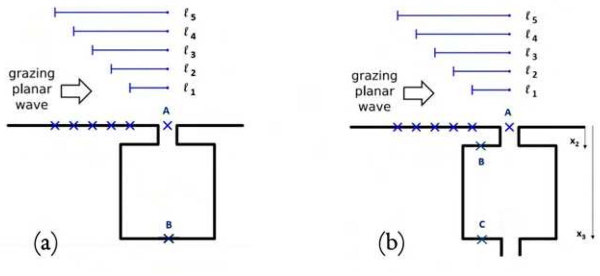

Figure 4.17: Probe array for the in-situ method application: (a) SDOF, (b) TDOF.

the acoustic signals were recorded by virtual pressure probes, at the cavity back-wall (B) and at the face-sheet center-line, upstream of the orifice aperture (A), as shown by Figure 4.17(a). For the TDOF configuration, the single-probe cavity acquisition is replaced by a couple of microphone placed in B and C as depicted in Figure 4.17(b). Since these in-situ techniques might suffer from the hydrodynamic influence of the pulsating jets, a set of five probes aligned with the face-sheet center-line was considered. The upstream distances at which the face-sheet probes were placed are respectively: $l_1 = 6d$, $l_2 = 12d$, $l_3 = 18d$, $l_4 = 24d$, $l_5 = 30d$, being d the orifice diameter. With regard to the multi-orifice SDOF cell, the same distances were referred to the orifice at the middle of the perforation pattern. The pressure signals are then processed by a DFT algorithm to derive the specific acoustic impedance of the liner element. In case of a SDOF configuration, specific acoustic impedance is obtained by using Equation 4.21 while for a TDOF one, Equation 4.22 is used.

$$z(\omega) = -j \frac{|p_A|}{|p_B|} \frac{e^{j\Phi_{AB}}}{sin(kL)} \tag{4.21}$$

$$z(\omega) = \frac{P_A P_A^* \sin(kL_1)}{P_C P_A^* i \cos(kx_2) - P_B P_A^* i \cos(kx_3)} \tag{4.22}$$

In the above expressions, L_i is the cavity depth, k is the acoustic wave number, Φ is the phase shifting between the face-sheet and the cavity pressure signals, P_i is the complex pressure amplitudes and x_2 and x_3 are the position along the grazing direction of the cavity microphones for the TDOF acquisition. Since from an experimental point of view it is unfeasible to place a microphone exactly at the orifice aperture, the acoustic pressure in A was reconstructed from the signal recorded by one of the face-sheet probes at position A_i. More precisely, knowing the linear distance l_i between the face-sheet probe and the orifice aperture, the grazing flow Mach number M and the excitation wavelength λ, the phase shift Φ_{AiA} between the acoustic signal at the probe and at the orifice aperture is given by:

$$\Phi_{A_i A} = \frac{2\pi l_i}{\lambda(1+M)} \tag{4.23}$$

Finally the phase shift Φ_{AB} in Equation 4.21 is retrieved by subtracting the translation term Φ_{AiA} to the acquired phase shift Φ_{AiB}.

4.7.1 Validation of the LES approach

In this subsection the acoustic impedance of the multi-orifice liner element coming from high fidelity simulations was compared with analytical and experimental benchmarks in order to validate the proposed LES approach.

1. **No-flow condition**

   The trends of the acoustic resistance and reactance for a 130 dB acoustic excitation are shown in Figure 4.18. Here, the frequency response predicted by the LES is represented by the black squares. The results coming from the semi-analytical Hersh model are represented by the red dashed line, while the light-blue circles and the blue pentagons come from Jones' acquisitions.

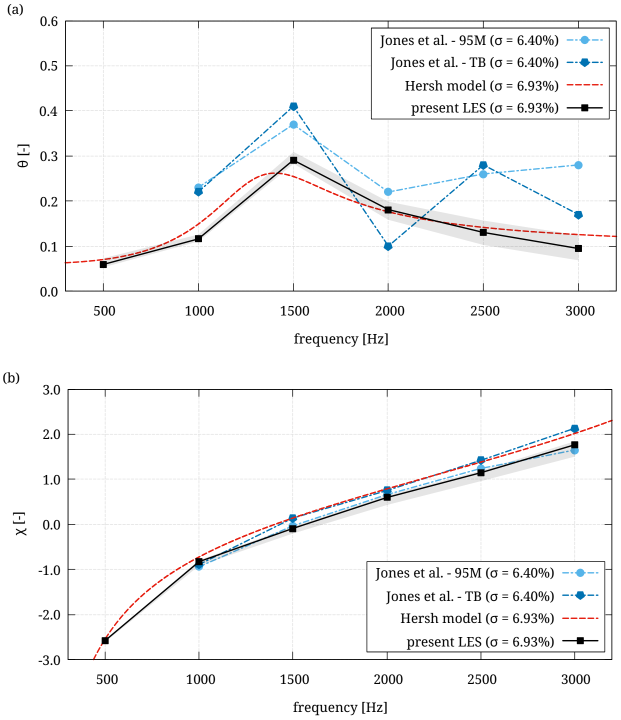

Figure 4.18: Specific resistance (a) and reactance (b) at fixed 130 dB SPL.

As shown in Figure 4.18, a good agreement between the LES results and the Hersh model is found for both the resistance and the reactance over the entire frequency range. To collapse LES impedance evaluations coming from the different probe A locations into a single black square an average on the face-sheet probe results has been taken. The shaded bandwidth across the black squares indicates the range of variation of the resistance and the reactance at each frequency. Looking at the experiments of Jones, it can be noted that the LES correctly detects the resistance peak at around 1.5 kHz which is predicted also by the Hersh model but at a slightly lower frequency. At the same time, the anticipation of the reactance zero crossing means that the Hersh model underestimates the resonant frequency at about 1.3 kHz. This discrepancy may come from the approximation of the seven-orifice perforation pattern with an equivalent single orifice with the same opening area. This assumption has been made as in the Hersh model formulation, a unique value for the discharge coefficient for a single hole was considered when implementing the formula to obtain the analytical resistance. Conversely, a marked mismatch between experiments and the LES results is visible for frequencies higher than the resonant one. Here the LES follows the trend of the Hersh model but it keeps decreasing instead of showing a secondary peak at around 2.5 kHz. It should be noted that the two experimental techniques (i.e., 95 microphones and traversing bar) used by Jones gave different results on the same liner geometry for frequencies higher than 1.5 kHz. The 95 microphone measurement is then considered the most reliable one, as it is not well clear why a secondary peak coming from the traversing bar method should appear in a locally reacting SDOF system. On the other hand, it should be considered that the porosity of the liner tested by Jones is not exactly the same of the one of the liner investigated by using the LES and the Hersh approaches. Since the liner porosity affects mainly the acoustic resistance evaluation, this might explain why greater deviations have been found on resistance, while reactance values have been predicted in an excellent agreement by all the three approaches.

Moving now to SPL effects, in Figure 4.19 the acoustic quantities are plotted against the SPL for an excitation frequency equal to 3 kHz. In this case the LES results are only compared with the Hersh model due to the lack of experiments at SPLs higher than 130 dB. From Figure 4.19 it

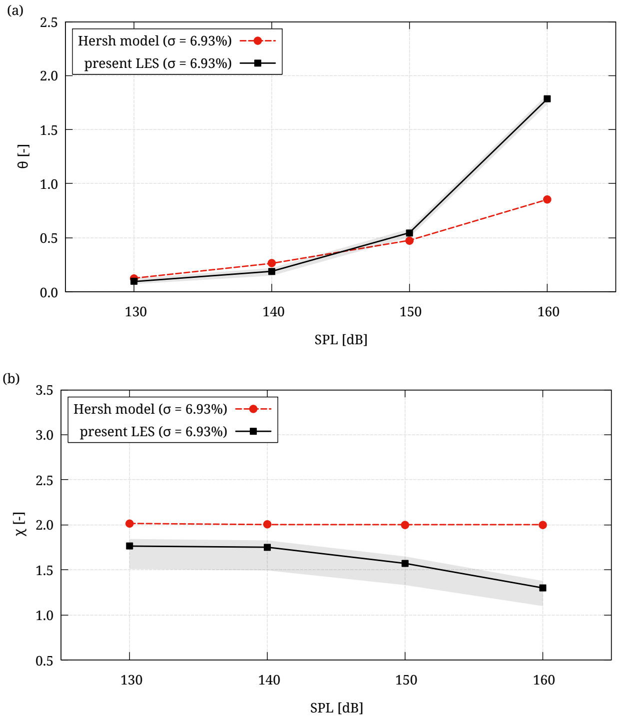

Figure 4.19: Specific resistance (a) and reactance (b) at fixed 3 kHz frequency.

can be observed that the sensitivity to the face-sheet probe location (gray band) affects the reactance estimation more than the resistance one. Moreover almost no effect of the SPL has been found on the bandwidth thickness meaning that the in-situ method of Dean is marginally influenced by the oscillation regime. Focusing on Figure 4.19(a), the numerical and the analytical resistance predictions agree well up to 150 dB. From this threshold on, an abrupt increase in the resistance is predicted by the LES so that at 160 dB the numerical resistance nearly doubles the analytical prediction. The reason behind this discrepancy is probably due to the lack of the cross-flow contribution when deriving the discharge coefficient through the Hersh model. More in detail, it can be deduced that the acoustic discharge coefficient coming from the LES simulation at 160 dB and 3 kHz is lower than the one computed in the analytical model. Since a lower discharge coefficient value implies a greater blockage on the orifice walls, the increase in acoustic resistance for the LES simulation is thus motivated. On the other hand, at the quasi-linear regimes, the jets oscillation is damped, thus reducing the hydrodynamic contribution to the overall discharge coefficient. As a result, a closer match between the Hersh model and the LES has been found at lower SPLs. Focusing now on reactance, the Hersh model predicts an almost constant reactance at all the investigated SPLs whereas a decreasing trend can be observed for the LES. This is again due to the way the Hersh model computes the discharge coefficient at the very high SPLs. According to the model implementation [88], the frequency dependency of the discharge coefficient is unaltered when a fully non-linear behavior of the acoustic system holds. This means that from a certain threshold on, the increasing SPL affects no more the resonator inertial length, leading to a constant reactance as shown by Figure 4.19(b). Actually, as the discharge coefficient would keep decreasing, a further reduction of the inertial length is expected, thus leading to a decreasing reactance as well. In other words, it can be concluded that from the Hersh model, almost the same amount of non-linearity is predicted for SPLs ranging from 130 dB to 160 dB. Conversely, the LES shows a tendency towards a quasi-linear response for SPLs equal to 130 dB or 140 dB, locating the fully non-linearity threshold beyond 150 dB. The difference between the numerical and the analytical approaches might lie once again in the reduction of the seven-orifice pattern to an equivalent single orifice configuration when applying the Hersh model. More in detail, the number of orifices and the perforation pattern may determine conjugate interactions between the pulsating jets that are not modelled by the analytical approach.

2. **The grazing-flow condition**

   For the grazing flow cases A10-A11 presented in Table 4.3, LES results have been compared with the numerical work of Zhang and Bodony [99] and the experiments of Jones [102] separately. More precisely, an excitation at 1.5 kHz was superimposed on a M = 0.3 grazing flow Mach number to recreate the experiments of Jones, while a 3.0 kHz excitation with M = 0.5 grazing flow Mach number have been selected to replicate the DNS of Zhang and Bodony [99]. Looking at Figure 4.20(a) it can be seen that the present LES calculations strongly underestimate acoustic resistance when compared to the experiments. This is probably due by the laminar boundary layer of the grazing flow at the face-sheet holes in the upper box of the numerical domain. It should be recalled that in the LES setup, no turbulent inflow was provided at the domain inlet and the upstream distance is not long enough to promote the boundary layer transition that is then triggered downstream of the holes by the pulsating jet as it will be explained later on. The effect of the laminar boundary layer is evident also from Figure 4.20(b), where the comparisons with Zhang and Bodony [99] of the acoustic quantities are reported. In their work, Zhang and Bodony imposed both laminar and turbulent LES inflows, stressing that the normalized acoustic resistance σ θ is expected almost to triple if a turbulent inflow is prescribed (see the resistance bars in Figure 4.20(b)). This was demonstrated for a single-orifice liner but it can be reasonably concluded that the same holds for any perforation pattern. Indeed, the bars referring to the seven-orifice configuration under a laminar grazing flow are in good agreement in terms of acoustic resistance. This is a further prove of the influence of the boundary layer characteristic on the liner performance. The explanation to this evidence lies in the amount of energy carried by a laminar and turbulent boundary layers. It is known that turbulent transition enhances the momentum mixing inside the boundary layer so that a higher acoustic energy must be supplied to make the jet penetrate the boundary layer over the orifices. As a consequence, this means that turbulent boundary layers hamper more the feeding of resonators due to the incoming forcing, leading to an increase in the acoustic resistance. This aspect will

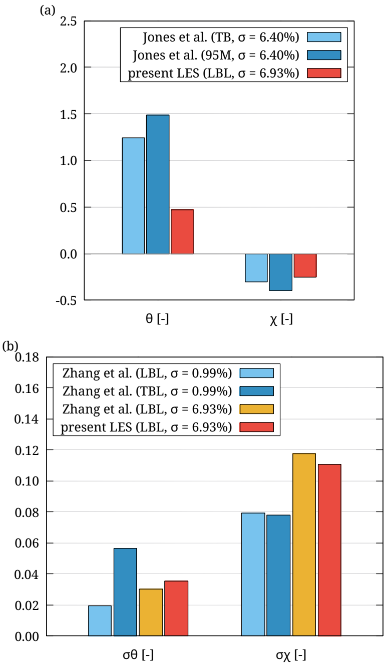

Figure 4.20: Effect of the grazing flow boundary layer on resistance and reactance: M = 0.3, f = 1.5 kHz (a); M = 0.5, f = 3.0 kHz (b).

be further investigated in the MDOF subsection where the LES results will be used as a validation tool.

4.7.2 Effect of porosity on acoustic absorption

This part of the chapter is focused on the effect of the perforation porosity on acoustic impedance of the liner resonators. The aim of this part of the work is to demonstrate when liners with different perforated face-sheets can be acoustically correlated as done by Zhang and Bodony in their works. To do so, the acoustic performance of different liner resonators must be expressed in terms of the acoustic resistance and reactance multiplied by the porosity of the liner. In this context, the acoustic responses of both the single and the multi-orifice cells are compared to the experiments of Jones [102] and the DNS of Zhang and Bodony [98]. Since experimental data are available for a fixed 130 dB SPL value, only the frequency response of single- and multi-orifice liner resonators has been investigated. A summary of the porosity values under investigation is reported in Table 4.7.

Case	Porosity (σ)
Single-orifice present LES	0.99%
Multi-orifice present LES	6.93%
Jones Experiments Low Porosity	6.40%
Jones Experiments High Porosity	15.00%
Zhang-Bodony DNS	0.99%

Table 4.7: Porosity values for different test-cases.

The normalized acoustic resistance and reactance of the investigated resonators are shown in Figure 4.21. From both the graphs, it can be noted that for frequencies higher than 2.5 kHz the present LES well agrees with the DNS by Zhang and Bodony both in terms of resistance and reactance. This suggests that liner with different porosity and perforation pattern are expected to be correlated at high frequencies. On the other hand, when moving to lower frequencies, major differences when collapsing the normalized resistance become evident also between numerical outcomes. Similar considerations can be made for the normalized reactance although the scaling by the porosity seems to work better than applied to resistance. However, even for the normalized reactance a discrepancy between the response of each

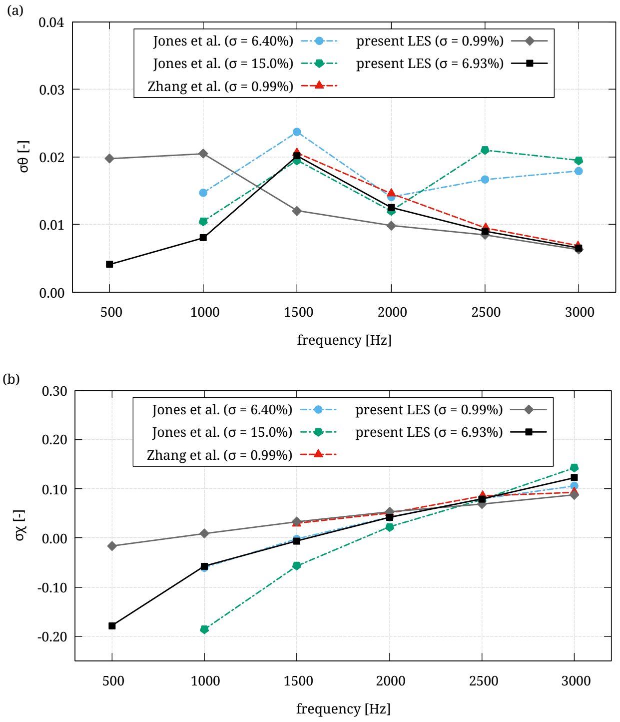

Figure 4.21: Normalized resistance (a) and reactance (b) for different perforation patterns.

resonator has been found at low frequencies. The explanation to these trends lies in the way the porosity enters into the resonator response. To stress and explain this aspect, the analytical resistance and reactance derived by using the Hersh model are displayed in Figure 4.22 for porosity values equal to: $\sigma_1 = 0.99$ %, $\sigma_2 = 6.93$ %, $\sigma_3 = 14.85$ %. It is worth noting that porosity in the Hersh model implementation refers to an arrangement of one, seven and fifteen orifices respectively, each one of the same diameter $d = 0.99$ mm. From both the graphs of Figure 4.22 it is clear that an increase in the liner porosity shifts the resonant

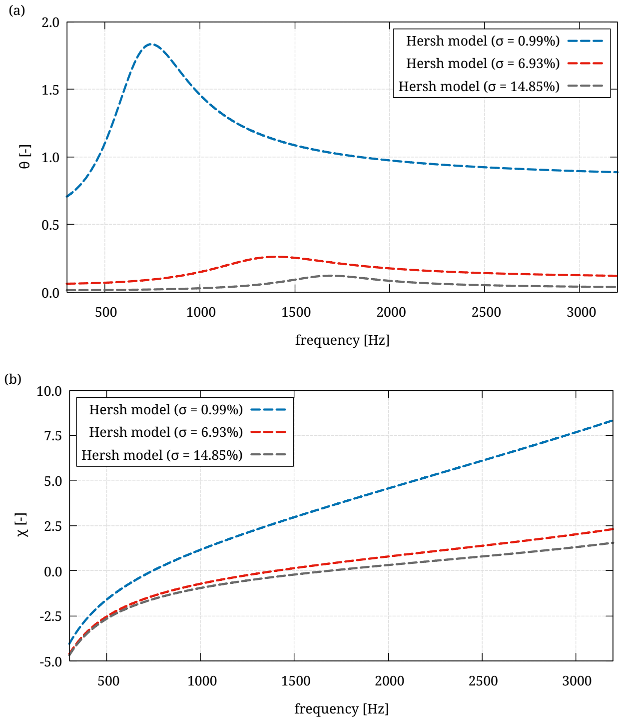

Figure 4.22: Acoustic resistance and reactance predicted by the Hersh model as functions of the porosity.

frequency towards higher values. For this reason, the reactance vanishing and the resistance peak move from 750 Hz to 1700 Hz as the porosity ranges from σ_1 to σ_3. Moreover, the higher the porosity, the lower viscous losses are expected. However, to understand when different resonators can be correlated from an acoustical point of view, the resistance and the reactance trends should be analysed separately. From Figure 4.22(b) is straightforward that in terms of reactance, the frequency response of the three resonators will always be different at the very low frequencies. More in detail, the convergent trend of all the three curves implies that the normalized reactance will take three different values, being the specific reactance χ of the three resonator almost the same. This also explains the large deviations of normalized reactance at low frequencies shown in Figure 4.21. A further interesting aspect is the saturation of both the resistance and reactance when increasing the liner porosity. More precisely, a plummet in both resistance and reactance is found moving from $\sigma_1 = 0.99\%$ to $\sigma_2 = 6.93\%$. Then, a further increase in porosity up to $\sigma_3 = 14.85\%$ results in a marginal downward displacement of the resonator response. This means that for intermediate and high porosity values an acoustic similarity between resonators is once again hardly possible. Finally, it can be noted that at high frequencies, an acoustical similarity between the low and the intermediate-porosity resonators may be found for both the acoustic quantities. The close matching between the curves in Figure 4.21 is now due to the large gap in the acoustic quantities predictions when moving from a porosity of $\sigma_1 = 0.99\%$ to $\sigma_2 = 6.93\%$. In conclusion, it has been demonstrated that an acoustic correlation between liners with different porosity holds at high frequencies and low to medium perforation porosity.

4.7.3 Validation of the MDOF Hersh model

The in-house recursive formulation of the Hersh semi-analytical model [87] has been validated for a TDOF resonator under the effect of the acoustic excitation frequency and of grazing flow separately.

1. **The no-flow condition**

   The frequency response of the TDOF liner in terms of acoustic resistance and reactance in case of no grazing flow is shown in Figure 4.23. The black dotted curve repre-

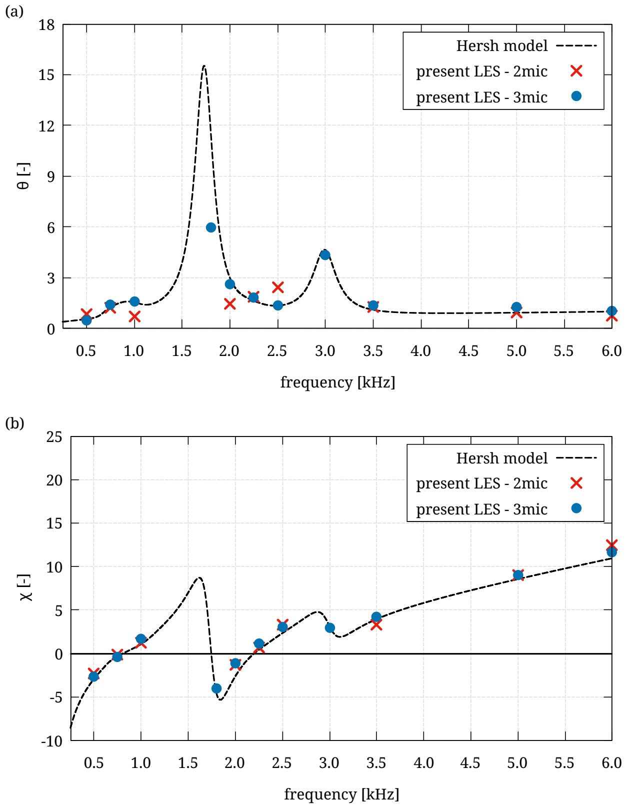

Figure 4.23: Specific resistance (a) and reactance of the TDOF at 130 dB SPL in absence of grazing flow.

sents the trends predicted by the extended version of the Hersh model, while the red crosses and the blue dots report the LES results calculated through the original two-microphone method of Dean [74] and the three-microphone method of Rademaker [85] respectively. The two methods for the impedance eduction can be also used to investigate at which conditions MDOF and SDOF liners have similar acoustic responses. This is possible when the two methods return similar results, meaning that the TDOF resonator can be approximated with an equivalent SDOF one. This is thus a direct consequence of the applicability of the two-microphone method of Dean [74] to SDOF resonators only. An arithmetic average was used to collapse the set of five face-sheet acquisitions into the crosses or dots displayed in Figure 4.23. Looking at the two graphs, a close match between the red crosses and the blue dots is found for excitation frequencies lower than 1.0 kHz and higher than 3.5 kHz. This suggests that in these frequency ranges, the TDOF resonator acoustically behaves as a SDOF one and thus a TDOF-to-SDOF approximation holds. Obviously, the equivalent cavity depth to be considered when making this approximation varies with the frequency. The key point is that the TDOF can be reduced to a SDOF system if there is no driving pressure gradient across one or more orifices. When this happens, the perforation acts as a rigid wall and it can be considered as the back-wall where the flush-mounted microphone of the two-microphone acquisition technique can be placed. The depth at which the flush-mounted microphone is placed also sets the equivalent cavity depth for the TDOF-to-SDOF analogy. An intuitive way to derive the equivalent SDOF depth consists in looking at the oscillations of the jets across each orifice of the TDOF liner element. An example is provided in Figures 4.24, 4.25, 4.26 and 4.27 where instantaneous vorticity contours and the pulsating jet velocity during one oscillation period at the three orifices are reported for cases C2, C4, C6 and C11 of Table 4.5. As visible from Figure 4.24, in-phase oscillations are present at all the three orifices at f

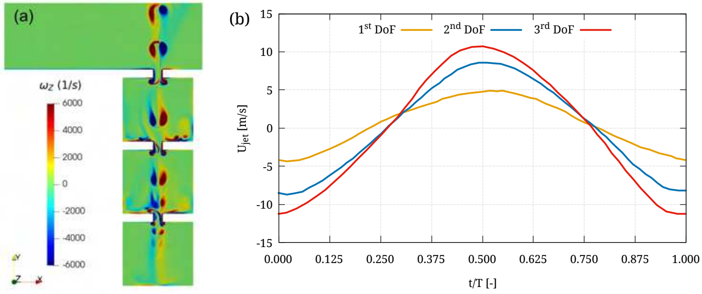

Figure 4.24: Span-wise vorticity contours (a) and jets oscillations (b) at f = 0.75 kHz.

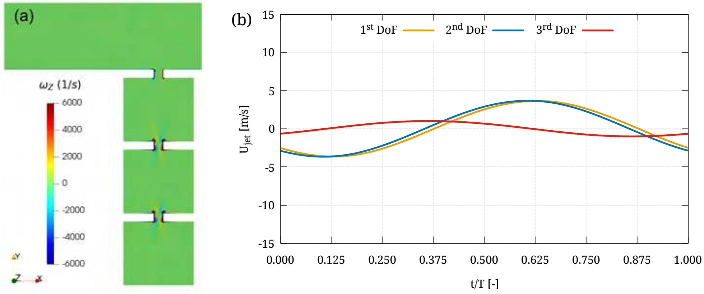

Figure 4.25: Span-wise vorticity contours (a) and jets oscillations (b) at f = 1.80 kHz.

= 0.75 kHz. This is confirmed from both the vorticity contours and the in-phase time-varying velocities of the jets during one oscillation cycle. Following a mechanical analogy, it can be affirmed that this situation mimics linearly dependent oscillations of the three degrees of freedom and a reduction from three to one degree of freedom is permitted. This is consistent with having approximated the TDOF system with a SDOF one with a cavity depth equal to the total size of the TDOF. Therefore, the second flush-microphone can be placed at the last cavity back-wall since

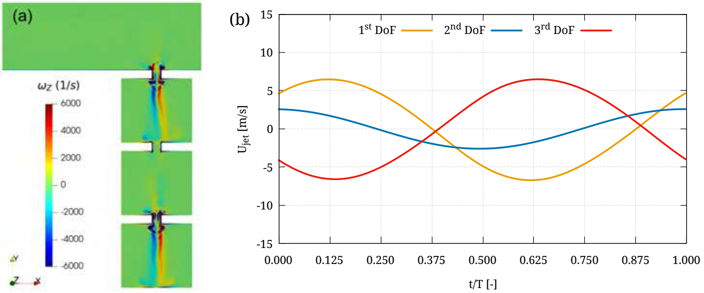

Figure 4.26: Span-wise vorticity contours (a) and jets oscillations (b) at f = 2.25 kHz.

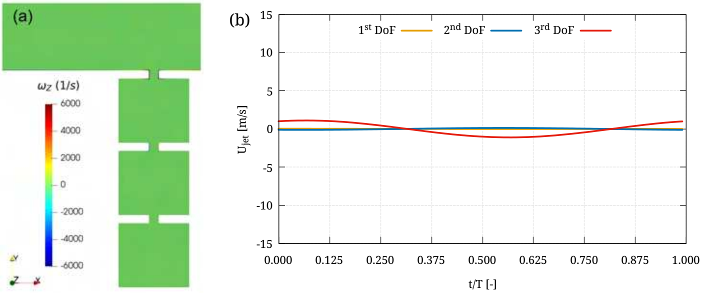

Figure 4.27: Span-wise vorticity contours (a) and jets oscillations (b) at f = 6.00 kHz.

the two septa do not alter the resonator acoustics. Conversely, at 6 kHz (see Figure 4.27) only a small jet pulsation is visible at the upper orifice. This means that no driving pressure gradient acts on the middle and the lower orifices and the flush-mounted microphone can be placed on the upper septum. Thus, the two-microphone method can be enforced at 6 kHz on a reduced SDOF geometry with an equivalent cavity depth of one third of the original TDOF total size. On the other hand, in the frequency range between 1 kHz and 3.5 kHz the two- and the three-microphone methods return impedance values that differ quite a lot each other. This is evident for resistance while reactance seems to be less affected. The motivation of the resistance discrepancies lies in the oscillating behavior of the TDOF system within this frequency range. Here, the conditions of no driving pressure gradient at any orifice and in-phase oscillations of the jets are never met. This is due to the presence of the two anti-resonances of the TDOF system that makes impossible to decouple such linearly independent oscillations. This is clearly shown in Figure 4.25 where the 1.8 kHz anti-resonance leads to perfectly coupled oscillations of the second and the third jets, nearly suppressing the first one. Similarly, from Figure 4.26 it can be noted that uncoupled oscillations are present for all the degrees of freedom. As a result, the SDOF-to-TDOF analogy holds no more and the two-microphone in-situ acquisition fails in predicting either the trend and the correct values of acoustic resistance. For this reason, the validation of the extended Hersh model was better achieved with the three-microphone method instead of the two-microphone one used in [103]. Again, from Figure 4.23 it can be observed that the black dotted curve well agrees with the blue dots on the entire frequency range for both the acoustic quantities. In fact, numerical and analytical predictions of resistance only deviate at around 1.8 kHz where the extended Hersh model prediction lies above the LES result. This is due to the steep slope of the curve coming from an anti-resonance condition. In this region of the curve, acoustic resistance is very sensitive to a change in excitation frequency, so that just a little modification of the acoustic frequency can lead to large variations of acoustic resistance.

However, this is not an actual concern as no acoustic absorption is obtained at one anti-resonance, regardless of the value the acoustic resistance takes. At the same time, it can be noted that by using a three-microphone technique an excellent agreement between numerical and analytical results is found also within the 1-to-3.5 kHz frequency range. In conclusion, the zero-flow analyses impedance results discussed in this section were aimed not only at validating the extended analytical model, but also at underlining in which cases the TDOF resonator behaves as an equivalent SDOF one from an acoustical perspective. A more detailed discussion about this last topic was faced in [103].

2. **The grazing flow condition**

   This last part of the chapter is dedicated to the validation of the extended Hersh model under the effect of a laminar grazing flow. To do so, the grazing flow simulations have been run at the first resonant condition (f = 0.75 kHz), keeping constant the excitation amplitude to 130 dB. An upper limit of M = 0.3 was dictated by computational cost reasons. Having already demonstrated that the three-microphone method outperforms the two-microphone one for TDOF resonators, the LES were post-processed using the Rademaker approach [85] only. In Figure 4.28, the acoustic quantities are plotted against the grazing flow Mach number. The red circles represents the LES results, while the black squares comes from the extended analytical model. Looking at the resistant component, the increasing trend of resistance with the grazing flow speed is predicted by both the approaches. This behavior is definitely reasonable as the grazing flow shields the resonator from being

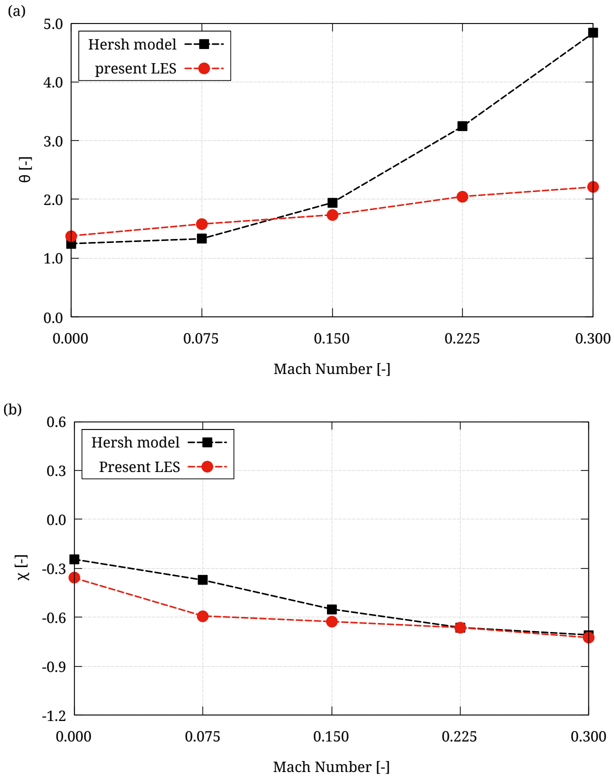

Figure 4.28: Effect of the grazing flow on specific resistance (a) and reactance (b) of the TDOF at f = 0.75 kHz, SPL = 130 dB.

fed with the incoming acoustic excitation. Therefore, resistance is expected to grow since it can be thought as a measure of the permeability of the resonator branch. However, the resistance growth rate is much higher when using the analytical model. This trend becomes evident starting from M = 0.075 onward, and the intersection between the red and the black curves occurs at around M = 0.0875.

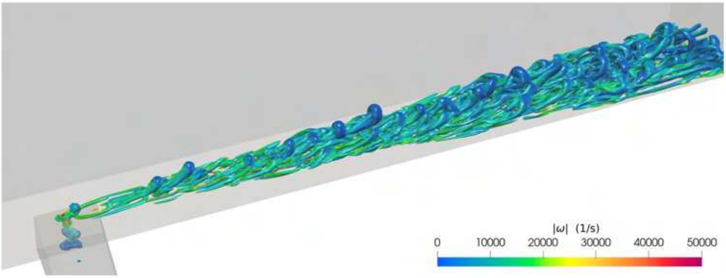

Figure 4.29: Q-crit contours colored with vorticity magnitude for the TDOF element at f = 750 Hz, SPL = 130 dB, and M = 0.075.

Again, the explanation to these trends lies in the characteristic of the boundary layer at the orifice. As for the SDOF cases at SPL = 130 dB, the presence of a laminar grazing inflow in the LES, promotes the generation of a pulsating jet across the orifice resulting in a lower resistance value. As shown in Figure 4.29, the boundary layer transition occurs only downstream of the orifice, triggered by the acoustically driven pulsating jets. At the same time, the constants and the coefficients of the analytical Hersh model are tuned at high grazing flow speed, for which the boundary layer over the face-sheet orifices is surely turbulent thus increasing resistance. An additional reason behind the resistance discrepancy at high Mach number can be due to the linearization hypothesis made for the middle and the lower cavities. More precisely, the absence in the model of an acoustic discharge coefficient for the middle and the lower orifices might have affected the recursive link between the acoustic impedance of each degree of freedom of the TDOF resonator.

Focusing now on Figure 4.28(b), a very good agreement between the analytical and the numerical results is found. Both the approaches predict the reactance decreasing with the grazing flow Mach number and a slight shifting of the resonant frequency to higher values. Moreover, the flattening of both the curves is visible when increasing the Mach number, meaning that no further influence of the grazing flow is expected from a certain threshold onward. The flattening trend is more pronounced on the LES curve implying that the saturating behavior is anticipated with respect to the analytical model. This aspect can be related to the way the inertial lengths are modelled as their formulation affect the analytical model. It can be reasonably assumed that a non-linear modelling at all the degrees of freedom might improve the matching between numerical and analytical results, especially at the lower grazing flow Mach numbers. To further discuss the non-linearity due to the grazing flow, some additional considerations can be made by comparing at the vorticity contours in Figure 4.30. The different grazing flow speeds do not strongly affect the oscillation patterns across the internal orifices which are very similar to the ones shown in Figure 4.24 for the no-flow case. Since a contraction of the jet flow is clearly visible also for the second and the third degrees of freedom, it can be easily deduced that the linearization hypothesis is not well posed when the excitation frequency is close to resonance. Furthermore Figure 4.30 shows that some flow vorticity is still produced at the upper cavity for M $= 0.3$ even though the amount of acoustic energy that enters the resonator branch is reduced. This explains the slow decrease of reactance, and the marginal effect of the grazing

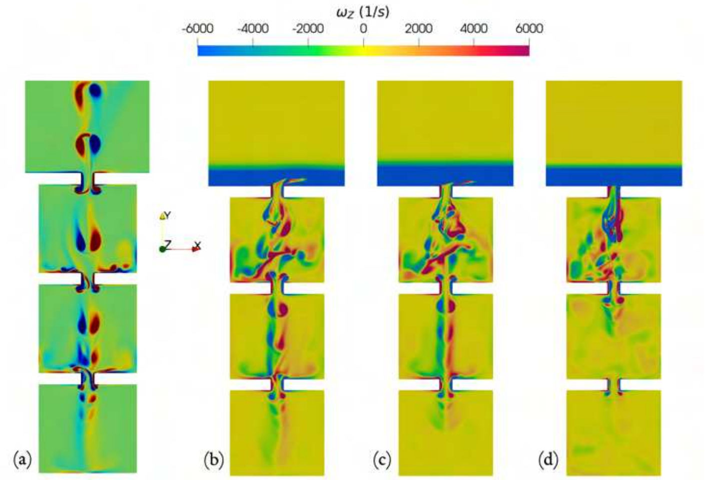

Figure 4.30: Span-wise vorticity contours at different grazing flow Mach numbers: (a) no-flow; (b) M = 0.075; (c) M = 0.150; (d) M= 0.300.

flow speed on the resonant frequency of the TDOF resonator. Looking at Figure 4.28(b), the acoustic reactance decreases from -0.2 at the no-flow condition, to -0.7 at M = 0.3, meaning that for an excitation frequency of 750 Hz the liner is still working close to resonance also when grazing flow is present. Finally, it can be concluded that the good agreement between the extended Hersh model and the LES under grazing flow conditions is limited to the reactance component as long as a laminar grazing inflow is prescribed at the LES. With respect to the resistance component, further investigations are needed to demonstrate that turbulent inflow simulations can fill the gap between LES and analytical predictions.

5

Jet noise

In the first part of the chapter, some aspects about the working principle of chevron nozzles for jet noise attenuation are discussed. A literature review on the available methods to tackle the jet noise topic is also present and it anticipates the outcomes of this research. The latter has been oriented to replicate the experiments of Tanna [115, 116] for the round SMC-000 and chevron SMC-001 nozzles.

5.1 Chevron nozzles

Chevron nozzles are a saw-tooth shaping of the exhaust nozzle rim that can be applied on both the core and the bypass nozzles (see Figure 5.1) of turbofan engines to reduce jet noise. The latter is originated by the mixing of jet streams at different temperature expelled through the nozzles to achieve the engine thrust. However, when the bypass (cold) and the core (hot) streams meet together at the exhaust, the shear layer mixing at the interface is hampered by the density gradient of the two

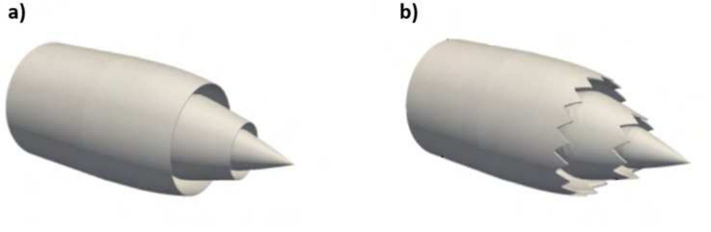

Figure 5.1: Round (a) and chevron (b) nozzles geometry.

streams. Hence, a huge amount of low-medium frequency broadband noise is expected, as well as a rise in the drag force on the airplane. The same issues arise also at the bypass duct exhaust rim due to the interaction of the bypass jet with the surrounding atmosphere. Here, large velocity gradients in the shear layer are expected especially at takeoff when the cold jet flows in a still atmosphere. A sketch showing the main regions of an exhaust jet is reported in Figure 5.2.

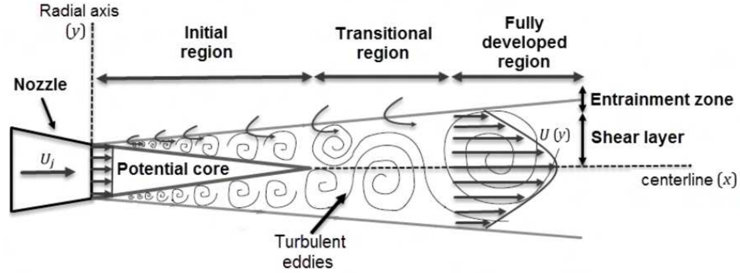

Figure 5.2: Shear layer regions for an exhaust jet.

It can be noted that in the initial region of the shear layer, small eddies are generated due to the velocity gap of fluid particles at the interface between the two jet streams or a jet stream and the surrounding fluid. These eddies comes from the rolling up of Kelvin-Helmholtz (KH) instabilities that mix together moving downstream of the exhaust. The coalescence of small turbulent eddies into larger ones motivates the broadband characteristic of jet noise, as different time scales are responsible for different noise frequencies in the spectrum. From Figure 5.2 it can be also observed that the conical region of influence of jet noise is wrapped around a potential jet core where viscous effect can be neglected. The length of this core is defined as the axial distance from the nozzle exit at which the center-line velocity is the 90 % of the one at the exit section. The length of the potential core is directly related to the amount of noise generated by the shear layer. It can be proved that shorter potential cores means faster turbulent mixing and thus less jet noise. The nozzle geometry and the co-flow stream characteristics are found to affect the potential jet core length, as demonstrated by experiments [117, 118] and calculations [119, 120]. The role of chevron nozzles for jet noise attenuation consists in producing stream-wise vorticity which enhances the turbulent mixing of the shear layer. In this way, smaller eddies are generated at the exhaust rim and a faster decay of the axial jet velocity is also observed. In other words, the saw-tooth pattern of the exhaust rim is designed to shift the broadband noise peak to higher frequencies which are more effectively dampened by the atmosphere. It can be demonstrated that atmospheric absorption is promoted at high frequencies and in case of high level of relative humidity [121].

Chevron nozzles are manufactured by cutting the exit rim of a round nozzle with an Electro Discharge Machining (EDM) process so to create an alternate pattern of notches and apexes along the exit circumference. To design a chevron nozzle, the circumferential angle (ϕ), the radial penetration (p) and the axial length (L) of the chevron teeth must be chosen. A recap of the chevron nozzle geometric parameters is illustrated in Figure 5.3 where an axial cross section and a rear view of a chevron nozzle are reported. According to Bridges and Brown [122], another important parameter to assess the chevron nozzle performance is the so called vortex strength (Γ). This represents the slope of the chevron edge projected onto a plane normal to the jet axis. With reference to Figure 5.4, the vortex strength can be calculated as the derivative of the local radius r with respect to the curvilinear coordinate s:

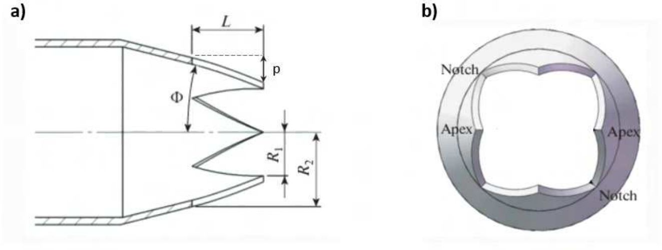

Figure 5.3: Chevron nozzle geometrical parameters: cross-section (a) and rear view (b) .

$$\Gamma = \frac{\partial r}{\partial s} \tag{5.1}$$

The vortex strength parameter is a measure of how much the chevron pattern interacts with the exhaust jet. A large value of Γ means that the chevron teeth soak more into the jet stream and thus a stronger impact of the chevron nozzle on noise emissions is obtained. The Γ parameter is also a similarity parameter for the design of the saw-tooth shape, as the same vortex strength

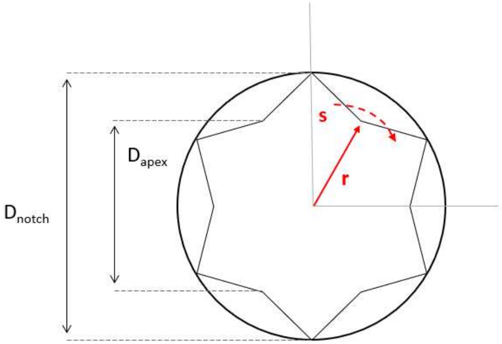

Figure 5.4: Deflection of the nozzle rim due to chevron shaping.

can be achieved through different combinations of teeth lengths and penetrations.

5.2 Investigation on turbulence noise

The topic of noise generation from turbulence was historically tackled with experimental methods aimed at deriving some cross-correlation functions to link the flow variables with the far field noise. More specifically, cross-correlation functions are measurable quantities that indicate the level of coherence between two acquired signals. This allows for a clear understating on the physics of turbulence noise regardless of the theoretical modelling of noise sources. In this context, starting from the early 70s, Seiner and Reethof [123] firstly exploited hot-wire and microphone measurements to demonstrate the high level of correlation between the far field acquisitions and aerodynamic sources located in the potential core of a round subsonic jet. Another contribution to this topic was provided by Schaffar [124] who experimentally identified a noise source in a choked cold jet using a velocimeter to correlate the far field noise with the axial velocity fluctuations inside the jet. Later on, jet noise diagnostic was performed by Richarz [125] who replaced the hot-wire acquisition with the Laser Doppler Velocimetry (LDV) technique to avoid spoiling the measurements because of the anemometer presence. Furthermore, in the work of Armstrong, Michalke and Fuchs [126] it was shown that cross-correlation functions depend on both the jet Mach number and the circumferential location of the pressure measurement. More in detail, it was found that the correlation level between the jet fluctuations and the far field sound is progressively lost for low Mach number jets or increasing the angle between the far field acquisition and the jet axis. More recently, thanks to important improvements in the measurement instrumentation, further in-depth analyses were conducted on jet noise cross-correlation. For instance, Panda and Seasholtz [127] correlated the noise peak and the direction of emission using the scattering Rayleigh technique. Then, Bogey and Bailly [128] investigated the effects of the Mach and the Reynolds numbers on jet noise, concluding that the maximum of the cross-correlation occurs at end of the potential core. At the same time, Tam et al. [129] experimentally demonstrated that jet noise from small-scale turbulence is almost omni-directional while its directional content comes from the large-scale turbulence downstream of the nozzle exit. Focusing on chevron nozzles, more recent experimental campaigns were conducted by Bridges and Brown [122] at the NASA facility. Here the authors took far field noise measurements for the parametric family of the Simple Metal Chevron (SMC) nozzles, varying the count, the penetration and the length of the chevron teeth. It was found that the penetration acts mainly on shifting the noise peak while an increase in the teeth count plays an important role in reducing the overall emissions. Similar considerations were traced also by Callender et al. [130] who studied three chevron nozzle arrangements in heated and co-flow working conditions. Another remarkable piece of work is the one of Alkislar et al. [131] where the axial vorticity structures coming from the usage of chevron nozzles and micro-jet injection are compared. Moreover, some military investigations on supersonic jets exiting convergent-divergent nozzles were conducted by Munday et al. [132] and Schinkler et al. [133] to understand the role of chevron nozzles in altering the shock cells and cancelling screech tones. However, although experiments are essential for CFD codes validation, they do not still provide general guidelines for the design of chevron nozzles, as the way the test rigs alter the jet flow is not fully understood. Another drawback lies in the difficulty of measuring the flow properties just downstream of the nozzle exit with an experimental apparatus, due to the very thin shear layer in this region. This is an issue as a proper characterization of the jet flow structures in the initial shear layer is crucial to further explain how jet noise is spread over the turbulent spectrum.

For all these reasons, in the last years CFD methods are becoming more and more appealing to overcome the limitations of experimental approaches. However, RANS-based simulations [134, 135] were proven to be unable to correctly predict the far field noise due to the lack of resolved spectral content of the jet flow. Thus, scale-resolved LES computations were firstly performed by Shur et al. [136] even if the authors did not simulate the chevron geometry but they just prescribed the saw-tooth pattern to the initial shear layer. Relevant contributions to this field were carried by Uzun and Hussaini [137, 138, 139] who used the LES to simulate the full-annular configurations of the SMC-001 and the SMC-006 chevron nozzles (details in [122]). In their first work [137], the authors put the stress on the strong impact of the axial domain extension for a correct representation of all the frequencies of the noise spectrum. Then, in [138] it was demonstrated the need for having a proper mesh refinement close to the nozzle exit to correctly detect the high frequency sources of noise. Finally, in [139] other issues like the generation of a turbulent inflow and the computational effort of running LES for high Reynolds jets are discussed. Another paper dealing with scale-resolved simulations of far field noise from chevron nozzle flows is the one of Xia et al. [140]. Here the authors suggest a hybrid RANS-LES approach coupled with a FWH extraction of the radiated far field noise. The core of the paper is on the high accuracy of the far field predictions achievable with relatively light meshes thanks to the hybrid technique. More in-depth analyses on both the acoustic emissions and the chevron jet features are presented in the work of Stich and Housman [141]. In this paper, WMLES calculations are carried out on a round and a chevron nozzle (i.e., SMC-000 and SMC-001) and compared with the experiments of Bridges and Brown [122] on the same geometries. A well documented mesh sensitivity analysis was also performed by the authors to judge the reliability of the far field noise predicted using the FWH analogy extraction method. A key aspect of this work lies in the cost affordability of the WMLES for such applications, as the authors also demonstrated a reduction of one order of magnitude compared to a their prior work [142] thanks to the explicit time-stepping of the WMLES.

5.3 Test Cases

This section is thought to provide details on the numerical simulations conducted on the round SMC-000 and chevron SMC-001 nozzles. Firstly the geometry and the operative conditions of the two nozzles are described, then numerical aspects of the CFD setup are discussed.

5.3.1 Geometry and mesh

The baseline round SMC-000 is a subsonic nozzle whose geometric parameters are reported in Table 5.1. A schematic view of the nozzle is displayed in Figure 5.5 for further clarification.

Inlet diameter D_i	152.5 mm
Exit diameter D_e	50.8 mm
Nozzle length l	215.9 mm
Rim thickness t	1.5 mm
Exhaust Angle α	5.0°

Table 5.1: Geometric parameters of the SMC000 round nozzle.

As visible from Figure 5.5, the nozzle is assembled by screwing a round end to the baseline main structure. Hence, the different configurations of the SMC chevron nozzle family [122] can be obtained just replacing the terminal part of the round nozzle with the desired saw-tooth end. It is worth mentioning that in this work, the outline of the nozzle is not exactly the same as the one depicted in Figure 5.5, as no information on the actual shaping of the nozzle profile was found. However, this is supposed not to be an issue as the original dimensions of Table 5.1 were preserved and the aerodynamic of the nozzle flow is not expected

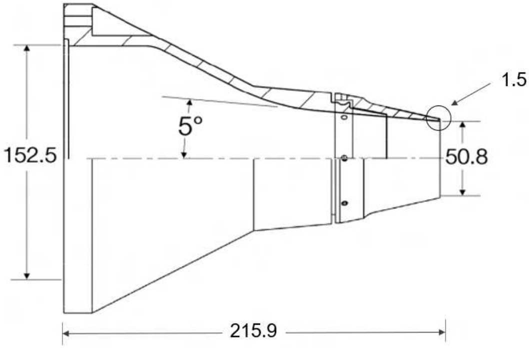

Figure 5.5: Cross section of the SMC000 round nozzle.

to be affected by the nozzle outline.

With regard to the SMC-001 chevron nozzle, a summary of the saw-tooth pattern geometry is given in Table 5.2. As stated above, the main structure of the nozzle is kept unaltered. The chevron pattern is produced carving the notches starting from the original exit diameter, thus the 50.8 mm value of the exit diameter is to be intended as the apex diameter (see Figure 5.4). The notch diameter D_n is derived by adding twice the penetration p to the apex diameter D_a.

Notch diameter D_n	52.77 mm
Apex diameter D_a	50.8 mm
Chevron length L	22.6 mm
Chevron penetration p	0.985 mm
Chevron angle ϕ	60.0°

Table 5.2: Geometric parameters of the SMC001 chevron nozzle.

The geometry of both the nozzles was created using the SolidWorks CAD software. Here an outer fluid domain was constructed to wrap around the full annular shape of the nozzles. The outer domain sizing was chosen following the hints provided by Uzun [138] about the minimum required axial and the radial extensions for jet noise applications. Thus, an axial length of $40D_e$ was considered enough to let the shear layer developing downstream of the nozzle exit, while a progressively increasing radial extension from $30D_e$ to $40D_e$ was decided to prevent spurious boundary effects on the jet flow. The outer outline of the domain was arbitrarily chosen to follow the conical spreading of the jet shear layer. A smooth curve was used to join the inlet and the outlet sections as this strategy helps in creating a higher quality mesh close to the boundary. Details of the two nozzle ends and a meridional view of the entire domain are reported in Figure 5.6.

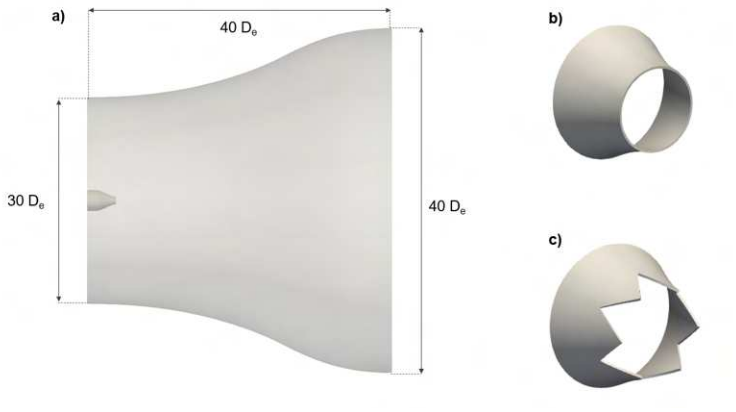

Figure 5.6: Numerical domain geometry: outer domain (a), round end (b), chevron end (c).

The boundaries of the numerical domain in Figure 5.6a were saved as .stl files and exported from the SolidWorks environment to the CFMesh, ready to be handled by the *cartesianMesh* application. Two meshes were built to perform a sensitivity study, as explained later on. An image of the final mesh and a zoom on the jet region is visible in Figure 5.7 for both the meshes.

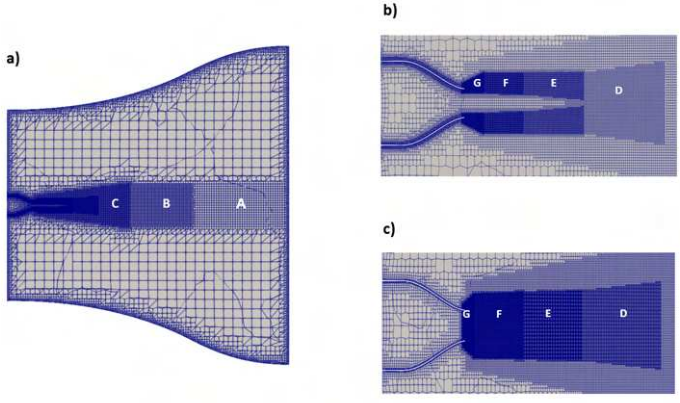

Figure 5.7: Domain mesh: meridional view (a), coarse mesh (b), fine mesh (c).

The mesh sensitivity analysis was carried out to assess the impact of a refinement around the potential core region on the numerical results. These ones involve both the aerodynamic shape of the exhaust jet and the far-field noise emissions. To this end, simulations of both the nozzles were performed on two meshes: a coarse one of around 33 million elements and a fine one of around 80 million elements. The computational effort was found to be nearly the same for both the SMC-000 and the SMC-001 nozzles, as differences in the geometry are concentrated just at the nozzle exit section. As it can be seen from Figure 5.7, a multi-region refinement strategy was pursued to cluster the elements close to the nozzle inner wall and in the shear layer region. As the simulations are expected to run into RANS mode close to solid walls, no particular requirements are needed except for a wall-normal mesh stretching to target y_+ classical values of RANS computations without wall-functions. Both the final meshes complies with this requirement, showing a maximum y_+ of around 20 at the nozzle exit where the highest flow velocity is expected in case of nozzle choking. Focusing on the shear layer region, the mesh was axially coarsened following the coalescence of turbulent eddies moving downstream of the nozzle exit. Such a degrading distribution of elements was achieved by defining in the *meshDict* file a sequence of topological entities, partially overlapping where different octree levels were set. The coarse mesh (see Figure 5.7) was refined just across the shear layer regions by specifying the thickness of three hollow cone regions. This thickness was chosen according to preliminary high-fidelity simulations aimed at just visualizing the jet spreading. On the other hand, the fine mesh was refined also in the potential jet region by replacing the hollow cone with a cylindrical body of influence. Details about the axial extension of each mesh region, the element dimensions and the corresponding octree level are summarized in Tables 5.3-5.4 for both the meshes. It is worth noting than the first octree level was skipped, thus the cell size of the coarsest level was set to 76.8 mm.

From the tables above it can be observed that the finest octree level is able to theoretically capture turbulent perturbations with a wavelength greater than 0.3 mm. Taking into account that spatial aliasing is prevented if at least 8-10 points per wavelength are retained [72], the actual cut-off wavelength due to mesh sizing is approximately 2.5 mm which corresponds to a maximum

Reg.	Shape	Length [D_e]	Cell size [mm]	Octree
A	cylinder	15	19.2	2
B	cylinder	10	9.6	3
C	cone	15	4.8	4
D	cone	4	2.4	5
E	hollow cone	3	1.2	6
F	hollow cone	2	0.6	7
G	hollow cone	1	0.3	8

Table 5.3: Regions and refinement levels of the coarse mesh.

Reg.	Shape	Length [D_e]	Cell size [mm]	Octree
A	cylinder	15	19.2	2
B	cylinder	10	9.6	3
C	cone	15	4.8	4
D	cone	4	2.4	5
E	cylinder	3	1.2	6
F	cylinder	2	0.6	7
G	cylinder	1	0.3	8

Table 5.4: Regions and refinement levels of the fine mesh.

resolved frequency of around 135 kHz. However, this is true only for an axial length equal to 1 D_e downstream of the nozzle exit section and across the shear layer region, as the mesh is then coarsened doubling the element sizing. In addition, the actual cut-off filter depends also on the choice of the numerical schemes used to discretize the Navier-Stokes equations so that highly dissipative setups are expected to produce poor quality data in the high-frequency range of the broadband noise spectrum.

Another important aspect is the very modest refinement of the potential core region of the coarse mesh: such a poor refinement was decided in order to keep the computational cost of the simulations quite low. Namely, it was supposed that the major contribution to the overall noise would have come from the shear layer perturbations, although this assumption was then disproved by the results. However, running scale-resolved simulations on a lighter mesh always provides quick information on the overall quality of the mesh. For these reasons, the cell sizing on the potential jet core was set to around 4.5 mm which led to a maximum resolved frequency of just 9 kHz considering the eight point per wavelength constraint. This clearly means that a finer meshing of the jet core is desirable to augment the resolution of far field noise spectra in the higher frequency range. Finally, further mesh coarsening was enforced also in the outer domain regions, as the computation of the far field noise through the FWH analogy is not based on a CFD mesh, thus allowing for mesh elements save far from the exhaust jet.

5.3.2 Numerical setup

Operative conditions for both the nozzles are referred to set-point 7 of the experimental campaign of Tanna [115, 116] on the SMC nozzle family. The jet flow properties at set-point 7 are listed in Table 5.5. From Table 5.5 it can be noted that set-point 7 is consistent with a cold jet flow, as the exhaust jet temperature T_j is lower than the ambient temperature T_∞. Although this is not realistic for a take-off condition, the choked flow ($M_j \approx 1$) is well representative of the loudest operative point of the nozzle. Thus, under an acoustic perspective, set-point 7 represents an attractive benchmark for the low noise design of the engine nozzle.

Acoustic Mach Number U_j/c_∞	0.9
Jet Mach Number U_j/c_j	0.985
Reynolds Number Re_j	1M
Temperature Ratio T_j/T_∞	0.835
Pressure Ratio P_0/P_∞	1.861

Table 5.5: Opertive conditions at set-point 7 from [115].

With regard to the numerical setup, the DDES computations were run using the *sonicFoam* solver for transient and compressible simulations of high speed flows. The latter still employs the pressure-based PIMPLE algorithm with a correction term to account for the hyperbolic characteristic of the Navier-Stokes equations in case of supersonic flows. Furthermore, the choice of a pressure-based solver instead of a density-based one was dictated by the need for preserving a high accuracy of the numerical discretization. More precisely, some preliminary investigations were carried out by using the density-based *rhoCentralFoam* solver embedding the flux splitting algorithm of Kurganov and Tadmor [143]. The latter was discarded as the usage of TVD schemes for flux reconstruction leads to a smoothing of the velocity gradients across the jet shear layer and thus it is not recommended for scale-resolved simulations of turbulent flows.

The two coarse DDES were initialized from steady-state RANS results of the jet flow while the DDES on the fine meshes were started from the final solution of the coarse ones. The SMC-000 simulations were run for around 110 convective time units ($CTU = D_e/U_j$) to purge the initial RANS solution, allowing for the development of a scale-resolved shear layer. Due to time limitations, a total simulation time of 80 CTU and 40 CTU was spent for the coarse and the fine DDES of the SMC-001 nozzle.

However, this simulation time has been considered sufficient for an acceptable convergence of the DDES, as their initialization were provided from well convergent high-fidelity solutions. Finally, the acoustic probing of the DDES flow field was enabled to produce noise spectra through the FWH analogy. Far-field pressure acquisitions were reproduced in the OpenFOAM framework by positioning pressure monitor points at a radial distance of 100 D_e downstream of the exit section, accordingly with the experimental measurements of Tanna [115]. An angular spacing of 15 degrees was considered when placing the virtual microphones on a 150° wide arc (the 0° direction is aligned with the jet axis). The *commonSettings* file of the *libAcoustics* library was modified to sample the noise sources every 128 simulation time-steps. As the time-step was set to 100 ns for stability and convergence reasons, from the chosen sampling rate an upper frequency of 78 kHz was determined. Signal analysis was then performed windowing the far-field pressure every 4096 time-steps (i.e., window width $\approx$ 0.4 ms) and taking the Discrete Fourier Transform (DFT) on it. The acoustic probing lasted other 170 CTU, producing a total amount of 73 FFT samples. From these considerations it follows that the lowest frequency of the spectrum resolved by the FWH analogy was around 30 Hz. However, considering that at least 8-10 points should be used for the temporal fit of a numerical signal without aliasing, it can be concluded that the SPL estimations in the frequency range from 30 to 300 Hz could be quite inaccurate. To further increase the noise spectrum accuracy at the very low frequencies, a longer total simulation time would have been necessary. More in detail, the round and the chevron simulations completed the total 280 CTU running for around ten days on 1536 CPU cores on the Advanced Research Computing (ARC) cluster owned by the University of Oxford. On the other hand, limitations on the maximum available computational resources were to be faced, taking into account also the time each calculation was queued on the cluster. For all these reasons, it was impossible to further improve the quality of the results for frequencies lower than 500 Hz.

Concerning the numerical schemes adopted for the DDES, second order cell-centered spatial and temporal schemes were prescribed for all terms of the Navier-Stokes equations. Some trials with higher order schemes were also attempted but the numerical setup was turned to be too unstable to successfully converge. This was probably due to the octree grid strategy which is likely to introduce numerical stiffness when combined with a higher order setup, especially in case of complex flows. The PIMPLE algorithm was set to run one inner pressure correction loop while looping three times on the outer pressure-velocity coupling. An additional non-orthogonal correction of the fluxes was enabled as simulations were run on a non-structured mesh. Finally, a $k-\omega$ turbulence modelling was selected for the DDES approach. This choice was motivated by the laminar inflow and the rather coarse mesh refinement on the nozzle inner walls that would have made useless to run into the more time-consuming IDDES mode. Nevertheless, the $k-\omega$ RANS model was preferred to the Spalart-Allmaras one due to its higher reliability for internal flow applications.

Focusing on boundary conditions, the entire domain was confined by five boundaries, as depicted in Figure 5.8: the nozzle inlet, the co-flow inlet, the outlet, the revolving lateral side, and the nozzle walls. It is worth mentioning that for the present simulations, no co-flow was included into the numerical setup as a take-off condition was simulated. However, the patch splitting of Figure 5.8 was thought to facilitate the boundary condition set-

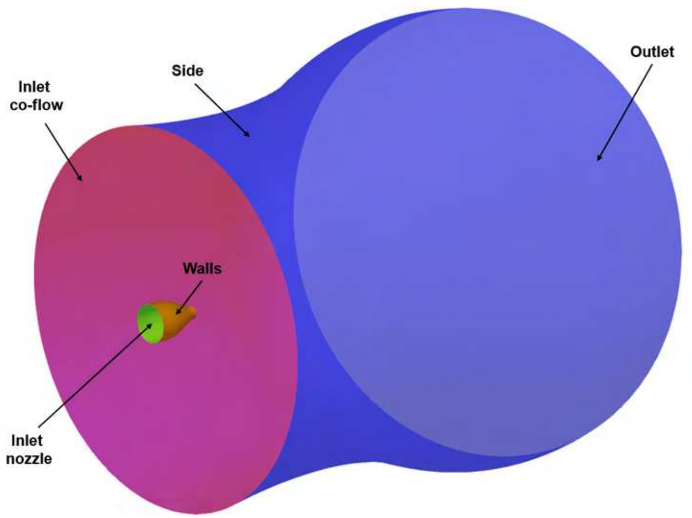

Figure 5.8: Boundary patches of numerical domain.

ting when simulating any other operative point during the flight mission. To reproduce the flow conditions in Table 5.5, total pressure and temperature were specified at the nozzle inlet while ambient values were imposed on the other fluid boundaries. Neumann boundary conditions were set for pressure and temperature on the nozzle walls to recreate an adiabatic wall constraint. With regard to velocity, the OpenFOAM *pressureDirectedInletVelocity* boundary type was used to tell the solver to derive the velocity field from the pressure field at the nozzle inlet. Such a boundary condition enables also the specification of the inlet flow direction that in the present simulations was considered aligned with the jet axis. On all the other fluid boundaries, the *inletOutlet* boundary condition was chosen to extract the velocity field on them from the interior of the domain. This boundary type is well suited for unsteady simulations as it can also handle possible back-flow occurring on the boundary patch due to turbulent fluctuations. Finally, a turbulence intensity of 5% and a mixing length equal to 0.152 m (i.e., the nozzle inlet diameter) were prescribed at the nozzle inlet to provide a closure for the background RANS model.

Finally, a last aspect of the numerical setup was the selection and the placement of the permeable FWH surface for the acoustic analyses. Following the suggestions of Mendez [72], the FWH surface was accurately chosen to embrace all the noise sources coming from the shear layer perturbations lying in the refined mesh regions. A picture of the FWH surface with the background mesh is shown in Figure 5.9

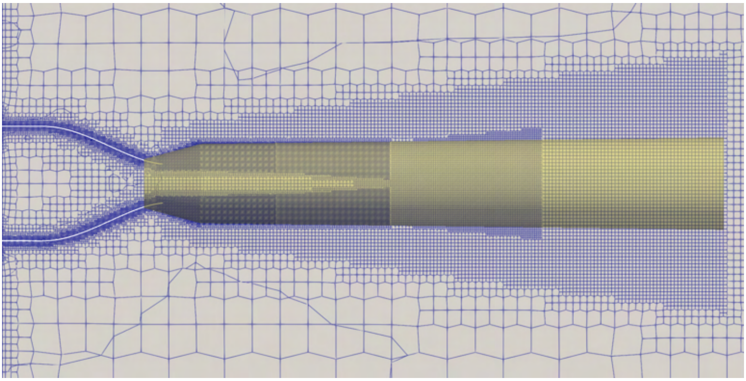

Figure 5.9: Placement of the FWH surface inside the numerical domain.

As depicted in Figure 5.9, the FWH surface is composed of a conical shell wrapping around the finest mesh region (zone G of Tables 5.3. 5.4), followed by a cylindrical annulus that extends up to the end of region C. Downstream of this threshold (15 D_e) the mesh is too coarse to provide significant information on turbulent structures, resulting in an unreliable estimation of noise emissions.

5.4 Aerodynamic results

In this section, numerical outcomes of the DDES simulations are discussed focusing on the characterization of the jet flow produced by the round and the chevron nozzle configurations. Firstly the effect of refining the mesh in the core region is shown, restricting the mesh sensitivity analysis to the SMC-000 nozzle only. This choice was motivated by the fact that the fine meshes have been created using the same settings on both the nozzle, thus no influence of the nozzle geometry is expected on the results. For the same reason, under an aerodynamic perspective, the observations about the refinement of the jet core will generally hold for both the nozzles. Then, comparisons between the round and the chevron jets are made to highlight how the selected saw-tooth shaping acts on the jet features of the baseline nozzle.

In Figure 5.10, the time-averaged decay trend of the non-dimensional jet velocity along the center-line and the lip-line of the exit section is shown. The axial distance from the exit section is scaled by the nozzle exit diameter (D_e) while the jet velocity by the inviscid jet velocity at the nozzle exit (U_j). The DDES results on the coarse (red curve) and the fine (blue curve) meshes are compared to the benchmark of Tanna experiments [115] to understand the margin of accuracy improvement coming from the mesh refinement. From the top graph of Figure 5.10 it can be noted that the experimental trend of the jet decay is correctly predicted on both the meshes, although running the DDES on the coarse mesh results in a shorter extension of the potential

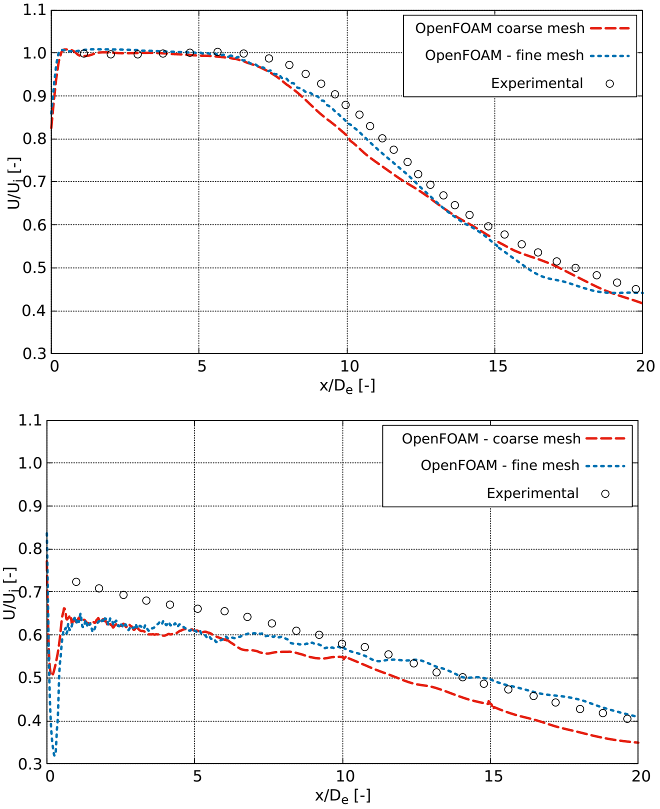

Figure 5.10: Jet velocity axial decay along the centerline (top) and the lip line (bottom)

region outlined by the threshold $U/U_j = 1$. The red curve starts to deviate from the experiments at around x = 5 D_e while the extension of the potential core is prolonged up to around $7D_e$ with the fine mesh. Moreover, major differences between the coarse mesh results and the experiments of Tanna are visible in terms of center-line decay in the region between x = 5 D_e to x = 15 D_e where the fine mesh better approaches the experimental levels, nearly halving the gap on the ordinate axis. Similar considerations can be made on the lip-line decay, although the experimental trend for the first 5 D_e is not matched by none of the two DDES. This suggests that further mesh refined will be probably needed to properly described the turbulent features responsible for the momentum exchange at nozzle exit section. On the other hand, the fine mesh helps in predicting the lip-line velocity decay far from the nozzle ($x > 10D_e$) where the numerical curve just lies on the experimental dots. This evidence comes from the augmented resolution of the eddies that coalesce moving downstream of the exit section. More specifically, the lip line velocity is even more influenced by the contribution of the turbulent eddies from the center-line region which is now populated by vortical structures as the potential core has collapsed. Thus, a more accurate detection of such features leads to a better representation of the lip-line jet velocity, explaining the closer numerical-to-experimental agreement visible in the bottom graph of Figure 5.10.

To further prove this fact, it can be looked at Figure 5.11 where the radial shape of the jet is shown for an axial distance of 1 D_e (top) and 10 D_e (bottom) downstream of the nozzle exit section. It can be easily deduced that the jet shape is almost mesh independent at x $= 1D_e$ while a marked under-prediction of the peak velocity (around the 12 % with respect to the experimental peak value) is evident on the coarse mesh at x $= 10D_e$. This mismatch is almost completely recovered with the fine mesh which leads to an estimation of the non-dimensional peak velocity of 0.87 compared to the 0.9 experimental level. From the top graph of Figure 5.11 it can be also observed that non-zero values of the jet velocity are predicted for a radial coordinate ranging from around -0.7 D_e to 0.7 D_e. This means that the

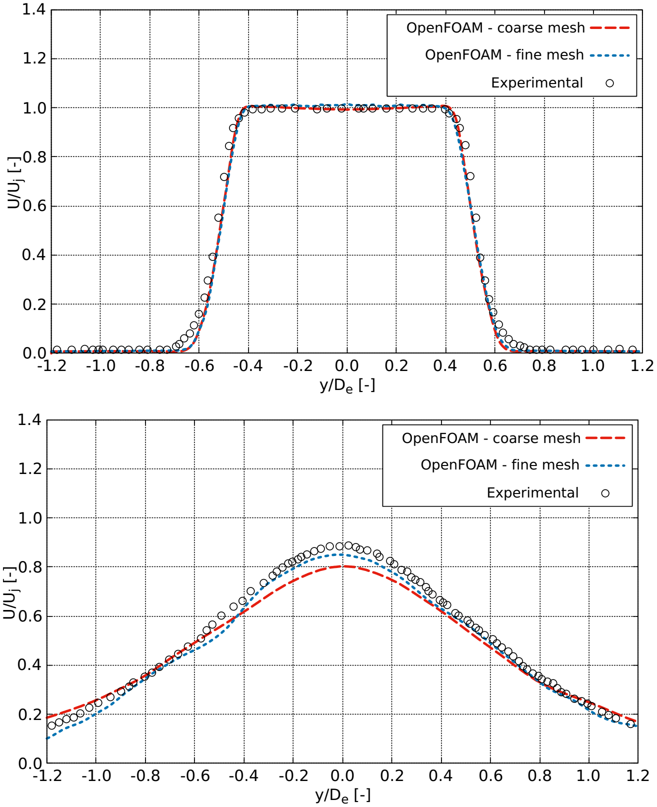

Figure 5.11: Radial jet shape at x $= 1D_e$ (top) and x$= 10D_e$ (bottom)

radial spreading of the shear layer is very low close to the nozzle exit, suggesting that the jet shape is basically unaffected by the refinement level of the jet core region. On the other hand, the width of the bell-shape radial profile increases with the axial distance and non-zero values of the jet velocity are predicted to cover a range of more than $2.4D_e$ at an axial distance equal to $10D_e$. Here the velocity peak is lower than 1, meaning that no potential regions are present at this axial distance. At the same time, the mesh dependency of the jet shape implies that the jet spreading is large enough to involve also the center-line area, making the mesh refinement absolutely necessary for an accurate prediction of the axial jet decay.

Focusing now on the effect of the chevron shaping, comparisons between the jet velocity decay and the radial jet profile are made in the following paragraph. As before, the decay has been evaluated along the center-line and the lip-line for the first 20 diameters downstream of the nozzle exit section since the mesh becomes too coarse from this point on. With regard to the lip-line comparisons, the apex lip height has been considered for the SMC-001 chevron nozzle. On the other hand, the radial jet shape has been compared at four stations (i.e., x $= 1D_e$, x $= 3D_e$, x $= 5D_e$, x $= 10D_e$) highlighting also the differences in the jet features on the apex and the notch meridional views.

Looking at Figure 5.12, it can be observed that the potential core region is shorter for the chevron nozzle if compared to the round one. This is well highlighted in the top graph of Figure 5.12 where the steeper decay trend (green curve) of the SMC-001 jet suggests an enhanced turbulent mixing across the shear layers. As a consequence, the jet core outlined by the threshold $U/U_j = 1$ is shrunk, reducing the axial length of the potential region from 7 D_e to less than 5 D_e. This aspect is also clearly displayed in Figure 5.13 where it can be observed that the area of the time-averaged contour $U/U_j = 1$ (dark red area) is smaller for the chevron jet compared to the one of the baseline geometry.

A side effect of the shrinkage of the chevron jet core is given by the lip-line decay shown in the bottom graph of Figure 5.12. Here, it can be seen that the non-dimensional jet velocity across

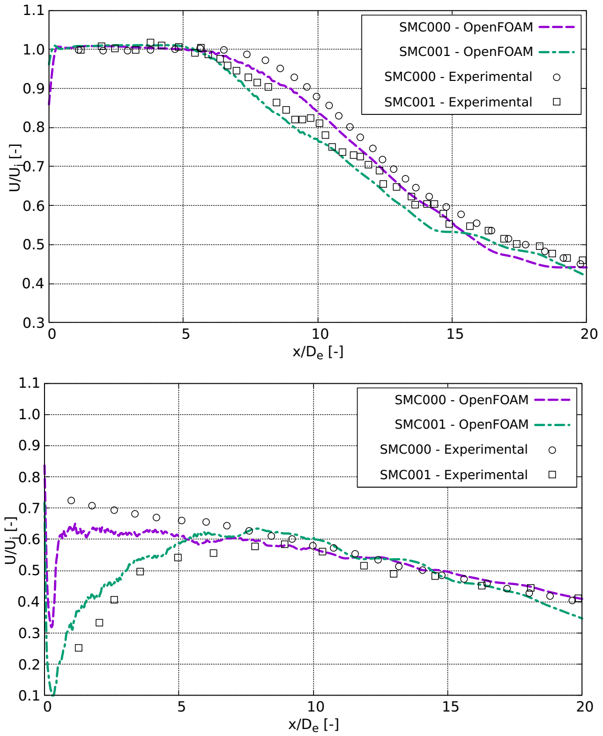

Figure 5.12: Comparison between jet velocity axial decay for SMC-000 and SMC-001 nozzles: center-line (top), lip-line (bottom)

the lip line of the chevron nozzle shows a maximum at around 9 D_e, while it keeps decreasing on the baseline geometry. Then, both the decay trends (see the green and the violet curves) becomes similar for $x > 10D_e$ suggesting that the turbulent eddies in the shear layer grow quite in the same way far from the nozzle exit section, regardless of the nozzle geometry. On the other hand, the very low velocity of the chevron jet along the lip line near the nozzle exit is coherent with intense transverse velocity

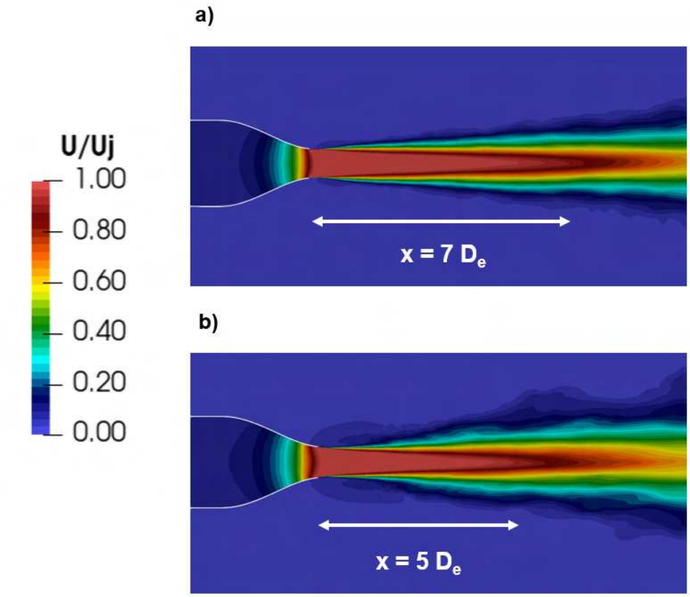

Figure 5.13: Potential region axial length: SMC-000 (a), SMC-001 (b).

fluctuations promoting the radial exchange of momentum across the shear layers. The magnitude of these effects depends on the axial length of the chevron apexes which is directly linked to the amount of the jet under-expansion at the notch exit section. In other words, in a chevron nozzle the jet expansion is not fully confined by the nozzle wall for the entire axial length, and it is completed outside the nozzle just downstream of the notch circumference. As a results, a star-like jet cross section is produced and a wider radial spreading of the chevron jet is observed, as illustrated by Figures 5.14, 5.15.

The excellent agreement between the DDES and the experimental observations can be also verified in terms of radial profiles

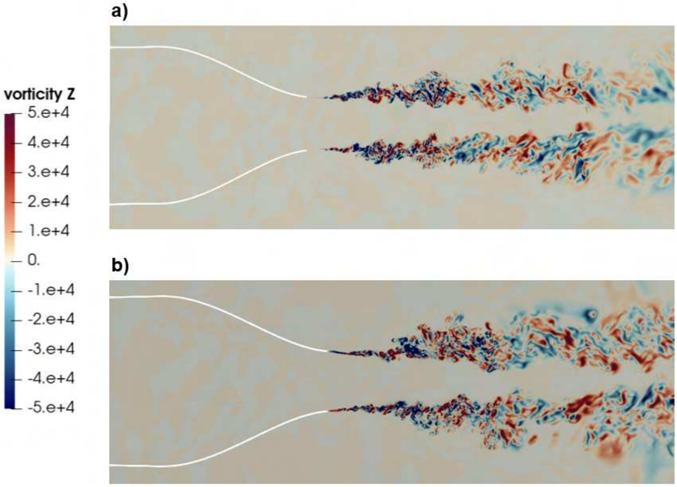

Figure 5.14: Radial vorticity contours: SMC-000 (a), SMC-001 (b).

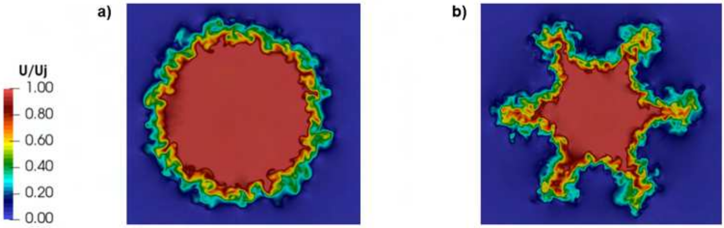

Figure 5.15: Axial jet cross section at x = $1D_e$: SMC-000 (a), SMC-001 (b)

at different sections downstream of the nozzles, as shown in Figures 5.16, 5.17, 5.18, 5.19.

The time averaged non-dimensional velocity U/U_j is plotted against the radial the direction to highlight the strength of the mixing mechanism when comparing the baseline and the chevron

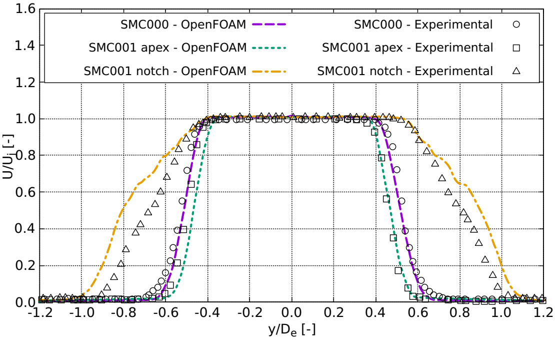

Figure 5.16: Radial jet profile at x = $1D_e$: violet = SMC-000, green = SMC-001 apex section, orange = SMC-001 notch section

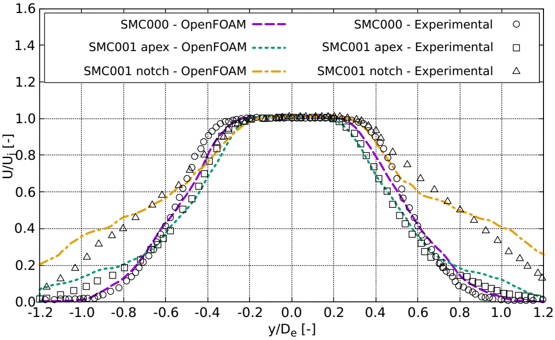

Figure 5.17: Radial jet profile at x = $3D_e$: violet = SMC-000, green = SMC-001 apex section, orange = SMC-001 notch section

nozzle jets. From all figures it can be stated that the quality of the numerical-to-experimental correlation is high, as both the peak levels and the radial width of the bell curves are well captured by the numerical simulations. Furthermore, a significant difference between the chevron nozzle radial profiles on the apex and the notch slices is well visible up to x = 3 D_e. In addi-

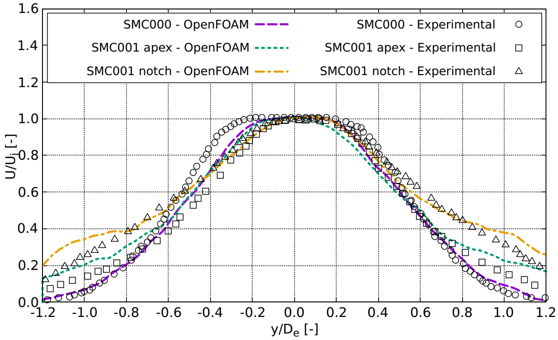

Figure 5.18: Radial jet profile at x $= 5D_e$: violet = SMC-000, green = SMC-001 apex section, orange = SMC-001 notch section

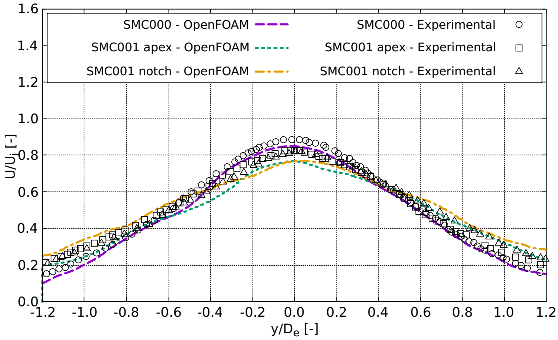

Figure 5.19: Radial jet profile at x $= 10D_e$: violet = SMC-000, green = SMC-001 apex section, orange = SMC-001 notch section

tion, it can be noted that the extent of the potential region is shortened since the radial profile peaks become even narrower reducing the radial range of the threshold $U/U_j = 1$. Then, for farther distances, the apex and the notch profiles tend to collapse onto a unique profile, nearly overlapping one another at x = 10 D_e where the non-dimensional velocity peak is less than

1. This characteristic of the chevron jet is again related to the incomplete expansion that generates the star-like jet pattern. As visible in Figure 5.20, the star-like shape of the chevron jet progressively loses its sharp outline as a result of the increasing influence of the fully developed region of the shear layer. At the same time, Figures from 5.16 to 5.19 show that on the apex slice, the chevron jet behaves very similar to the round jet. However, the effect of the chevron penetration is always visible at each axial location, as demonstrated by the narrower peak regions and the higher levels of U/U_j in the ranges $-1.2 < y/D_e < -0.8$ and $0.8 < y/D_e < 1.2$.

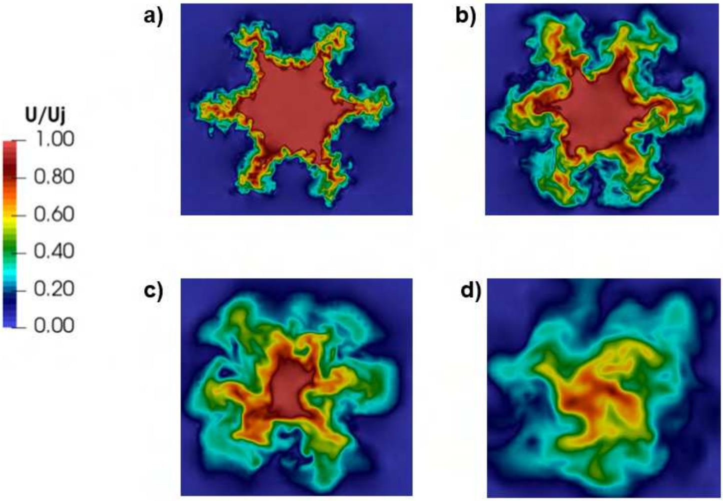

Figure 5.20: Star-like shape of SMC-001 jet at different axial locations: x = 1 D_e (a), x = 3 D_e (b), x = 5 D_e (c), x = 10 D_e (d)

5.5 Acoustic results

This last section follows the same structure of the previous one, but with an emphasis on the acoustic signature of the nozzles jet flow. The mesh sensitivity analysis was carried out on the far field spectra of both the nozzles as many aspects concur to the derivation of the noise spectra from the velocity fluctuations of the shear layers. Although keeping the same mesh strategy on both the nozzles should ensure the same accuracy when resolving the jet shear layers, some questions have arisen on how the modification of the potential core in the chevron nozzle simulations would have affected the inviscid noise sources responsible for the overall broadband emissions. Moreover, it could not be a priori stated that noise spectra calculated through the FWH analogy would have been affected the same by the mesh refinement. More in detail, as the CFD input for the FWH calculation changed depending on the nozzle geometry, it had to be demonstrated whether keeping the same mesh refinement would have produced similar acoustic results. To investigate the mesh influence on the noise results, narrow-band spectra have been drawn at the polar positions $\theta = 60^o$ and $\theta = 120^o$ as shown in Figures 5.21, 5.22 for the SMC-000 and the SMC-001 nozzles respectively.

It can be noted that in both the cases and for both the polar locations, the blue spectrum obtained with the fine mesh well covers the experimental black dots on the entire Strouhal range (the maximum Strouhal number on the abscissa was truncated to $St = 4$ which corresponds to the upper frequency limit of the audible range). On the contrary, without the core region refinement, a large under-prediction of noise levels at the higher frequencies is visible on the red spectrum resulting from the coarse

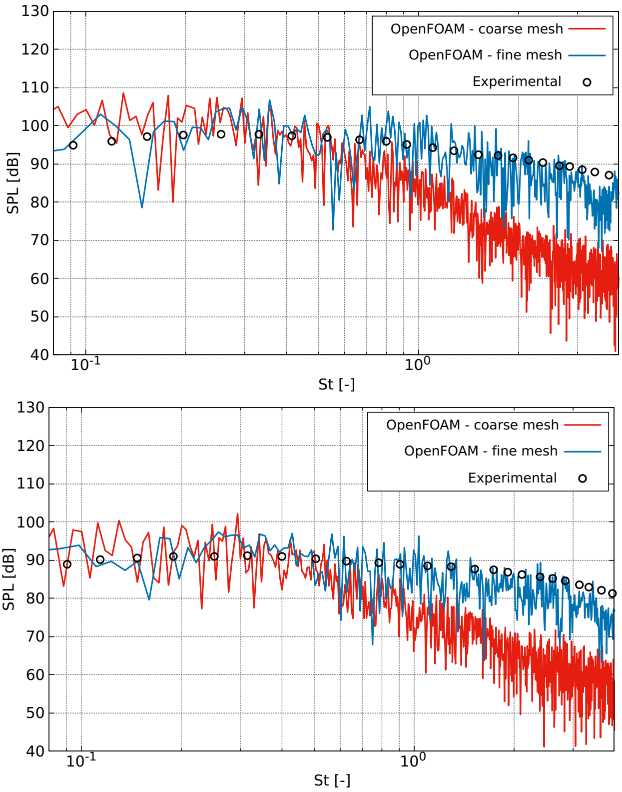

Figure 5.21: Mesh sensitivity on far field noise spectra at polar angle $\theta = 60°$ (top) and $\theta = 120°$ (bottom), SMC000 nozzle

mesh. More specifically, the coarse and the fine spectra start to diverge from around $St > 1$ suggesting that this is the cut-off frequency of the coarse mesh. In terms of audible frequency, this threshold correspond to around 6000 Hz, meaning that all those noise emissions with a frequency higher than 6000 Hz cannot be captured on the coarse mesh. This is clearly due to the too large octree sizing of the coarse mesh in the potential region

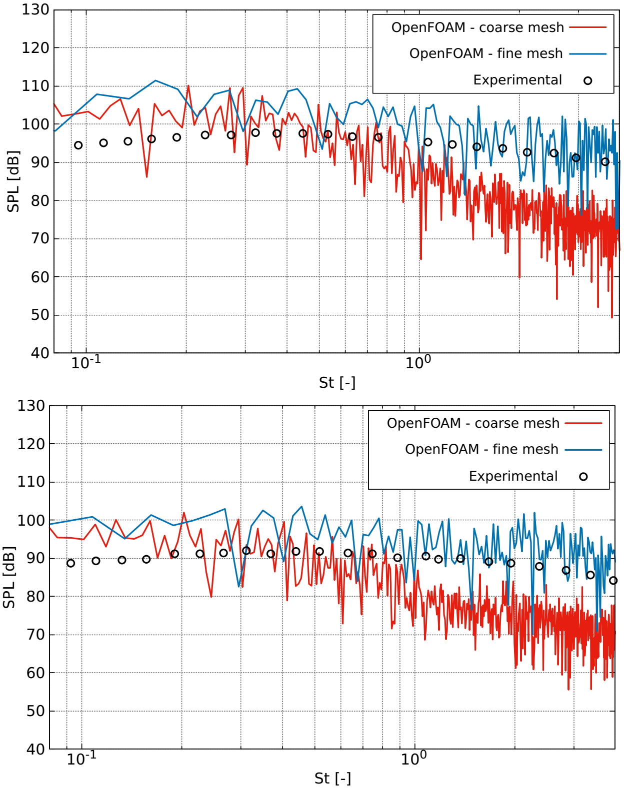

Figure 5.22: Mesh sensitivity on far field noise spectra at polar angle $\theta = 60°$ (top) and $\theta = 120°$ (bottom), SMC001 nozzle

which damps out all the high-frequency perturbations generated in the shear layers close to the nozzle exit section. On the other hand, restricting the analysis to the low-frequency range (i.e., below 6000 Hz), no significant differences between the spectra are noted and they both well agree with experimental SPLs. This is definitely true for the round nozzle, while some discrepancies in the chevron nozzle spectra are present on the fine mesh. However, it should be reminded that the fine mesh simulation on the SMC-001 nozzle ran for just 40 CTU, which is around 0.006 seconds of physical time. Hence, this cannot be considered enough time to determine a reliable Fourier transform of the very low noise emissions. Considering that at least ten samples are needed for a good temporal resolution of a time-varying signal, the first frequencies that are not affected by aliasing are the ones greater than 1800 Hz (i.e., $St \approx 0.3$). This fact is further proved by the rather smooth low frequency range of the blue curve in Figure 5.22 which is consistent with an under-resolved portion of the noise spectrum.

Moving now to the comparisons between the baseline SMC-000 and the chevron SMC-001 nozzles, in the rest of the chapter the far-field narrow-band noise spectra are plotted against the experimental benchmark for polar angles of 45°, 60°, 90° and 120°, as shown in Figures from 5.23 to 5.26. From the previous discussion about the acoustic mesh sensitivity, it follows that all the spectra are here referred to the simulations performed on the fine mesh on both the nozzles.

From all the four figures, it can be said that the numerical results are in a good agreement with the experimental data as the noise spectra are well reproduced at all the angles correctly locating the noise peak and the spectrum trend. Furthermore, it can be seen the chevron effect on the high frequencies of the spectrum as higher SPLs are predicted from $St > 1$ at any polar angle under investigation. This is evident also on the experimental spectra but with a lower SPL increase which is also slightly shifted at larger Strouhal numbers (i.e., $St > 1.5 - 2$). Another interesting characteristic visible from the spectra is the directional noise emitted by both the nozzles. More specifically, the noise peak which occurs at $St \approx 0.5$ on both the round and the

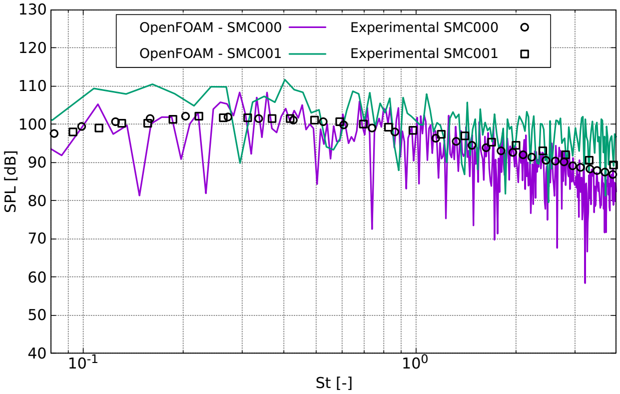

Figure 5.23: Far field noise spectra for SMC000 (violet) and SMC001 (green) at $\theta = 45^o$

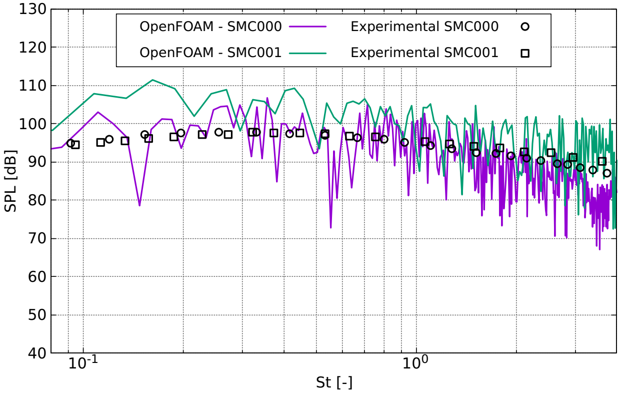

Figure 5.24: Far field noise spectra for SMC000 (violet) and SMC001 (green) at $\theta = 60^o$

chevron spectra is progressively decreasing falling from 102 dB at $\theta = 45°$ down to 91 dB at $\theta = 120°$. Thus, regardless of the nozzle layout, broadband noise from exhaust jets is mostly radiated rearward. This is a consequence of the anisotropy of the larger eddies which are mainly convected along the axial di-

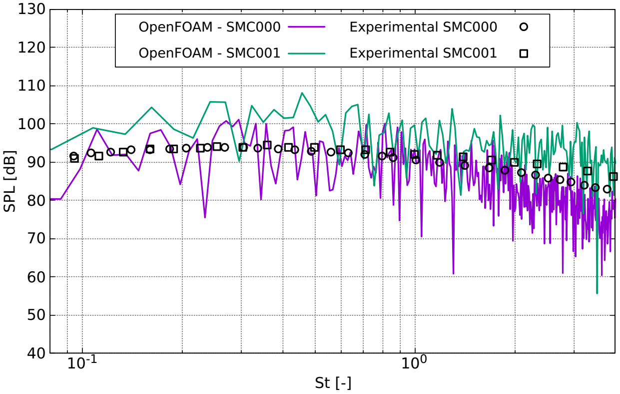

Figure 5.25: Far field noise spectra for SMC000 (violet) and SMC001 (green) at $\theta = 90^o$

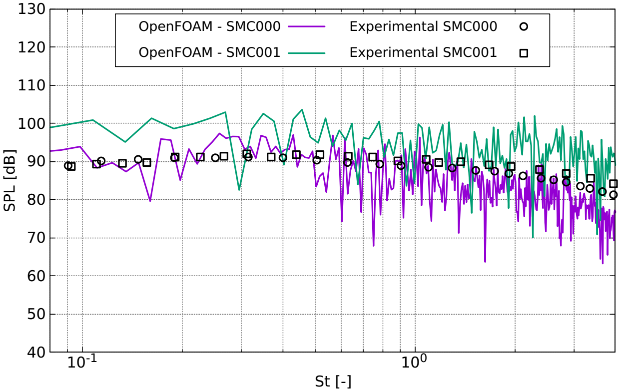

Figure 5.26: Far field noise spectra for SMC000 (violet) and SMC001 (green) at $\theta = 120^o$

rection by the mean jet velocity. Another conclusion that can be retrieved from the spectral analysis is that the SMC-001 nozzle is not well designed to tackle the low-to-medium broadband noise, as almost no attenuation on this portion of the spectrum is performed. This aspect is present on both the numerical and the experimental spectra where almost identical spectra are predicted for the SMC-000 and the SMC-001 jets from $St = 0.1$ to $St = 1.5$. Major discrepancies are also visible on the DDES results as noise levels of the chevron nozzle in this range are about 10 dB above the baseline ones. However, this evidence can be motivated by the poor convergence of the low frequency range of the SMC-001 spectra due to the insufficient simulation time. Nonetheless, it can be reasonably stated that the SMC-001 is not able to provide an efficient shifting of the broadband noise to higher frequencies, as the noise peak occurs at the same Strouhal number of the baseline configuration at all the polar locations. A possible explanation of this behaviour lies in the very little teeth penetration of the chevron end (i.e., ≈ 1 mm only) which implies a too modest vortex strength. In other words, the chevron teeth of the SMC-001 layout are carved without a sufficient bending in the radial direction, thus making the exhaust jet almost insensitive to the nozzle exit section geometry.

6

Conclusions

This thesis describes how the high-fidelity CFD applied to turbofan engines components can be considered a powerful tool to properly design noise absorbing devices to tackle the aeronautical noise. Two different low noise devices commonly used in aviation have been studied, focusing on the characterization of the performance of acoustic liners and chevron nozzles under different operating conditions.

With regard to the acoustic liner activity, the proposed LES has been validated on a single degree of freedom resonator mock up, showing a close matching between the LES results, the experiments of Jones [102] and the theoretical model of Hersh [88] in terms of acoustic impedance prediction. The acoustic liner response has been assessed by varying the excitation frequency and amplitude as well as the Mach number of a laminar grazing flow. Some discrepancies about the resistance evaluation have been reported when analyzing the impact of the grazing flow on the acoustic impedance. According to some literature works [98, 99], these can be addressed to the imposed laminar inflow of the LES which is actually turbulent in both the experiments and the analytical modelling assumptions. Although the author is aware of such a simplified hypothesis, the imposotion of a laminar inflow has drastically reduced the complexity of the numerical setup and the simulation duration. More precisely, in the OpenFOAM environment no boundary condition can handle an acoustic and a velocity inlet at the same time, meaning that acoustic wave and synthetic turbulence cannot be applied simultaneously. Furthermore, digital filter methods [144, 145] or synthetic turbulence boundary conditions [146] lead to too long lasting simulations, partially corrupting the robustness of the numerical setup. A possible workaround to implement the turbulent boundary layer over the acoustic liner could be the simulation of two adjacent resonators so that the pulsating jets of the first system act as a trigger of the boundary layer transition, still keeping a laminar inflow setup. A similar effect can be achieved by carving a rib on the fluid domain to promote the boundary layer transition on the liner surface. On the other hand, the rib might reflect part of the travelling acoustic wave, thus polluting the in-situ impedance evaluation. Despite this lack, the LES has been successfully applied for the validation of an in-house analytical model aimed at extending the theory of Hersh [88] to innovative multi-degree-of-freedom liners. The model has been validated for a three-degree-of-freedom resonator under the effect of the excitation frequency and the grazing flow.

On the other side, the aeroacoustic investigation of noise emission from round and chevron nozzles has been firstly based on the definition of a proper numerical setup to perform Detached Eddy Simulations (DDES) in the OpenFOAM environment. In this context the need for a full 360 degrees model of the nozzle has emerged, since no flow periodicity can be assumed when running high-fidelity simulations also on periodic geometries. As a consequence, the computational effort of running such full model simulations has drastically grown up, requiring large parallel clusters to accomplish the task. Also for this reason, a mesh sensitivity analysis has been carried out to understand whether different refinement levels of the jet region might return similar results. Ideally, it has been thought that the mesh on the potential region of the exhaust jet could be coarsened as broadband emissions were supposed to be originated mainly in the shear layers. However, looking both at the jet shape resolved by the DDES and at the far-field spectra, it has been demonstrated that a fine mesh is needed also in the jet core region to achieve a closer agreement between numerical and experimental results. In addition, focusing on the far-field comparison between noise spectra of round and chevron layouts, it has been highlighted how to design the chevron pattern for effectively tackling the broadband noise emissions. Due to the limited time spent for this activity, many future works can be thought to further extend the jet noise investigation from exhaust nozzles. Some interesting projects may involve the study of more than a single chevron nozzle pattern to compare the acoustic performance of different saw-tooth designs. In this context, hot flow simulations can be also run to provide a deeper insight on noise emissions investigating a more realistic working condition of aeronautical nozzles. Finally, the DDES approach may be replaced with a wall modelled Large Eddy Simulation (WMLES) formulation to test if a fully scale-resolved characterization of the boundary layer on the inner wall of the nozzle might influence the far-field noise estimations.

Bibliography

[1] Oct. 2022. URL: `https://www.eurocontrol.int`.

[2] Stéphane Moreau. "Turbomachinery Noise Predictions: Present and Future". In: *Acoustics* 1.1 (2019), pp. 92–116. ISSN: 2624-599X. DOI: `10.3390/acoustics1010008`.

[3] Attila Balázs Nagy, Jan Delfs, and Gareth J. Bennett. "Aeroacoustics research in Europe: The CEAS-ASC report on 2020 & 2021 highlights". In: *Journal of Sound and Vibration* 534 (2022), p. 117002. ISSN: 0022-460X. DOI: `https://doi.org/10.1016/j.jsv.2022.117002`.

[4] ICAO Annex. "16, vol. 1, aircraft noise". In: *International Civil Aviation Organization, Montreal, Canada* (2008).

[5] Axel Krein and Gareth Williams. "Flightpath 2050: Europe's vision for aeronautics". In: *Sixth European Aeronautics Days, Madrid, Spain, 30 March-1 April*. 2011, p. 30.

[6] Meelan M Choudhari et al. *Aeroacoustic experiments in the NASA Langley low-turbulence pressure tunnel.* Tech. rep. 2002.

[7] Craig Streett et al. "Aerodynamic noise reduction for high-lift devices on a swept wing model". In: *44th AIAA aerospace sciences meeting and exhibit.* 2006, p. 212.

[8] Taro Imamura et al. "Designing of slat cove filler as a noise reduction device for leading-edge slat". In: *13th AIAA/CEAS Aeroacoustics Conference (28th AIAA Aeroacoustics Conference).* 2007, p. 3473.

[9] William D Scholten et al. "Development and analysis-driven optimization of superelastic slat-cove fillers for airframe noise reduction". In: *AIAA Journal* 54.3 (2016), pp. 1078–1094.

[10] Roberto Merino Martinez et al. "Comparing flyover noise measurements to full-scale nose landing gear wind tunnel experiments for regional aircraft". In: *23rd AIAA/CEAS aeroacoustics conference.* 2017, p. 3006.

[11] Petr Eret, John Kennedy, and Gareth J Bennett. "Effect of noise reducing components on nose landing gear stability for a mid-size aircraft coupled with vortex shedding and freeplay". In: *Journal of Sound and Vibration* 354 (2015), pp. 91–103.

[12] Eleonora Neri, John Kennedy, and Gareth J Bennett. "Characterization of low noise technologies applied to a full scale fuselage mounted nose landing gear". In: *Noise Control and Acoustics Division Conference.* Vol. 56819. American Society of Mechanical Engineers. 2015, V001T01A005.

[13] Gareth J Bennett, Eleonora Neri, and John Kennedy. “Noise characterization of a full-scale nose landing gear”. In: *Journal of Aircraft* 55.6 (2018), pp. 2476–2490.

[14] Kyle E Niemeyer and Chih-Jen Sung. “Recent progress and challenges in exploiting graphics processors in computational fluid dynamics”. In: *The Journal of Supercomputing* 67 (2014), pp. 528–564.

[15] Julien Thibault and Inanc Senocak. “CUDA implementation of a Navier-Stokes solver on multi-GPU desktop platforms for incompressible flows”. In: *47th AIAA aerospace sciences meeting including the new horizons forum and aerospace exposition.* 2009, p. 758.

[16] Aaron F Shinn and Surya Pratap Vanka. “Implementation of a semi-implicit pressure-based multigrid fluid flow algorithm on a graphics processing unit”. In: *ASME International Mechanical Engineering Congress and Exposition.* Vol. 43864. 2009, pp. 125–133.

[17] Michael Griebel and Peter Zaspel. “A multi-GPU accelerated solver for the three-dimensional two-phase incompressible Navier-Stokes equations”. In: *Computer Science-Research and Development* 25 (2010), pp. 65–73.

[18] Yu Shi et al. “Accelerating multi-dimensional combustion simulations using GPU and hybrid explicit/implicit ODE integration”. In: *Combustion and Flame* 159.7 (2012), pp. 2388–2397.

[19] Stephen B Pope and Stephen B Pope. *Turbulent flows.* Cambridge university press, 2000.

[20] Lewis Fry Richardson. *Weather prediction by numerical process.* University Press, 1922.

[21] Andrey Nikolaevich Kolmogorov. “The local structure of turbulence in incompressible viscous fluid for very large Reynolds number”. In: *Dokl. Akad. Nauk. SSSR*. Vol. 30. 1941, pp. 301–303.

[22] Patrick W McDonald. *The computation of transonic flow through two-dimensional gas turbine cascades*. Vol. 79825. American Society of Mechanical Engineers, 1971.

[23] Robert MacCormack and Alvin Paullay. “Computational efficiency achieved by time splitting of finite difference operators”. In: *10th aerospace sciences meeting*. 1972, p. 154.

[24] Osborne Reynolds. “IV. On the dynamical theory of incompressible viscous fluids and the determination of the criterion”. In: *Philosophical transactions of the royal society of london.(a.)* 186 (1895), pp. 123–164.

[25] A Favre. “Statistical equations of turbulent gases”. In: *Problems of hydrodynamics and continuum mechanics* (1969), pp. 231–266.

[26] Joseph Boussinesq. *Theorie analytique de la chaleur: mise-en harmonie avec la thermodynamique et avec la theorie mecanique de la lumiere: Tome 2: Refroidissement et echauffement par rayonnement conductibilite des tiges, lames et masses cristallines courants de convection*. Gauthier-Villars Paris, 1903.

[27] Ludwig Prandtl. “7. Bericht über Untersuchungen zur ausgebildeten Turbulenz”. In: *ZAMM-Journal of Applied Mathematics and Mechanics/Zeitschrift für Angewandte Mathematik und Mechanik* 5.2 (1925), pp. 136–139.

[28] Edward R Van Driest. “On turbulent flow near a wall”. In: *Journal of the aeronautical sciences* 23.11 (1956), pp. 1007–1011.

[29] Francis H Clauser. “The turbulent boundary layer”. In: *Advances in applied mechanics* 4 (1956), pp. 1–51.

[30] W Mii Kays and RJ Moffat. “The behavior of transpired turbulent boundary layers”. In: *NASA STI/Recon Technical Report N* 75 (1975), p. 32383.

[31] Amo Smith, Tuncer Cebeci, and Douglas Aircraft Division. *Numerical solution of the turbulent-boundary-layer equations.* Douglas Aircraft Company, Douglas Aircraft Division, 1967.

[32] Barrett Baldwin and Harvard Lomax. “Thin-layer approximation and algebraic model for separated turbulentflows”. In: *16th aerospace sciences meeting.* 1978, p. 257.

[33] L Prandtl. “Ueber ein neues Formelsystem fur die ausgebildete Turbulenz. Nach. Ges. Wiss. Gottingen, Math”. In: *Phys. Kl* (1945), pp. 6–18.

[34] Philippe Spalart and Steven Allmaras. “A one-equation turbulence model for aerodynamic flows”. In: *30th aerospace sciences meeting and exhibit.* 1992, p. 439.

[35] Brian Edward Launder and Dudley Brian Spalding. “The numerical computation of turbulent flows”. In: *Numerical prediction of flow, heat transfer, turbulence and combustion.* Elsevier, 1983, pp. 96–116.

[36] David C Wilcox et al. *Turbulence modeling for CFD.* Vol. 2. DCW industries La Canada, CA, 1998.

[37] Florian R Menter. “Two-equation eddy-viscosity turbulence models for engineering applications”. In: *AIAA journal* 32.8 (1994), pp. 1598–1605.

[38] Robin B Langtry and Florian R Menter. “Correlation-based transition modeling for unstructured parallelized computational fluid dynamics codes”. In: *AIAA journal* 47.12 (2009), pp. 2894–2906.

[39] Brian Edward Launder, G Jr Reece, and W Rodi. “Progress in the development of a Reynolds-stress turbulence closure”. In: *Journal of fluid mechanics* 68.3 (1975), pp. 537–566.

[40] Charles G Speziale, Sutanu Sarkar, and Thomas B Gatski. “Modelling the pressure–strain correlation of turbulence: an invariant dynamical systems approach”. In: *Journal of fluid mechanics* 227 (1991), pp. 245–272.

[41] Joseph Smagorinsky. “General circulation experiments with the primitive equations: I. The basic experiment”. In: *Monthly weather review* 91.3 (1963), pp. 99–164.

[42] James W Deardorff. “A numerical study of three-dimensional turbulent channel flow at large Reynolds numbers”. In: *Journal of Fluid Mechanics* 41.2 (1970), pp. 453–480.

[43] Massimo Germano et al. “A dynamic subgrid-scale eddy viscosity model”. In: *Physics of Fluids A: Fluid Dynamics* 3.7 (1991), pp. 1760–1765.

[44] Douglas K Lilly. “A proposed modification of the Germano subgrid-scale closure method”. In: *Physics of Fluids A: Fluid Dynamics* 4.3 (1992), pp. 633–635.

[45] Franck Nicoud and Frédéric Ducros. “Subgrid-scale stress modelling based on the square of the velocity gradient tensor”. In: *Flow, turbulence and Combustion* 62.3 (1999), pp. 183–200.

[46] Philippe R Spalart. "Comments on the Feasibility of LES for Wings and on the Hybrid RANS/LES Approach". In: *Proceedings of the First AFOSR International Conference on DNS/LES, 1997.* 1997, pp. 137–147.

[47] M Shur et al. "Detached-eddy simulation of an airfoil at high angle of attack". In: *Engineering turbulence modelling and experiments 4.* Elsevier, 1999, pp. 669–678.

[48] Philippe R Spalart et al. "A new version of detached-eddy simulation, resistant to ambiguous grid densities". In: *Theoretical and computational fluid dynamics* 20 (2006), pp. 181–195.

[49] Mikhail L Shur et al. "A hybrid RANS-LES approach with delayed-DES and wall-modelled LES capabilities". In: *International journal of heat and fluid flow* 29.6 (2008), pp. 1638–1649.

[50] Michael James Lighthill. "On sound generated aerodynamically I. General theory". In: *Proceedings of the Royal Society of London. Series A. Mathematical and Physical Sciences* 211.1107 (1952), pp. 564–587.

[51] Michael James Lighthill. "On sound generated aerodynamically II. Turbulence as a source of sound". In: *Proceedings of the Royal Society of London. Series A. Mathematical and Physical Sciences* 222.1148 (1954), pp. 1–32.

[52] Newby Curle. "The influence of solid boundaries upon aerodynamic sound". In: *Proceedings of the Royal Society of London. Series A. Mathematical and Physical Sciences* 231.1187 (1955), pp. 505–514.

[53] JE Ffowcs Williams and David L Hawkings. “Sound generation by turbulence and surfaces in arbitrary motion”. In: *Philosophical Transactions for the Royal Society of London. Series A, Mathematical and Physical Sciences* (1969), pp. 321–342.

[54] H. G. Weller et al. “A tensorial approach to computational continuum mechanics using object-oriented techniques”. In: *Computers in Physics* 12.6 (1998), pp. 620–631.

[55] Franjo Juretić. “cfMesh user guide”. In: *Creative Fields, Zagreb* (2015).

[56] Andre Ribes and Christian Caremoli. “Salomé platform component model for numerical simulation”. In: *31st Annual International Computer Software and Applications Conference, Beijing, China, 24-27 July*. Vol. 2. 2007, pp. 553–564.

[57] July 2023. URL: `https://www.salome-platform.org/?page_id=2430`.

[58] Dudley Brian Spalding. “A novel finite difference formulation for differential expressions involving both first and second derivatives”. In: *International Journal for Numerical Methods in Engineering* 4.4 (1972), pp. 551–559.

[59] Richard M Beam and RoF Warming. “An implicit factored scheme for the compressible Navier-Stokes equations”. In: *AIAA journal* 16.4 (1978), pp. 393–402.

[60] Mohit Arora and Philip L Roe. “A well-behaved TVD limiter for high-resolution calculations of unsteady flow”. In: *Journal of Computational Physics* 132.1 (1997), pp. 3–11.

[61] Bram Van Leer. “Towards the ultimate conservative difference scheme. II. Monotonicity and conservation combined in a second-order scheme”. In: *Journal of computational physics* 14.4 (1974), pp. 361–370.

[62] A Harten. “High resolution schemes for hyperbolic conservation laws”. In: *Journal of Computational Physics* 49.3 (1983), pp. 357–393.

[63] Peter Lax and Burton Wendroff. *Systems of conservation laws.* Tech. rep. Los Alamos National Lab.(LANL), Los Alamos, NM (United States), 1958.

[64] John Crank and Phyllis Nicolson. “A practical method for numerical evaluation of solutions of partial differential equations of the heat-conduction type”. In: *Mathematical proceedings of the Cambridge philosophical society.* Vol. 43. 1. Cambridge University Press. 1947, pp. 50–67.

[65] LS Caretto et al. “Two calculation procedures for steady, three-dimensional flows with recirculation”. In: *Proceedings of the Third International Conference on Numerical Methods in Fluid Mechanics, Paris, France, 3-7 July.* Springer. 1973, pp. 60–68.

[66] Raad I Issa. “Solution of the implicitly discretised fluid flow equations by operator-splitting”. In: *Journal of computational physics* 62.1 (1986), pp. 40–65.

[67] Andrey Epikhin et al. “Development of a dynamic library for computational aeroacoustics applications using the OpenFOAM open source package”. In: *Procedia Computer Science* 66 (2015), pp. 150–157.

[68] Kenneth S Brentner and Feri Farassat. "Analytical comparison of the acoustic analogy and Kirchhoff formulation for moving surfaces". In: *AIAA journal* 36.8 (1998), pp. 1379–1386.

[69] Guillaume Brès, Franck Pérot, and David Freed. "A Ffowcs Williams-Hawkings solver for Lattice-Boltzmann based computational aeroacoustics". In: *16th AIAA/CEAS aeroacoustics conference*. 2010, p. 3711.

[70] Andrey Epikhin. "Validation of the developed open source library for far-field noise prediction". In: *Proceedings of the 27th International Congress on Sound and Vibration, Denver, Colorado*. 2021.

[71] Michael T Heideman, Don H Johnson, and C Sidney Burrus. "Gauss and the history of the fast Fourier transform". In: *Archive for history of exact sciences* (1985), pp. 265–277.

[72] S Mendez et al. "On the use of the Ffowcs Williams-Hawkings equation to predict far-field jet noise from large-eddy simulations". In: *International Journal of Aeroacoustics* 12.1-2 (2013), pp. 1–20.

[73] Christoph Richter. *Liner impedance modeling in the time domain with flow*. Univerlagtuberlin, 2009.

[74] PD Dean. "An in situ method of wall acoustic impedance measurement in flow ducts". In: *Journal of Sound and Vibration* 34.1 (1974), 97–IN6.

[75] British Standard et al. "Acoustics-determination of sound absorption coefficient and impedance in impedance tubes—part 2: Transfer-function method". In: *BS EN ISO* (2001), pp. 10534–2.

[76] LJ Sivian. “Acoustic impedance of small orifices”. In: *The Journal of the Acoustical Society of America* 7.2 (1935), pp. 94–101.

[77] Uno Ingard. “On the theory and design of acoustic resonators”. In: *The Journal of the acoustical society of America* 25.6 (1953), pp. 1037–1061.

[78] GD Garrison et al. “Suppression of combustion oscillations with mechanical damping devices”. In: *Interim Report PWA FR-3299, Pratt & Whitney Aircraft* (1969).

[79] Edward J. Rice. “Model for the Acoustic Impedance of a Perforated Plate Liner with Multiple Frequency Excitation”. In: *The Journal of the Acoustical Society of America* 51.1A (1972), pp. 94–95. DOI: `10.1121/1.1981715`.

[80] Andrew B Bauer. “Impedance theory and measurements on porous acoustic liners”. In: *Journal of Aircraft* 14.8 (1977), pp. 720–728.

[81] J Kooi and S Sarin. “An experimental study of the acoustic impedance of Helmholtz resonator arrays under a turbulent boundary layer”. In: *7th Aeroacoustics Conference, Palo Alto, CA, USA, 5-7 October*. 1981, p. 1998.

[82] A Goldman and CH Chung. “Impedance of an orifice under a turbulent boundary layer with pressure gradient”. In: *The Journal of the Acoustical Society of America* 71.3 (1982), pp. 573–579.

[83] R Kirby and A Cummings. “The impedance of perforated plates subjected to grazing gas flow and backed by porous media”. In: *Journal of sound and vibration* 217.4 (1998), pp. 619–636.

[84] T Zandbergen. “On the practical use of a three-microphone technique for in-situ acoustic impedance measurements on double layer flow duct liners”. In: *7th Aeroacoustics Conference, Palo Alto, CA, USA, 5-7 October*. 1981, p. 2000.

[85] ER Rademaker and EAFA Demmenie. “In-situ acoustic impedance measurements on air-injected liners under grazing flow”. In: *33rd International Congress and Exposition on Noise Control Engineering, Prague, Czech Republic.* 2004, p. 146.

[86] Antoni Alomar and Yves Auregan. “Liner impedance determination from PIV acoustic measurements”. In: *10th Euronoise Conference, Maastricht, The Netherlands, 31 May - 3 June*. 2015, pp. 2231–2236.

[87] J Celano, A Hersh, and B Walker. “Semi-empirical Helmholtz resonator impedance model”. In: *5th AIAA/CEAS Aeroacoustics Conference and Exhibit, Bellevue, WA, USA, 10-12 May*. 1999, p. 1825.

[88] Alan Hersh, Bruce Walker, and Joseph Celano. “Effect of grazing flow and spl on impedance of 2-dof resonators”. In: *8th AIAA/CEAS Aeroacoustics Conference And Exhibit, Breckenridge, CO, USA, 17-19 June*. 2002, p. 2443.

[89] S Mekid and M Farooqui. “Design oF Helmholtz resonators in one and two degrees of freedom for noise attenuation in pipelines.” In: *Acoustics Australia* 40.3 (2012).

[90] Leandro Rego et al. “Acoustic liners for jet-installation noise reduction”. In: *Journal of Sound and Vibration* 537 (2022), p. 117189. ISSN: 0022-460X. DOI: `https://doi.org/10.1016/j.jsv.2022.117189`.

[91] Julian Winkler et al. "High fidelity modeling tools for engine liner design and screening of advanced concepts". In: *International Journal of Aeroacoustics* (2021), pp. 1–31.

[92] Christopher K.W. Tam et al. "Experimental validation of numerical simulations for an acoustic liner in grazing flow: Self-noise and added drag". In: *Journal of Sound and Vibration* 333.13 (2014), pp. 2831–2854. ISSN: 0022-460X. DOI: `https://doi.org/10.1016/j.jsv.2014.02.019`.

[93] Rémi Roncen et al. "Spatially-varying impedance model for locally reacting acoustic liners at a high sound intensity". In: *Journal of Sound and Vibration* 524 (2022), p. 116741. ISSN: 0022-460X. DOI: `https://doi.org/10.1016/j.jsv.2021.116741`.

[94] Adrien Mann et al. "Characterization of Acoustic Liners Absorption using a Lattice-Boltzmann Method". In: *19th AIAA/CEAS Aeroacoustics Conference And Exhibit, Berlin, Germany, 27–29 May.* 2013, pp. 4032–4052. DOI: `10.2514/6.2013-2271`.

[95] Chenzhen Ji and Dan Zhao. "Lattice Boltzmann investigation of acoustic damping mechanism and performance of an in-duct circular orifice". In: *The Journal of the Acoustical Society of America* 135.6 (2014), pp. 3243–3251. DOI: `10.1121/1.4876376`.

[96] D. Casalino, A. Hazir, and A. Mann. "Turbofan Broadband Noise Prediction Using the Lattice Boltzmann Method". In: *AIAA Journal* 56.2 (2018), pp. 609–628. DOI: `10.2514/1.J055674`.

[97] Jean Dassé, Simon Mendez, and Franck Nicoud. “Large-Eddy Simulation of the Acoustic Response of a Perforated Plate”. In: *14th AIAA/CEAS Aeroacoustics Conference and Exhibit, Vancouver, BC, Canada, 5–7 May.* 2008, pp. 2983–2991. DOI: `10.2514/6.2008-3007`.

[98] Qi Zhang and Daniel J Bodony. “Numerical investigation and modelling of acoustically excited flow through a circular orifice backed by a hexagonal cavity”. In: *Journal of Fluid Mechanics* 693 (2012), pp. 367–401.

[99] Qi Zhang and Daniel J. Bodony. “Numerical investigation of a honeycomb liner grazed by laminar and turbulent boundary layers”. In: *Journal of Fluid Mechanics* 792 (2016), pp. 936–980. DOI: `10.1017/jfm.2016.79`.

[100] Michaël Bauerheim and Laurent Joly. “LES of the aero-acoustic coupling in acoustic liners containing multiple cavities”. In: *AIAA Aviation 2020 Forum.* 2020, p. 2571.

[101] Soizic Esnault et al. “Large Eddy Simulation of Heat Transfer Within a Multi-Perforation Synthetic Jets Configuration”. In: *Journal of Turbomachinery* 142.6 (2020).

[102] Michael Jones et al. “Design and evaluation of modifications to the NASA Langley flow impedance tube”. In: *10th AIAA/CEAS Aeroacoustics Conference and Exhibit, Manchester, UK, 10-12 May.* 2004, p. 2837.

[103] Simone Giaccherini et al. “Validation of an Analytical Model for the Acoustic Impedance Eduction of Multi-Cavity Resonant Liners by a High-Fidelity LES Approach”. In: *Journal of Turbomachinery* (2023), pp. 1–33.

[104] Lorenzo Pinelli et al. “Validation of a 3D Linearized Method for Turbomachinery Tone Noise Analysis”. In: *ASME Turbo*

Expo, Vancouver, British Columbia, 6-10 June. 2011, pp. 1033–1042. DOI: `10.1115/GT2011-45886`.

[105] L. Pinelli et al. "A linearized method for tone noise generation and propagation analysis in a multistage contra-rotating turbine". In: 9^{th} *European Conference on Turbomachinery Fluid Dynamics and Thermodynamics, Istanbul, Turkey, 21-25 March.* 2011, pp. 1253–1263.

[106] Paolo Gaetani et al. "Computational and Experimental Study of Hot Streak Transport Within the First Stage of a Gas Turbine". In: *Journal of Turbomachinery* 142.8 (July 2020). 081002. ISSN: 0889-504X. DOI: `10.1115/1.4045961`.

[107] Lorenzo Pinelli et al. "Computational and Experimental Study of the Unsteady Convection of Entropy Waves Within a High-Pressure Turbine Stage". In: *Journal of Turbomachinery* 143.9 (May 2021). 091011. ISSN: 0889-504X. DOI: `10.1115/1.4050600`.

[108] Lorenzo Pinelli et al. "The Effects of Swirling Flows in Entropy Wave Convection Through High-Pressure Turbine Stage". In: *Journal of Turbomachinery* 145.3 (Oct. 2022). 031004. ISSN: 0889-504X. DOI: `10.1115/1.4055613`.

[109] Lorenzo Pinelli et al. "Effect of clocking on entropy noise generation within an aeronautical high pressure turbine stage". In: *Journal of Sound and Vibration* 529 (2022), p. 116900. ISSN: 0022-460X. DOI: `https://doi.org/10.1016/j.jsv.2022.116900`.

[110] Lorenzo Pinelli et al. "Forced response in a multi-stage aeroderivative axial compressor with acoustic excitations: Method validation with field data". In: *Aerospace Science*

and Technology 138 (2023), p. 108305. ISSN: 1270-9638. DOI: `https://doi.org/10.1016/j.ast.2023.108305`.

[111] Willie R. Watson, Sharon E. Tanner, and Tony L. Parrott. “Optimization Method for Educing Variable-Impedance Liner Properties”. In: *AIAA Journal* 36.1 (1998), pp. 18–23. DOI: `10.2514/2.369`.

[112] T J&amp Poinsot and SK Lelef. “Boundary conditions for direct simulations of compressible viscous flows”. In: *Journal of computational physics* 101.1 (1992), pp. 104–129.

[113] Jeffrey P Van Doormaal and George D Raithby. “Enhancements of the SIMPLE method for predicting incompressible fluid flows”. In: *Numerical heat transfer* 7.2 (1984), pp. 147–163.

[114] Richard Courant, Kurt Friedrichs, and Hans Lewy. “Über die partiellen Differenzengleichungen der mathematischen Physik”. In: *Mathematische annalen* 100.1 (1928), pp. 32–74.

[115] HK Tanna, PD Dean, and MJ Fisher. “The influence of temperature on shock-free supersonic jet noise”. In: *Journal of Sound and Vibration* 39.4 (1975), pp. 429–460.

[116] HK Tanna, PD Dean, and RH Burrin. *The generation and radiation of supersonic jet noise, part III, Turbulent mixing noise data.* Tech. rep. AFAPL–TR–76–65, 1976.

[117] Erina Murakami and Dimitri Papamoschou. “Mean flow development in dual-stream compressible jets”. In: *AIAA journal* 40.6 (2002), pp. 1131–1138.

[118] CM Or, Kit Ming Lam, and P Liu. “Potential core lengths of round jets in stagnant and moving environments”. In: *Journal of Hydro-environment Research* 5.2 (2011), pp. 81–91.

[119] Nicholas Georgiadis and Dimitri Papamoschou. “Computational investigations of high-speed dual stream jets”. In: *9th AIAA/CEAS Aeroacoustics Conference and Exhibit.* 2003, p. 3311.

[120] G Saravanan, A Vinoth Kumar, and KB Ravichandrakumar. “Numerical analysis of subsonic coaxial jet on effect of potential core length”. In: *Journal of Advances in Mechanical Engineering and Science* 2.1 (2016), pp. 26–32.

[121] Henry E Bass et al. “Atmospheric absorption of sound: Further developments”. In: *The Journal of the Acoustical Society of America* 97.1 (1995), pp. 680–683.

[122] James Bridges and Clifford Brown. “Parametric testing of chevrons on single flow hot jets”. In: *10th AIAA/CEAS aeroacoustics conference.* 2004, p. 2824.

[123] J Seiner and G Reethof. “On the distribution of source coherency in subsonic jets”. In: *12th Aerospace Sciences Meeting.* 1974, p. 4.

[124] M Schaffar. “Direct measurements of the correlation between axial in-jet velocity fluctuations and far field noise near the axis of a cold jet”. In: *Journal of sound and vibration* 64.1 (1979), pp. 73–83.

[125] WG Richarz. “Direct correlation of noise and flow of a jet using laser Doppler”. In: *AIAA journal* 18.7 (1980), pp. 759–765.

[126] Ralph R Armstrong, Alfons Michalke, and Helmut V Fuchs. “Coherent structures in jet turbulence and noise”. In: *AIAA Journal* 15.7 (1977), pp. 1011–1017.

[127] Jayanta Panda, Richard Seasholtz, and Kristie Elam. “Measurement of Correlation Between Flow Density, Velocity and Density* velocity2 with Far Field Noise in High Speed Jets”. In: *8th AIAA/CEAS Aeroacoustics Conference & Exhibit*. 2002, p. 2485.

[128] Christophe Bogey and Christophe Bailly. “Investigation of sound sources in subsonic jets using causality methods on LES data”. In: *11th AIAA/CEAS aeroacoustics conference*. 2005, p. 2885.

[129] Christopher KW Tam et al. “The sources of jet noise: experimental evidence”. In: *Journal of Fluid Mechanics* 615 (2008), pp. 253–292.

[130] Bryan Callender, Ephraim Gutmark, and Steve Martens. “Far-field acoustic investigation into chevron nozzle mechanisms and trends”. In: *AIAA journal* 43.1 (2005), pp. 87–95.

[131] Mehmet B Alkislar, Anjaneyulu Krothapalli, and GW Butler. “The effect of streamwise vortices on the aeroacoustics of a Mach 0.9 jet”. In: *Journal of Fluid Mechanics* 578 (2007), pp. 139–169.

[132] David Munday et al. “Acoustic Effect of Chevrons on Jets Exiting Conical CD Nozzles”. In: *15th AIAA/CEAS Aeroacoustics Conference (30th AIAA Aeroacoustics Conference)*. 2008, p. 3128.

[133] Robert Schlinker et al. “Supersonic jet noise from round and chevron nozzles: experimental studies”. In: *15th AIAA/CEAS*

Aeroacoustics Conference (30th AIAA Aeroacoustics Conference). 2009, p. 3257.

[134] Stanley Birch et al. “Noise predictions for chevron nozzle flows”. In: *12th AIAA/CEAS Aeroacoustics Conference (27th AIAA Aeroacoustics Conference)*. 2006, p. 2600.

[135] PS Tide and V Babu. “Numerical predictions of noise due to subsonic jets from nozzles with and without chevrons”. In: *Applied Acoustics* 70.2 (2009), pp. 321–332.

[136] Michael L Shur et al. “Analysis of jet-noise-reduction concepts by large-eddy simulation”. In: *International journal of aeroacoustics* 6.3 (2007), pp. 243–285.

[137] Ali Uzun and M Yousuff Hussaini. “Simulation of noise generation in the near-nozzle region of a chevron nozzle jet”. In: *AIAA journal* 47.8 (2009), pp. 1793–1810.

[138] Ali Uzun, Jonghoon Bin, and M Yousuff Hussaini. “High-fidelity numerical simulation of a chevron nozzle jet flow”. In: *International Journal of Aeroacoustics* 10.5-6 (2011), pp. 531–564.

[139] Ali Uzun and M Youssuff Hussaini. “Some issues in large-eddy simulations for chevron nozzle jet flows”. In: *Journal of Propulsion and Power* 28.2 (2012), pp. 246–258.

[140] Hao Xia, Paul G Tucker, and Simon Eastwood. “Large-eddy simulations of chevron jet flows with noise predictions”. In: *International Journal of Heat and Fluid Flow* 30.6 (2009), pp. 1067–1079.

[141] Gerrit-Daniel Stich et al. “Jet Noise Prediction for Chevron Nozzle Flows with Wall-Modeled Large-Eddy Simulation”. In: *AIAA SciTech Forum*. 2021.

[142] Gerrit-Daniel Stich et al. “Large-Eddy Simulation of Jet Surface Interaction Noise”. In: *25th AIAA/CEAS aeroacoustics conference*. 2019, p. 2475.

[143] Alexander Kurganov and Eitan Tadmor. “New high-resolution central schemes for nonlinear conservation laws and convection–diffusion equations”. In: *Journal of computational physics* 160.1 (2000), pp. 241–282.

[144] Markus Klein, Amsini Sadiki, and Johannes Janicka. “A digital filter based generation of inflow data for spatially developing direct numerical or large eddy simulations”. In: *Journal of computational Physics* 186.2 (2003), pp. 652–665.

[145] Zheng-Tong Xie and Ian P Castro. “Efficient generation of inflow conditions for large eddy simulation of street-scale flows”. In: *Flow, turbulence and combustion* 81 (2008), pp. 449–470.

[146] R Poletto, T Craft, and A Revell. “A new divergence free synthetic eddy method for the reproduction of inlet flow conditions for LES”. In: *Flow, turbulence and combustion* 91 (2013), pp. 519–539.